THE CHEMICAL STRUCTURE OF METAL/SEMICONDUCTOR INTERFACES AS DETERMINED BY X-RAY PHOTOELECTRON SPECTROSCOPY

Thesis by

Paula Jean Grunthaner

In Partial Fulfillment of the Requirements

for the Degree of

Doctor of Philoscopy

California Institute of Technology

Pasadena, California

1980

(Submitted May 22, 1980)

ACKNOWLEDGMENTS

As this period of my life draws to a close, it is appropriate to thank the many people who have contributed to the successful completion of my graduate studies at Caltech. I have had the pleasure of working closely with many people at both Caltech and the Jet Propulsion Laboratory.

A simple thanks is not sufficient to acknowledge the contributions of my advisor Jim Mayer. He has influenced my career more than any other single person. I have come to appreciate not only the style of his science but also the unique philosophy with which he approaches it. A heartfelt thanks to you, Jim.

Most thesis acknowledgments always seem to leave room at the end to thank one's parents and spouse for support during the graduate career. I would like to state upfront that the love and support of my parents and my husband Frank have been instrumental in the successful completion of four years at Caltech. They were always there when I needed them. Frank has also contributed immensely to the technical aspects of this work.

Many additional people have contributed technically to the work reported in this thesis. I would like to thank Dave Scott for his collaboration in the impurity studies reported in Chapter V. Nathan Cheung and Bor Yeu Tsaur have provided advice and insight concerning silicide reactions. The technical assistance of Rouel Fernandez for

the metal depositions and Dan Tonn for the ion implantation is greatefully acknowledged. The friendship and assistance of Michelle Parks has been most helpful.

I would like to thank Len Feldman from Bell Laboratories for useful discussions. His insight helped to quide the studies presented in this thesis.

Anupam Madhukar has also been very generous with his time. Many long hours have been spent discussing experiments and data interpretation. Special thanks are due.

At the Jet Propulsion Laboratory, there are many people to acknowledge. I thank Blair Lewis, Jim Wurzbach, Rick Vasquez, and Joe Maserjian for many helpful and stimulating discussions. The technical assistance of Frank Lombardi and Chuck Zachman is also greatly appreciated. Thanks goes to Malcolm Rayfield for his patience with my ignorance of computers. I thank Don Lawson for his help with sample preparations. Marge Brandenberg and Terry Pipes are to be thanked for running interference with all the paperwork that JPL is capable of generating.

The assistance of the Jet Propulsion Laboratory through its tuition support program is gratefully acknowledged.

ABSTRACT

The chemical nature of transition metal/silicon interfaces has been investigated using x-ray photoelectron (XPS) and Rutherford backscattering (RBS) spectroscopy. In particular, the Ni/Ni_2Si, Si/Ni_2Si, and Ni/Si transitional regions have been examined in detail. The effect of oxygen impurities on the Ni/NiSi interface has been studied using ion implantation and $^{16}O(d,\alpha)^{14}N$ nuclear reactions in conjunction with XPS and RBS. Preliminary results on the Pd/Pd_2Si and Pt/Pt_2Si interfaces are presented and contrasted to the Ni system.

A technique for studying silicide/silicon and silicide/metal interfaces has been developed in the course of this work. The approach exploits the exponential attenuation of photoemission intensities to dynamically monitor the advancing planar silicide growth front during the *in situ* growth of the silicide. The technique allows the examination of a realistic interface bounded on either side by an extended solid without the chemical and structural perturbations caused by conventional depth profiling methods. The local chemical environment of both the silicon and transition metal atoms has been established through analysis of the observed binding energy shifts in the photoemission spectra. $^4He^+$ backscattering has been used to follow the progression of the thin film reaction and to provide quantitative information on atomic composition.

These interfacial experiments demonstrated that the local environment of the Ni atoms at the Si/Ni_2Si interface is more Si-rich than that found for Ni in Ni_2Si. The transition layer is not a unique silicide phase, but rather is graded in composition. The first detectable Ni $2p_{3/2}$ signal is consistent with a single Ni atom located in the octahedral/tetrahedral interstitial voids in a pure Si lattice. The width of the amorphous Si/Ni_2Si interface was determined to be at least 1.5λ, where λ is the escape depth for Ni 2p electrons in the interfacial layer. A lower limit of 22 Å may be placed on the width of the transition region assuming a value of 15 Å for λ.

The Ni/Ni_2Si interface was examined using both amorphous and crystalline Si as a substrate. In each case, it was demonstrated that the Si atoms in the transition region are in a substantially more Ni-rich environment than that found for Si in Ni_2Si. These regions are again of graded composition. The first Si 2p signal observed is consistent with a metallic-like Si substituted in the fcc lattice of Ni metal. The essential difference between the Ni/Ni_2Si interface using a crystalline substrate as compared to an amorphous substrate is that the former is 2 - 3 times narrower (0.6λ) than the latter (1.5λ).

The as-deposited Ni/Si interface was investigated by monitoring the evolution of the Ni and Si core levels as multiple monolayers of Ni were deposited on Si <100>. The data indicate the presence of a chemically graded transition region which ranges in stoichiometry from Ni atoms bound in the Si interstitial voids on the <100> Si side of the interface to Si atoms substituted in the Ni metal lattice on the Ni^{o}

side of the interface.

The chemical nature of the Ni/Si interface as a function of the substrate temperature was also examined. It was shown that substantial chemical interaction occurs between the Ni and Si substrate at temperatures as low as 100^{o} K. Ni metal was deposited on an inert substrate to demonstrate that aggregation effects were not responsible for the observed chemical shifts.

The dependence of the Ni 2p binding energy on the substrate temperature also demonstrated that the initial Ni atom deposited on the Si surface must drop into the interstitial Si voids rather than being bound on the surface. The behavior of the Ni 2p binding energy as a function of Ni coverage at elevated substrate temperatures suggests the presence of several distinct Ni environments.

The effect of oxygen impurities on the Ni/Ni_2Si interface was investigated via ion implantation using XPS, RBS, and $^{16}O(d,\alpha)^{14}N$ nuclear reactions. It was shown that 2.2×10^{16} O/cm^2 are sufficient to block the diffusion of the Ni metal and thereby inhibit the silicide reaction. The data demonstrate that as the advancing Ni/Ni_2Si interface encounters oxygen in the Ni film, silicon suboxides are formed. As more oxygen is encountered, SiO_2 is formed. When a sufficient layer of SiO_2 has formed, the Ni metal is no longer able to diffuse through to the Si/Ni_2Si interface to continue the solid phase reaction.

Preliminary results for the Pd/Pd_2Si and Pt/Pt_2Si interfaces are presented and contrasted to those found for the Ni/Ni_2Si system. The

data suggest that, as the Ni case, the limiting environment for Si at the Pd/Pd_2Si interface is metallic-like with a high ligancy. We propose this is a Si atom substituted in the fcc lattice of Pd metal. The Si atoms at the Pt/Pt_2Si interface, on the other hand, rest in a site of substantially lower coordination number in the fcc Pt lattice. This is suggestive of an interstitial defect site.

Both the Pd/Pd_2Si and Pt/Pt_2Si interfaces are found to be graded in composition. Estimations of these widths indicate that the metal/silicon interface widths decrease in the order Ni > Pt > Pd.

TABLE OF CONTENTS

Table of Contents, Continued

CHAPTER I

INTRODUCTION

Thin film and solid-solid interactions have become critically important in the development of modern technology. In particular, the solid phase reactions of thin metal films with silicon have attracted a great deal of attention, both experimentally and theoretically, in recent years. The great interest in metal silicide formation is a consequence of their increasing use in integrated circuit technology, where they play a primary role in Schottky barrier and contact formation, epitaxial growth, and device reliability. Prior to 1974, over 900 papers were published on the subject of metal-semiconductor interactions[1] and since that time the literature has expanded substantially.

As a result of their technological importance, the transition metal silicides have been thoroughly examined in terms of their formation kinetics and solid state reaction products. In particular, backscattering studies have provided a panoply of such information. The fundamental nature of the chemical bonds formed within the silicides and their interfaces to both silicon and the transition metal have not been adequately investigated. As integrated circuit technology demands tighter constraints on thin film dimensions, the importance of understanding the interdiffusion and reactions at interfacial regions can only increase.

Aside from the technological incentives, the study of solid phase metal-silicon interactions is of scientific interest because of the opportunity to characterize unique chemical bonding environments. The

interface between two solids provides a region structurally and thermodynamically different from that which can be found in the bulk. The investigation of this region presents an experimental challenge, but it promises a substantial return in the understanding of the relationship between chemical bonding and electronic characteristics.

Several interesting questions also arise concerning the mechanism responsible for the solid phase silicide reaction. For instance, thin films of the near-noble metals Ni, Pd, and Pt on silicon are known to form silicides at temperatures as low as 100°C.[2-3] This is only 0.3-0.4 of the eutectic temperature of the binary systems.[4] At these low temperatures, phonon energies are not sufficient to dissociate the covalent bonds in silicon. An alternate low temperature mechanism must be responsible for the formation of the near-noble metal silicides. An understanding of the chemical nature of the interfacial regions may help to elucidate these mechanisms.

Thus the impetus for the work reported in this thesis is derived from two basic themes: (1) the relevance of the transition metal silicides to technology and (2) scientific incentives due to the unique chemical environments at the metal/silicide and silicon/silicide interfaces.

References

1) A. H. Agajanian, V. L. Rideout, "A Bibliography on Metal-semiconductor (Schottky Barrier) Contacts," IBM Tech. Report TR22-1745, March 4, 1974

2) K. N. Tu, Appl. Phys. Lett., 27, 221 (1975)

3) J. W. Mayer, K. N. Tu, J. Vac. Sci. Technol., 11, 86 (1974)

4) M. Hansen, K. Anderko, Constitution of Binary Alloys, 2nd edn. (McGraw-Hill, New York, N.Y., 1958)

CHAPTER II

EXPERIMENTAL METHODS

A. INTRODUCTION

The work reported in this thesis has employed two complementary techniques to probe the structure of the transition metal silicides and their interfaces. These techniques are Rutherford backscattering spectroscopy (RBS) and x-ray photoelectron spectroscopy (XPS). In XPS, one measures the electron charge density on an atom core, which in turn reflects the chemical environment of that atom. A limitation of this surface technique is its inability to provide straightforward quantitative information. Using RBS, one may quantitatively determine the atomic composition of a solid as a function of depth. The success of the interfacial investigations reported in the following chapters was highly dependent upon having both chemical and compositional information. The combination of these two spectroscopies thus allowed the characterization of the bulk and interfacial systems studied here.

In this chapter, the basic concepts of XPS and RBS are presented. Only the theoretical considerations necessary to understand the work presented in this thesis will be discussed. Excellent detailed treatments of RBS[1] and XPS[2-4] may be found elsewhere.

B. X-RAY PHOTOELECTRON SPECTROSCOPY

1. General Theoretical Considerations

In solid state XPS, one analyzes the kinetic energy of electrons ejected when a solid is irradiated with monoenergetic photons of energy $h\nu$. The relevant energy conservation equation is

$$h\nu + E^{i}_{tot} = E_{kin} + E^{f}_{tot}(k) \qquad \text{II-1}$$

where E^{i}_{tot} is the total energy of the initial state, E_{kin} is the kinetic energy of the photoelectron, and $E^{f}_{tot}(k)$ is the total final energy of the system after ejection of the photoelectron from the k^{th} level. Contributions from a recoil energy E_r can be neglected. Siegbahn et al.[5] calculated the recoil energies for valence shell photoelectrons with AlKα radiation for different atoms: H = 0.9 eV, Li = 0.1 eV, Na = 0.04 eV, K = 0.02 eV, Rb = 0.01 eV. Only for the lightest atoms (H, He, Li) is E_r significant when compared to the instrumental linewidths in XPS spectra. The binding energy of the photoelectron is defined as the energy required to remove it to infinity with a zero kinetic energy. If $E^{V}_{b}(k)$ is the binding energy of an electron in the k^{th} level referred to the vacuum level, then

$$E^{V}_{b}(k) = E^{f}_{tot} - E^{i}_{tot} \qquad \text{II-2}$$

Substituting II-2 into II-1 results in the familiar photoelectric equation

$$h\nu = E_{kin} + E^{V}_{b}(k) \qquad \text{II-3}$$

In the case of a solid specimen, an electrical contact is made to the spectrometer. For metallic samples, such as the metal silicides, the resulting energy levels are shown in Figure 1. Because the sample and spectrometer are in thermodynamic equilibrium, their electron chemical potentials or Fermi levels are equal. In passing from the sample surface into the spectrometer, the photoelectron will feel a potential equal to the difference between the spectrometer work function ϕ_{spec} and the sample work function ϕ_s. Thus, the electron kinetic energy E'_{kin} at the sample surface is measured as E_{kin} inside the spectrometer analyzer.

$$E_{kin} = E'_{kin} + (\phi_s - \phi_{spec}) \qquad \text{II-4}$$

From Figure 1 it can be seen that the binding energy in a metallic specimen may be determined relative to the common Fermi level as follows

$$h\nu = E_b^F(k) + E_{kin} + \phi_{spec}. \qquad \text{II-5}$$

Notice that the sample work function, ϕ_s, is not involved. The sample work function can be derived from photoelectron spectra, however, by measuring the zero-kinetic energy cutoff of the secondary electron peak and the high-kinetic energy cutoff due to excitation from the occupied states at the Fermi level. If the difference between these cutoffs is ΔE then

$$\phi_s = h\nu - \Delta E \qquad \text{II-6}$$

This procedure for determining ϕ_s is used frequently in UPS[12,15] but has only been used for a few cases in XPS[13-14].

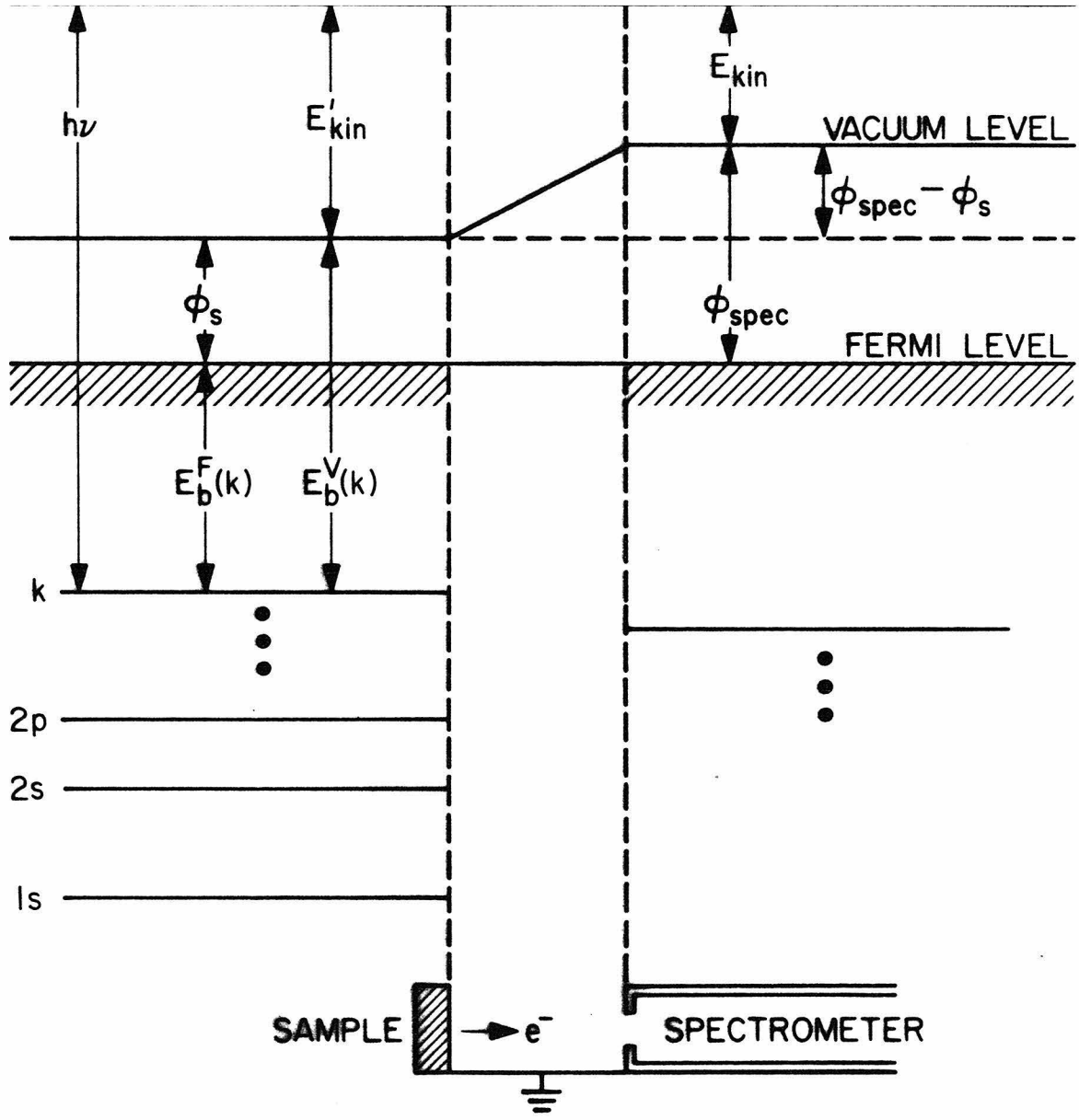

Figure 1: **Energy level diagram from a metallic specimen electrically connected to an electron spectrometer.**

2. Core Electron Binding Energy Shifts

The exact binding energy for an electron in a given element depends on the chemical environment of that element. If we consider a core level, the energy of an electron in this core state is determined by the repulsive core Coulomb interaction with the other electrons and the attractive potential of the nuclei. Any change in the chemical environment of the element will involve a spatial redistribution of the valence electron charges of this atom and the creation of a different potential from the electrons and nuclei of the other elements around it. This redistribution affects the potential of the core electrons and results in a change in their binding energies.

Many attempts have been made with varying degrees of success to theoretically interpret core level chemical shifts[5-9]. A discussion of these theories is beyond the scope of this chapter. A brief outline of the most significant of the theoretical models may be found in the review by Fadley[3].

The chemical shifts of all the core levels in a given atom should be the same as long as the core electrons overlap relatively little with the valence shell. This may be understood with a simple classical model. One may approximate the valence electron distribution by a spherical charged shell with radius r. If q is the charge in the valence shell, then the potential within the shell will be a constant q/r. A change in the valence charge of Δq will result in a binding energy change of all the core levels inside the shell of $\Delta E_b = \Delta q/r$. The

prediction that the various core levels in a given atom should experience the same chemical shift when the environment of the atom is changed has been verified experimentally.[10-11] Fadley, et al.[11], in an investigation of iodine compounds, found that the shifts in the 2s, $2p_{1/2}$, $2p_{3/2}$, $3d_{3/2}$, $3d_{5/2}$, 4s, and $4p_{3/2}$ levels of iodine were all identical within experimental error.

3. Final State Effects

Complexities in the final state of the photoemission process give rise to several effects on the observed binding energy of the photoelectron. Relaxation shifts, shake-up and shake-off transitions, multiplet splittings, and other many-electron effects are all final state electronic phenomena. Only relaxation shifts are relevant to the data presented in this thesis and will be briefly discussed below. Detailed treatments of relaxation and other final state effects may be found in several recent reviews.[3, 16-19]

Conceptually, the relaxation energy may be divided into two parts: an intra-atomic term and an extra-atomic term. Intra-atomic relaxation is a result of the one-electron orbitals of an atom relaxing toward the hole of positive charge created by the photoemission of an electron. These orbitals relax adiabatically, imparting additional energy to the photoejected electron. The effect is to lower the measured binding energy of this electron. In addition to this atomic relaxation, the sudden creation of a positive charge in a solid tends to polarize the passive electrons in the surrounding medium. This contribution to the

relaxation energy is termed extra-atomic. The effect again is to lower the observed electron binding energy because the photoemitted electron acquires the energy lost by the passive electrons relaxing toward the region of more attractive potential. On the time scale of this electronic relaxation, the atomic nuclei are effectively frozen in place.

4. Photoelectron Peak Intensities

The intensity dI_k of electrons of a given energy originating in a volume element dxdydz in a homogeneous material is given by[3]

$$dI_k = \begin{bmatrix}\text{x-ray flux}\\ \text{at x, y, z}\end{bmatrix} \cdot \begin{bmatrix}\text{Number of atoms}\\ \text{in dxdydz}\end{bmatrix} \cdot \begin{bmatrix}\text{Differential cross}\\ \text{section for k shell}\end{bmatrix}$$

$$\cdot \begin{bmatrix}\text{Acceptance solid angle of}\\ \text{electron analyzer at x, y, z}\end{bmatrix} \cdot \begin{bmatrix}\text{Probability for no-loss}\\ \text{escape from specimen}\end{bmatrix}$$

$$\cdot \begin{bmatrix}\text{Instrumental detection}\\ \text{efficiency}\end{bmatrix} \qquad \text{II-4}$$

One may assume that the x-ray flux is unattenuated over the thickness range from which the photoelectron can emerge. Neglecting elastic scattering, the probability for no-loss escape may be expressed in terms of a characteristic electron attenuation length or mean free path λ. Specifically, the no-loss photoelectron intensity is given by an exponential decay law

$$I = I_o\, e^{-x/\lambda} \qquad \text{II-5}$$

where x is the distance through the solid traveled by the electron. The attenuation length λ is a function of the electron kinetic energy and the solid matrix through which it is traversing. The value of λ is generally determined by measuring the photoemission intensity from uniform overlayers with thicknesses varying on the order of λ. Extensive reviews and compilations of electron mean free path lengths may be found in the literature.[20-23]

The photoelectric cross-sections used in this thesis are those calculated by Scofield.[24]

5. Instrumental Characteristics

Conceptually, the experiments reported in this thesis are straightforward. The success or failure of these experiments, however, is highly dependent upon the characteristics of the XPS instrumentation used. The dynamic interface studies reported in Chapter III, in particular, require signal/noise and energy resolution characteristics that challenge the present instrument technology. A modified Hewlett-Packard 5950A ESCA spectrometer has been used for the work reported here. The instrumental characteristics and modifications responsible for the success of these experiments is discussed in this section.

Figure 2 gives a schematic of the HP 5950A. The major components are the x-ray monochromator, the four-element electron lens, the constant energy electrostatic analyzer, and the multichannel detector. The x-ray monochromatization is accomplished by Bragg reflecting the $AlK\alpha_{1,2}$ region of radiation (1486 eV) produced in the x-ray generator from a

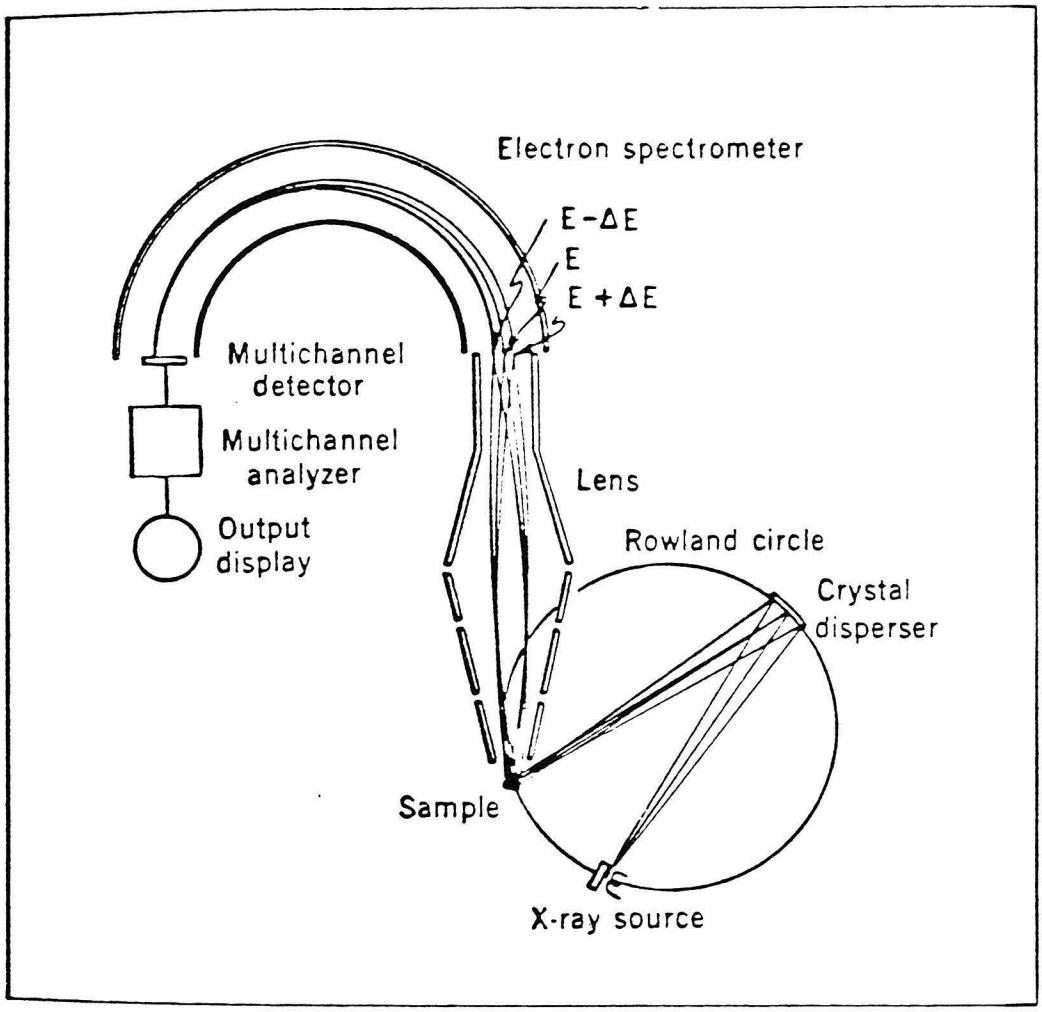

Figure 2: Schematic of the HP 5950A x-ray photoelectron spectrometer.

spherically bent quartz single crystal. This eliminates satellite x-rays and bremsstrahlung radiation. The reflected $AlK\alpha_{1,2}$ doublet is dispersed in wave number across the sample surface. The energy of the x-ray photons incident on the sample varies across the sample with a dispersion of $\sim$ 1 eV. This results in the kinetic energy of the photoelectrons also varying by $\sim$ 1 eV across the sample. Dispersion compensation electron optics are used to remove this inherent line width limitation. The dispersion of the electron spectrometer precisely cancels the dispersion of the x-ray monochromator across the sample. This spectrometer design was originally proposed by Siegbahn et al.[5] in 1967 and allows one to improve the instrument resolution beyond the natural linewidth limitation. The spectrometer response function generally obtained by the HP instrumentation is gaussian with 0.55 eV FWHM.

The HP 5950A spectrometer at the Jet Propulsion Laboratory, which was used in this work, has been extensively reengineered. The modifications to the instrument result in significant increases in signal/noise and energy resolution. In the original system, the electronic subsystems were analog. The spectrometer electronics have been redesigned to be completely digital, which eliminates many systematic contributions to the linewidth and signal to noise ratio. The instrument is controlled by a Varian V76 computer, which continually monitors the various power supplies and potentials in the system.

The most significant modification is in the area of the multichannel detector. In the original HP spectrometer, a multichannel electron multiplier was used to project the electron distribution at the exit

plane of the analyzer onto a phosphor plate. A videcon scanned the phosphor screen to determine the number of electrons falling on a given scan line. Since the scan lines were aligned to the equipotential lines of the analyzer, this corresponded to the number of electrons occurring at a given energy. The videcon system suffers from several severe problems. The primary problems are non-linearities in the analyzer equipotential lines, erratic weighting of each photoelectron, and energy broadening due to the finite spot size on the phosphor screen. It was found that a single electron event was counted by the videcon system 1 to 14 times.[25] This results in non-analytical counting statistics. To avoid these problems, the videcon system has been replaced with a resistive anode position sensitive detector (PSD). This detector consists of a resistively coated plate at the channel-plate output. A charge packet striking this anode is divided among the electrical contacts at the corners of the resistive film. The X-Y spot position is calculated by computer. Only one count is detected per electron event. Thus, $\sqrt{N}$ counting statistics are obtained. In addition, an electronic system has been implemented that allows spectra to be selectively measured from any part of the detector. This feature has been used to empirically determine the non-linearities in the analyzer equipotential lines. This allows distortion correction of the detector. The feature also allows control of the instrument resolution by electronically suppressing low resolution regions of the detector. With the appropriate trade-off in count rate, the instrument response function can be decreased to as low as 0.19 eV FWHM. For the work reported in this thesis, the regions of the detector that suffer from the intensity and energy of spurious internal reflections

off the analyzer walls have been suppressed. This corresponds to a response function of 0.4 eV FWHM. Further details of the detector modifications may be found in reference 25.

The final modification of significance to the work reported here is the incorporation of an aperture in the electron lens train of the spectrometer. This provides a high-throughput mode of operation wherein the count rate of the instrument is increased approximately five-fold. The aperture changes the angular acceptance of the electron optics from the original value of $\sim$ 0.004 Sr to $\sim$ 0.03 Sr. The aperture feature is critically important to the dynamic interface experiments reported in Chapter III. The high-throughput mode allowed the detection of the emerging interface signal far in advance of when it could otherwise be observed. Once the interface was detected in this mode, the lower-throughput mode was reinstated and the spectrum retaken at higher resolution with a correspondingly longer data acquisition time. This procedure allowed the interface to be detected 2-3 electron escape lengths below the sample surface.

The final instrumental characteristic that should be discussed is the residual gas background in the main chamber of the analyzer. This is particularly important for the impurity experiments reported in Chapter V. During normal operation, the residual gas pressure in the unbaked analyzer is typically 5×10^{-10} Torr. The residual gas consists primarily of N_2, CO and H_2 with small quantities of hydrocarbons and rare gases.

C. BACKSCATTERING SPECTROSCOPY

RBS provides quantitative information on the depth distribution of atomic species through a kinematic consideration of the scattering of incident monoenergetic ions off atoms within a solid. The utility of RBS derives from three basic physical concepts: (1) the energy transfer in an elastic two-body collision, (2) the probability that such a two-body collision will occur, and (3) the energy loss of an ion traversing a dense solid. Each of these processes will be discussed below, but only to the extent necessary to understand the backscattered spectra presented in this thesis. Further details may be found in reference 1.

1. The Kinematic Factor

Consider a particle of mass m and energy E_0 colliding with a stationary particle of mass M ($m < M$). In a single elastic collision, the mass m particle will be deflected by some angle θ from its original direction of motion with energy E_1, where $E_1 < E_0$. The ratio of the projectile energy before and after collision is defined as the kinematic factor K,

$$K \equiv E_1/E_0. \qquad \text{II-6}$$

Through an analysis of the conservation of energy and momentum equations, one may calculate K,

$$K = \frac{(M^2-m^2\sin^2\theta)^{\frac{1}{2}} + m\cos\theta}{M+m}^2 \qquad \text{II-7}$$

Notice that K does not depend on the projectile energy E_0 before collision. Equations II-6 and II-7 are essentially the basis for mass discrimination in backscattering. Knowing the mass m and primary energy E_0 of the projectile and experimentally measuring the energy E_1 at a known angle θ after collision, one can determine the mass M of the target atom.

2. The Scattering Cross Section

The probability that an elastic collision will occur is expressed in terms of a differential scattering cross section $d\sigma/d\Omega$. If Q is the total number of particles incident on the target and dQ is the number of particles detected by the detector at angle θ in the differential solid angle $d\Omega$, then

$$d\sigma/d\Omega \equiv (1/Nt)[dQ/d\Omega/Q], \qquad \text{II-8}$$

where N is the density of the target atoms and t is the thickness of the target. The differential scattering cross section has the units of an area per steradian, which may be interpreted as the probability that a given scattering event will result in a signal at the detector. An average differential cross section may be defined for the number of scattering events falling within a finite solid angle Ω.

$$\sigma \equiv (1/\Omega)\int_{\Omega} (d\sigma/d\Omega)d\Omega. \qquad \text{II-9}$$

The scattering cross section σ of the elements is known quite accurately and a compilation may be found in reference 1. The total number of detected backscattered particles A can then be simply expressed as

$$A = \sigma\Omega \cdot Q \cdot Nt, \qquad \text{II-10}$$

where Q is the total number of incident particles and Nt is the number of atoms per unit area in the target. Herein lies the ability of RBS to quantitatively determine the number of atoms per unit area of the sample. Knowing σ and Ω and experimentally measuring A and Q, Nt can be easily determined.

3. Stopping Cross Section

The capacity for depth perception with RBS is due to the fact that in addition to the energy loss suffered from elastic collisions with atoms in a solid, ions traversing a solid lose energy through electronic interactions. An energetic particle impinging on a target penetrates into it. As it traverses the solid, it loses kinetic energy, the exact amount of which depends on the target composition and the nature of the projectile. The energy loss per unit length is generally abbreviated the dE/dx loss.

The energy loss per unit length, dE/dx, depends upon the number of electrons that each atom contributes to the medium through which the particle passes.[26] It is thus convenient to introduce a quantity to express the effectiveness of each atom in stopping the particle. This is defined as the stopping cross section ε.

$$\varepsilon \equiv (1/N)\ (dE/dx). \qquad \text{II-11}$$

Because the stopping cross section is independent of the atomic density of the elements, ε for a compound target may be simply computed using

Bragg's rule. The stopping cross section for a molecule A_mB_n is given by

$$\varepsilon^{A_mB_n} = m\varepsilon^A + n\varepsilon^B, \qquad \text{II-12}$$

where ε^A and ε^B are the stopping cross sections for elements A and B, respectively. The stopping cross sections for $^4He^+$ ions in all elements are tabulated in reference 1.

References

1) W. K. Chu, J. W. Mayer, M-A Nicolet, Backscattering Spectroscopy (Academic Press, New York, 1978)

2) M. Cardona, L. Ley, Topics in Applied Physics, 26 (Springer-Verlag, New York, N.Y., 1978)

3) C. S. Fadley in Electron Spectroscopy: Theory, Techniques, and Applications, 2, C. R. Brundle and A. D. Baker, eds. (Academic Press, New York, N.Y., 1977)

4) T. A. Carlson, Photoelectron and Auger Spectroscopy (Plenum Press, New York, N.Y., 1975)

5) K. Siegbahn, C. Nordling, A. Fahlman, R. Nordberg, K. Hamrin, J. Hedman, G. Johansson, T. Bergmark, S-E. Karlsson, I. Lindgren, B. Lindberg, ESCA: Atomic, Molecular, and Solid State Structure Studied by Means of Electron Spectroscopy, Nova Acta Regiae Soc. Sci. Uppsaliensis, Ser. IV,20 (Almquist and Wiksells, Stockholm, 1967)

6) K. Siegbahn, C. Nordling, G. Johansson, J. Hedman, P-F. Heden, K. Hamrin, U. Gelius, T. Bergmark, L. O. Werme, R. Manne, Y. Baer, ESCA Applied to Free Molecules) (North-Holland, Amsterdam, 1969)

7) C. S. Fadley in Electron Emission Spectroscopy, W. Dekeyser, et al., eds. (Reidel, Dordrecht, Netherlands, 1973)

8) H. Busch, J. Electron. Spectrosc., 5, 463 (1974)

9) D. A. Shirley, Advan. Chem. Phys., 23, 85 (1973)

10) C. S. Fadley, S.B.M. Hagström, M. P. Klein, D. A. Shirley, J. Chem. Phys. 48, 3779 (1968)

11) C. S. Fadley, S.B.M. Hagström, J. M. Hollander, M. P. Klein, D. A. Shirley, Science, 157, 1571 (1967)

12) D. E. Eastman in Electron Spectroscopy, D. A. Shirley, ed. (North Holland, Amsterdam, 1972), 487

13) Y. Baer, Sol. St. Comm., 19, 669 (1976)

14) S. Evans, Chem. Phys. Lett., 23, 134 (1973)

15) J. L. Freeouf, G. W. Rubloff, P. S. Ho, T. S. Kuan, Phys. Rev. Lett., 43, 1836 (1979)

16) R. L. Martin, D. A. Shirley in Electron Spectroscopy: Theory, Techniques, and Applications, C. R. Brundle and A. D. Baker, eds (Academic Press, London, 1977), Vol. 2, Chapter 2.

17) C. S. Fadley, D. A. Shirley, Phys. Rev. A, 2, 1109 (1970)

18) R. L. Martin, D. A. Shirley, Phys. Rev. A, 13, 1475 (1976)

19) D. A. Shirley in Topics in Applied Physics, M. Cardona and L. Ley, eds. (Springer-Verlag, New York, N.Y., 1978), Chapter 4

20) I. Lindau, W. E. Spicer, J. Electron Spectros., 3, 409 (1974)

21) C. J. Powell, Surf. Sci., 44, 29 (1974)

22) M. P. Seah, National Physical Laboratory, Electron Mean Free Path Versus Energy Compilation, Teddington, Middlesex, U.K.

23) M. P. Seah, W. A. Dench, Surface and Interface Analysis, 1, 2 (1979)

24) J. H. Scofield, J. Electron. Spectrosc., 8, 129 (1976)

25) B. F. Lewis, F. J. Grunthaner, to be published

26) M-A. Nicolet in Nondestructive Evaluation of Semiconductor Materials and Devices, J. N. Zemel, ed. (Plenum Publishing Corporation, 1979), Chapter 11

CHAPTER III

DYNAMIC MONITORING OF THE NICKEL/SILICIDE AND SILICON/SILICIDE INTERFACES

A. INTRODUCTION

Several studies concerned with compound formation due to solid phase reactions at metal-semiconductor interfaces have recently appeared. In contrast to various theoretical studies which have modeled the interface as abrupt, these studies have concluded that there exists an interfacial layer with a structure or composition different from either the pure metal or the bulk semiconductor. The current understanding of the chemical properties within this interfacial layer is still rather primitive. In particular, such fundamental questions as the nature of the chemical bonding at the interface and the stoichiometry of the compounds formed have yet to be answered. The experimental results presented in this chapter will address these fundamental questions.

Examination of the chemistry occurring at the metal/semiconductor interface is an experimental challenge that has been met with varying degrees of success by researchers utilizing a variety of electron spectroscopies such as Auger electron spectroscopy (AES)[1-3] and ultraviolet photoelectron spectroscopy (UPS).[4] Because the interface is typically buried under silicide or metal layers hundreds of angstroms in thickness, these surface sensitive studies have employed two basic experimental approaches.

One approach involves the use of AES in conjunction with *in situ* ion sputtering to erode away the overlayer structure. The interpretation of the depth profiles obtained using ion bombardment sputter etching is severely compromised by complications induced by the sputtering process. It has been well established that upon bombardment of a multicomponent surface with energic ions, the species with the highest effective sputtering yield will be preferentially removed. This results in a layer of altered stoichiometry on the surface of the ion sputtered solid. Typically, there is an enrichment of the species with the lowest effective sputtering yields. Ion bombardment also alters the surface microtopography which can affect interpretation by degrading the depth resolution, reducing the sensitivity of the Auger experiment, and modifying the ion sputter rate. Recoil or knock-on implantation, which is a process by which an atom is driven deeper into the solid by collision with the incoming ion, has the effect of broadening the interfacial region as well as altering its composition. The above complications introduced by ion sputtering result in alteration of the chemical state of the interfacial layer under investigation. Consequently, conclusions drawn in such studies are compromised by the sputter-sectioning technique.

To avoid the chemical and structural perturbation of the interface encountered with sputter profiling, a second experimental approach has been used in several recent studies.[1,4,5] These studies approximate the interface by evaporating multiple monolayers of a metal on silicon. The development of the interfacial properties is monitored

as the first few atomic layers are deposited using either AES or UPS. This approach has been considerably more successful than the ion-sputtering approach. The primary disadvantage is that it is only an approximation of the true interface. The true interface is bounded on both sides by an extended solid. The presence of this extended solid on each side of the interfacial region will impose different bonding restrictions on the interface atoms as compared to the presence of a vacuum on one side. Further details concerning the thin-film deposition approximation to the true interface and its implications for bonding and stoichiometry at the interface are discussed in Chapter IV.

In this chapter, a new approach for examining the chemical nature of the metal-semiconductor interface is developed. It is a dynamic approach which exploits the exponential attenuation of photoemission intensities to examine the advancing silicide growth front during *in situ* formation of the metal silicide. The approach does not suffer from the disadvantages found in the conventional ion sputering or thin-film deposition techniques discussed previously. Instead, it allows examination of a realistic interface with an extended solid on each side and without the chemical and structural perturbations caused by depth profiling methods.

To illustrate the procedure, consider the reaction of a nickel film on silicon. Rutherford backscattering studies have shown that the formation of the silicide proceeds as a planar front as shown in Figure 1. Upon heating, an initial phase Ni_2Si forms at the Ni/Si interface.

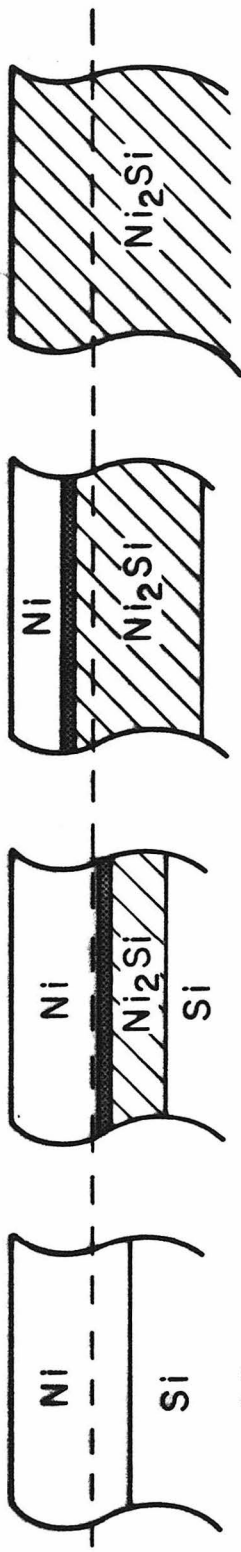

Figure 1: Schematic representation of the progression of the Ni/Ni_2Si interface.

With continued heating, the width of the silicide layer increases until the Ni film has been consumed. This first phase is the highest congruently-melting compound near the lowest eutectic of the possible compounds which can form from a metal/silicon couple.[7] Once the nickel film has been consumed, a second less metal-rich phase NiSi can develop at the Ni_2Si/silicon interface. Formation of the second phase generally requires a higher temperature or longer heating time than the initial phase. This second compound continues to increase in width at the expense of the first until the latter is entirely consumed. During the various phase growths, two compounds coexist, but as discrete layers. If the temperature is elevated even further, a third silicon rich phase $NiSi_2$ will begin to develop at the NiSi/silicon interface. This phase will proceed as above in a planar fashion to consume the NiSi phase.

In these experiments, the progression of the first metal rich phase Ni_2Si will be examined. The planar progression of the phase allows one to examine the Ni/Ni_2Si interface by utilizing the finite information depth of XPS. The exponential attenuation of photoemission intensities establishes an effective observation depth as shown in Figure 1. If the initial Ni film is sufficiently thick, only photoemission signals from the Ni metal will be detected. By monitoring the Si photoemission signals as the sample is heated *in situ*, one can examine the emerging Ni/Ni_2Si interface and bulk Ni_2Si region as they advance into the observation depth. It will be demonstrated that this emerging signal, when compared to the signal from the final

Ni_2Si phase, can provide considerable information concerning not only the chemical nature of the interface but also the physical width of the transition region.

An estimation of the effective observation depth is necessary if one is to be convinced that the emerging interface signal is representative of the true interface; that is, the interface with an extended solid on both sides. In photoemission spectroscopy, the signal intensity from deep lying atoms diminishes as $\exp(-x/\lambda)$, where x is the depth of the atom from the surface and λ is the electron elastic mean free path length.[8] The mean free path λ is a function not only of the kinetic energy of the emitted electron but also of the solid matrix through which it must traverse. It has been determined that with the instrumentation used in these experiments, a substrate beneath a metal overlayer of thickness 2-3 λ can be readily detected. A more detailed discussion of this point may be found in Chapter II where photoelectron peak intensities are considered in more detail, including the influence or such factors as instrumental sensitivity and signal/background ratio. Assuming an escape depth of 15 Å for a metallic overlayer, one finds that in the example discussed above the emerging Si signal will be first detected when approximately 30-45 Å of the Ni overlayer still remains. If the Si/Ni_2Si interface was examined through a Si overlayer, the effective observation depth would be considerably greater due to the large electron mean free path in Si of $\sim$25 Å. The emerging signal should in this case be detected with a 50-75 Å Si overlay present. Clearly, in both cases a

sufficient overlayer exists that one may conclude the interface signal is representative of the true interface. The observed overlayer thickness in each experiment will be discussed later and will be shown to be consistent with these estimations.

To further illustrate the concept behind the dynamic interface experiments, one can examine the evolution of all the available photoemission core level signals as the silicide growth front advances into the observation depth of the spectroscopy. To illustrate the typical features observed in XPS spectra, Figure 2 shows a broad energy spectrum of 1280 eV obtained from a bulk Ni_2Si specimen. The major photoelectron lines are labelled according to their level of origin. In addition, several Auger peaks are observable (O KLL, Ni $L_3M_{2,3}M_{2,3}$, Ni L_3 $M_{2,3}V$, Ni L_3 VV) which are generally broader and more complex in structure than the photoelectron peaks. The oxygen and carbon peaks in the spectrum are due to the presence of a thin surface oxide and overlayer of carbon containing contaminants. The stepped appearance in the background to the low kinetic energy side of each electron peak is the result of electrons that have suffered extrinsic energy losses.[10] These are electrons that are initially excited to the same energy as those in the sharp primary peaks, but have lost energy due to inelastic scattering during their passage through the solid. These inelastic background tails may also display structure if appropriate excitations in the solid are possible, such as the excitation of collective valence electron oscillations (plasmons).[11] The inelastic tails below the C 1s and O 1s peaks are extremely weak relative to the other electron

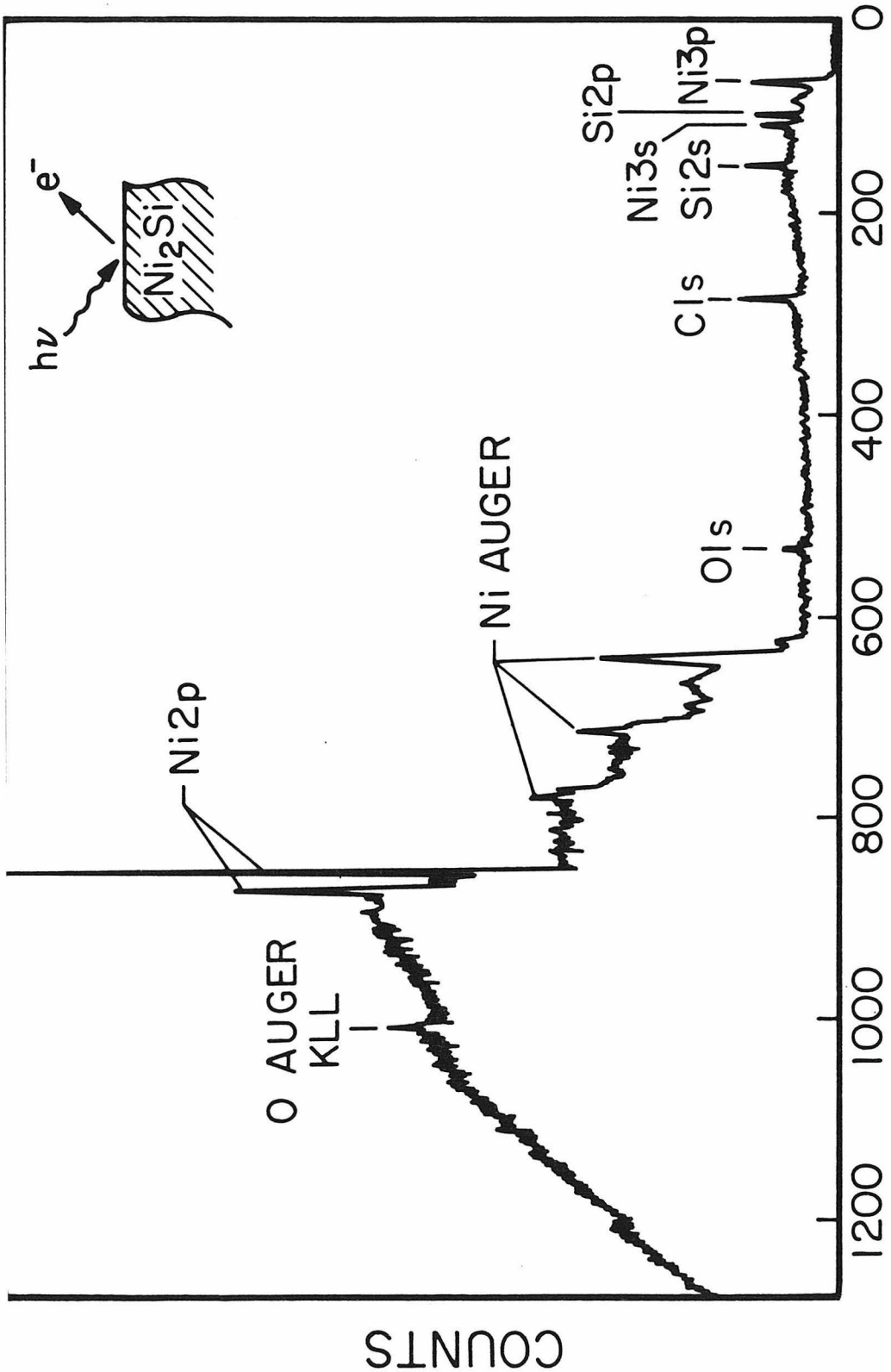

Figure 2: Wide scan XPS spectrum of a Ni_2Si specimen.

peaks because the layers responsible for these signals are thin and thus allow the photoelectrons to escape with a low probability of being scattered. The sharp decrease in the background starting at ∿1000 eV binding energy is due to a decrease in the instrument transmission function for low kinetic energy electrons.

In Figure 3, broad energy scans are plotted for various stages during the *in situ* growth of Ni_2Si. The sample consists of ∿1500 Å Si deposited on ∿1000 Å Ni which in turn was deposited on a thermally oxidized Si wafer (∿1000 Å SiO_2). The SiO_2 acts as a barrier to prevent the Si substrate from participating in the reaction. The initial Si overlayer is sufficiently thick that only photoemission signals from the Si are detectable, as shown in Figure 3a. The fluorine signal is due to residue left from the sample cleaning procedure which involves the use of HF to remove any surface oxides that may have formed during sample transport. The oxygen signal is due to a residual SiO_2 surface oxide (< monolayer) or to residual water or ethanol which is also part of the cleaning procedure. The weak peak structure on the high binding energy side of the Si 2p and Si 2s core lines are extrinsic energy loss peaks attributable to plasmons. Upon heating the sample *in situ* to 275°C the silicide begins to form as shown in Figure 1. The wide energy scan corresponding to the first detectable Ni 2p signal due to the advancing Si/Ni_2Si planar growth front is shown in Figure 3b. The characteristic Ni 2p core lines are very weak at this point because of attenuation by the remaining Si overlayer. The inelastically scattered background from the Ni 2p electrons contributes

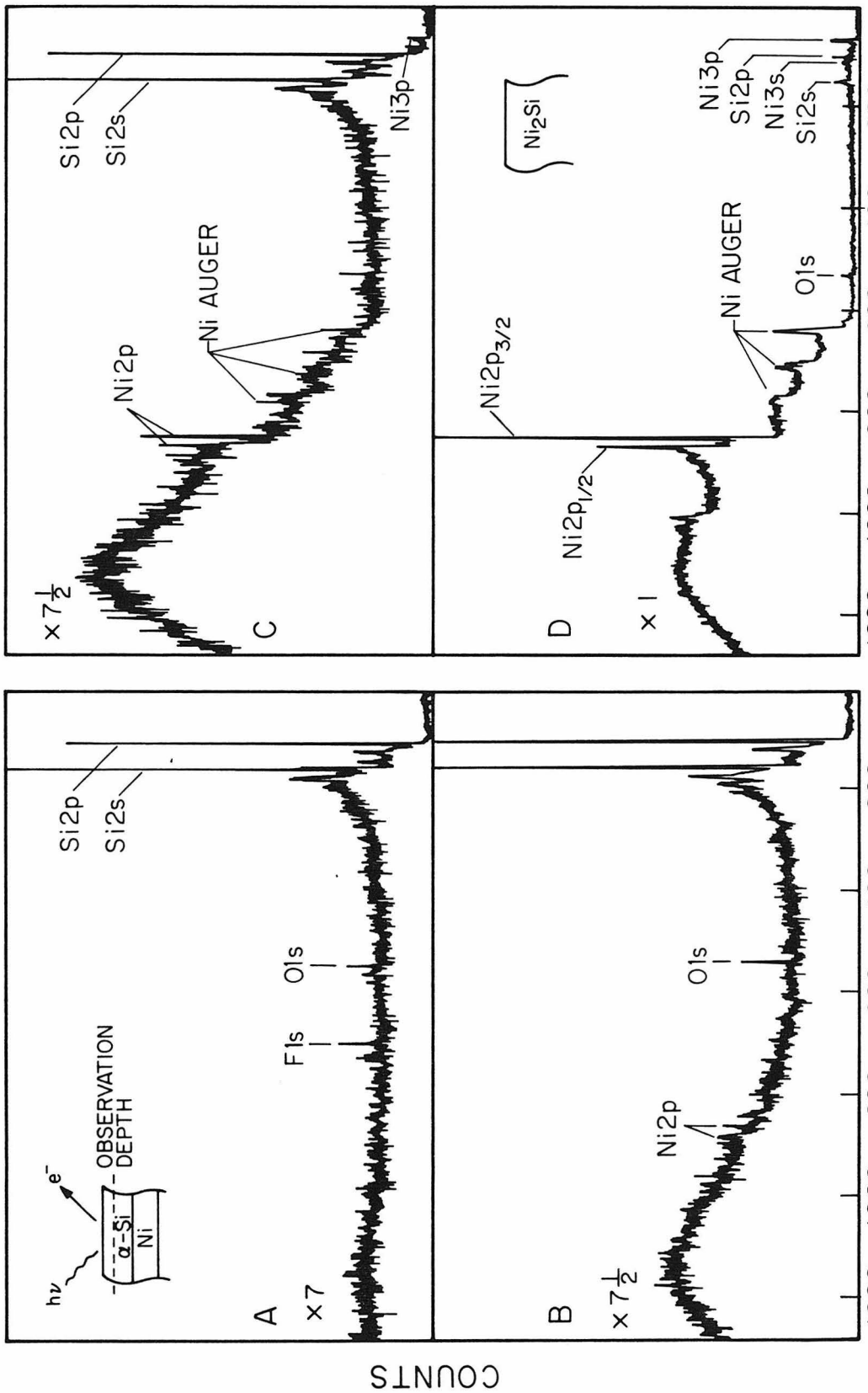

Figure 3: Wide scan XPS spectra illustrating the evolution of the Ni and Si core lines as the Ni_2Si growth front advances into the observation depth.

the broad hump at the high binding side of the spectra. Because the Ni atoms are relatively deep within the solid, there is a high probability that a given Ni 2p photoelectron will undergo scattering before escaping the solid. The corresponding Si 2p and Si 2s signals have lost intensity because the atomic density of the Si atoms within the observation depth has decreased. The residual fluorine contamination signal is no longer present due to its desorbtion upon heating. The oxygen signal is still present and has increased in intensity. This is a result of the accumulation of the residual oxygen contamination within the evaporated Si overlayer at the Si/Ni_2Si growth front. This phenomenon is discussed in more detail in Chapter V. As the Si/Ni_2Si growth front continues to proceed toward the sample surface, the Ni 2p core lines become more intense and other less intense Ni lines such as the Ni 3p and the Ni Auger manifold are observable as shown in Figure 3c. Finally, in Figure 3d, the Si overlayer has been completely consumed and only bulk Ni_2Si is present within the observation depth of the spectroscopy.

Because several silicide phases are possible with a thin film Si-Ni couple, it is important to verify that the end phase in these experiments is indeed Ni_2Si. Quantitative analysis is difficult with XPS. One problem is the lack of information about photoelectron cross-sections. A more serious problem is the satellites generated by various multielectron processes during photoemission.[12] The area of these satellites must be included with the area of the primary core line to accurately assess composition. The satellites are often

weak and broad and merge into other energy loss structures, making determination of their areas difficult. To avoid the problems that plague XPS, Rutherford backscattering spectroscopy (RBS) has been used to follow the progression of the silicide growth front and to provide identification of the final phase. RBS is ideally suited to complement the information obtained from XPS. It provides quantitative information on the depth distribution of atomic species through a kinematic consideration of the scattering of incident monoenergetic ions off atoms within a solid. Through analysis of the scattered ion energy, and a knowledge of the relevant scattering and stopping cross sections, one may quantitatively determine the atomic composition of a solid as a function of depth. In Figure 4 is shown the $^4He^+$ backscattered spectra corresponding to the photoelectron spectra in Figure 3. It can be seen that when the first Ni 2p signal is observed by XPS (Figure 3b), there still remains a detectable Si overlayer in the backscattered spectra. From the relative intensities of the signals in the backscattered spectra, one finds it is the Si/Ni_2Si interface that has progressed into the XPS observation depth, as expected. When no further changes occur in the Ni 2p signal intensity (Figure 3d), the corresponding backscattered spectrum indicates the reaction has completely consumed the Si overlayer to form the phase Ni_2Si. Some Ni metal still remains at the SiO_2/Ni interface, but it is too deep to be detected by XPS.

As discussed in Chapter II, the exact binding energy of the photoelectron signal reflects changes in the valence charge density

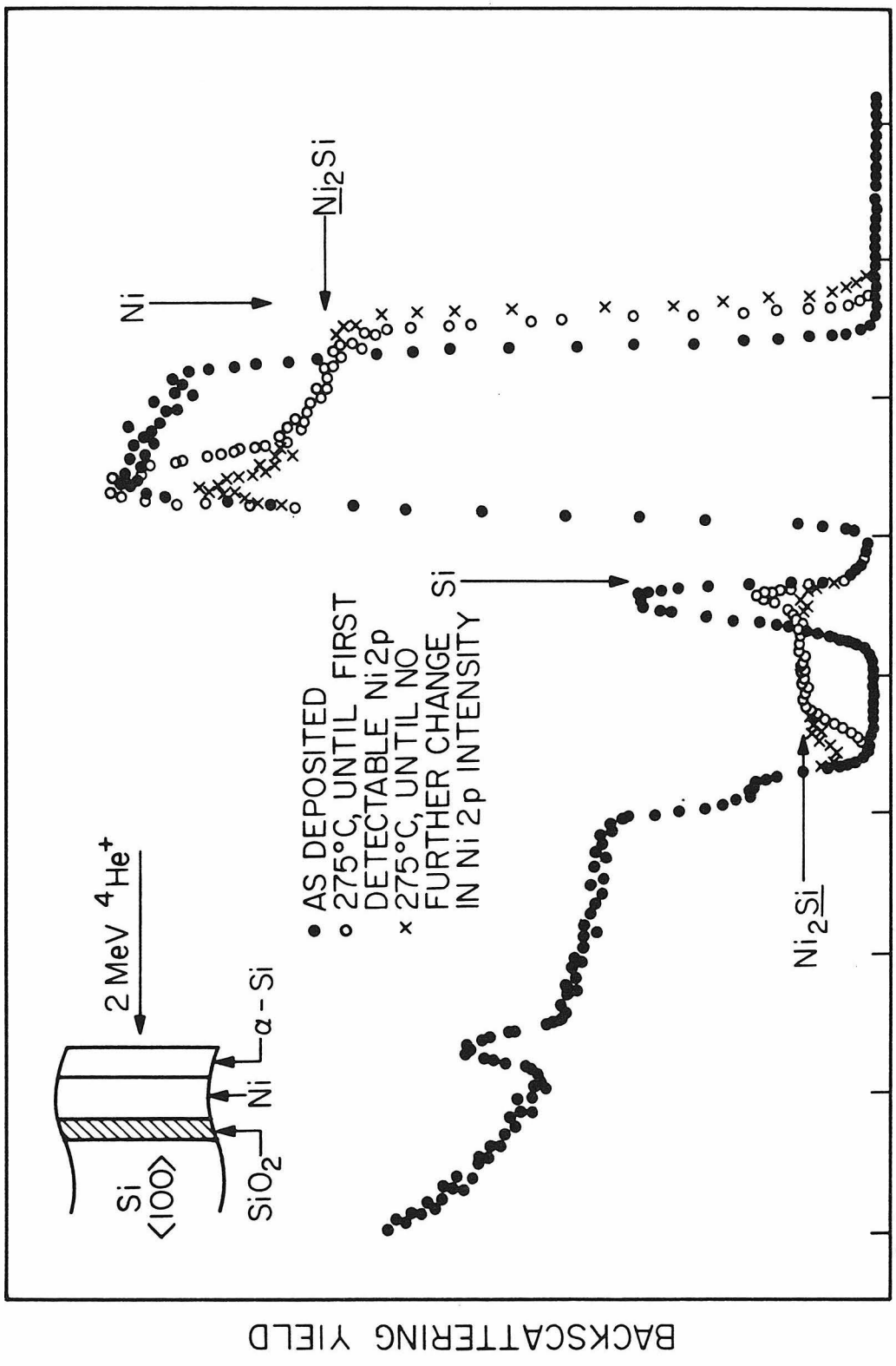

Figure 4: $^{4}He^{+}$ backscattered spectra showing the progression of the Ni_2Si reaction front.

around the atom from which it originates. This directly yields information concerning the chemical environment of that atom. In the following sections, the details of the evolution of the Ni 2p and Si 2p core level binding energies as the silicide growth fronts progress toward the solid surface are presented.

B. EXPERIMENTAL

Three types of samples were prepared in the course of the work reported in this chapter: Ni films on <100> Si, Ni films on amorphous Si (α-Si), and α-Si films on evaporated Ni. This allowed the investigation of three distinct interfaces. They are the α-Si/Ni_2Si interface and the Ni/Ni_2Si interface with both crystalline Si and amorphous Si as the starting substrate. The details of the sample preparation are given below.

Crystalline Si <100> (n type, 1-10 Ω-cm) and thermally oxidized Si wafers (∿1000 Å SiO_2, 1000°C) were used as the substrates for the deposition of thin Ni and Si films. Prior to being loaded into the vacuum system for evaporation, the SiO_2 substrates were cleaned ultrasonically with tricholoroethylene (TCE), acetone, and methanol and then rinsed in deionized water. In order to examine the α-Si/Ni_2Si interface, ∿1500 Å Ni was deposited on SiO_2 substrate, followed by a ∿1000 Å Si. Conversely, to study the Ni/Ni_2Si interface beginning with a α-Si substrate, ∿1500 Å Si was deposited on a SiO_2 substrate followed by ∿1000 Å Ni. A background pressure of 5×10^{-7} Torr was maintained during the evaporations. The Si and Ni films were evaporated using an e-beam source at a rate of 40 and 20-35 Å/sec, respectively.

The Ni/Ni_2Si interface starting with a crystalline substrate was studied by preparing a sample with 500 Å Ni deposited on <100> Si. The Si substrate was cleaned ultrasonically with TCE, acetone, and methanol and then rinsed with deionized water. Just prior to loading for evaporation, the substrate was etched in dilute HF and rinsed again in deionized water. The Ni was e-beam evaporated at ∿20-35 Å/sec with a background pressure of $\sim 5 \times 10^{-7}$ Torr.

Prior to examination by XPS, surface oxide layers that had formed during sample transport had to be removed. The nickel oxide that formed on the surfaces of the Ni/α-Si and Ni/<100> Si samples was etched off under a N_2 atmosphere by spinning the sample at 3600 rpm and adding dropwise 500 µl of 1:1 HCl in ethanol, followed by 500 µl of ethanol. The SiO_2 layer that formed on the α-Si/Ni samples was removed with several drops of 1:10 HF in ethanol using the same spinning technique. The sample inlet port of the spectrometer is directly connected to the N_2 drybox. Consequently, no additional oxygen contamination occurred after etching. This removal of the contaminant oxide overlayers is extremely important since the oxide not only severely attenuates the emerging interface photoelectron signals, but it also obscures any chemical shifts that occur upon silicide formation. Figure 5 compares the Ni 2p region of an evaporated nickel surface before and after several etches with an HCl in ethanol solution using the spinning technique described above. The native nickel oxide that forms during air exposure is approximately ∿20 Å thick and its attenuation effect on the underlying nickel metal can be seen in Figure 5a. The Ni $2p_{3/2}$

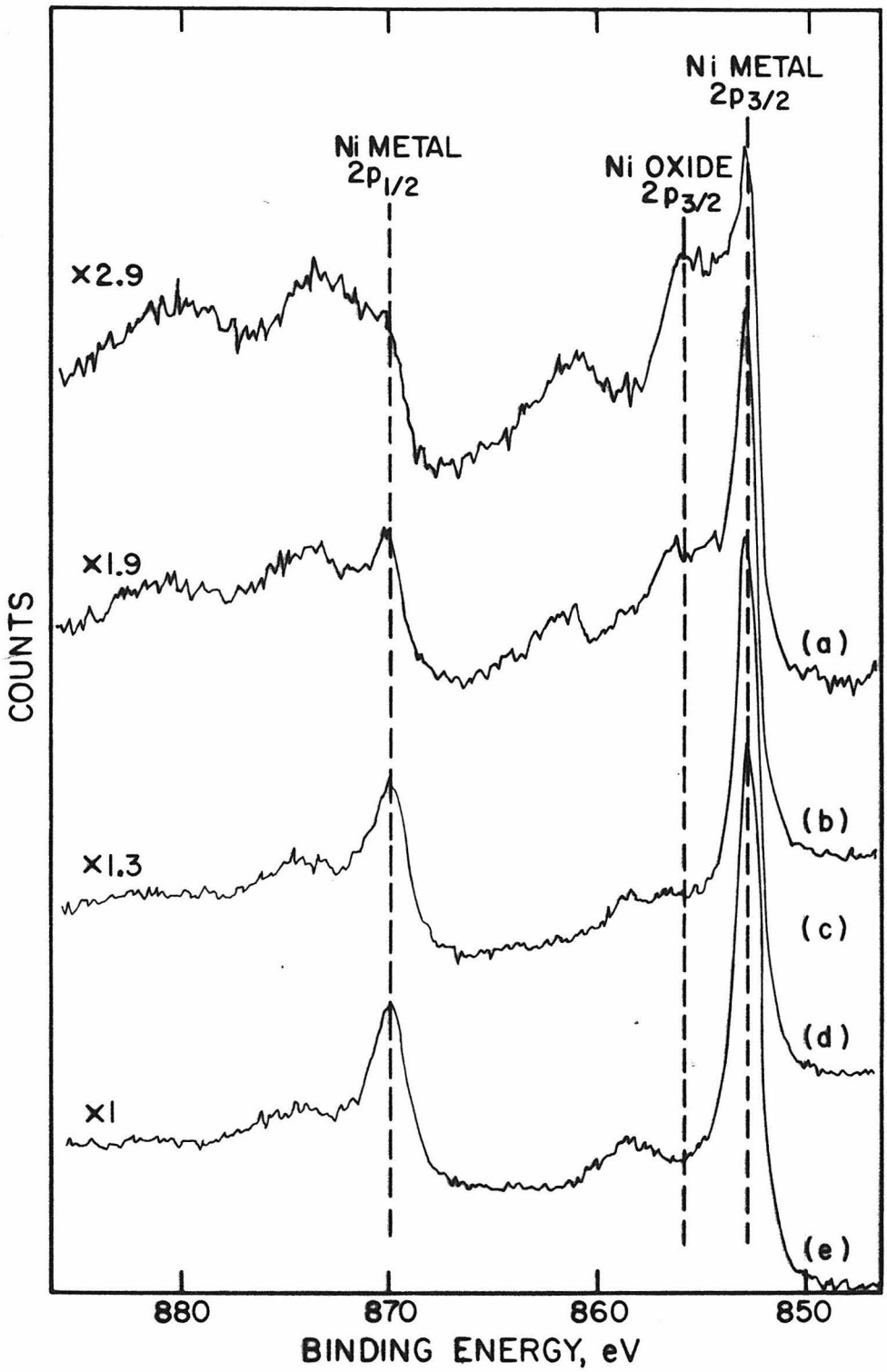

Figure 5: Ni 2p XPS spectra illustrating the chemical removal of the nickel oxide overlayer.

oxide peak is almost as intense as the Ni $2p_{3/2}$ metal peak and, more importantly, the presence of this oxide peak interferes with any Ni 2p signal emerging on the high binding energy side of the Ni metal peak. As more of the Ni oxide is sequentially removed, the spectra shown in Figures 5b-5d are obtained. In Figure 5d, no Ni oxide is observable and the Ni metal signal shows a 3-fold increase in intensity. A small amount of carbon and residual oxygen possibly due to absorbed water and solvent are the only detectable contaminants (<1 monolayer). The broad peaks at 862 eV and 859 eV correspond to intrinsic energy loss satellites in Ni oxide and Ni metal, respectively.

After establishing sample surfaces that are free of oxide and carbon overlayer contamination, the various Ni and Si core and valence levels were monitored as the samples were heated *in situ* in the analyzer chamber of the XPS spectrometer. The vacuum inside the chamber during heating was better than 2×10^{-9} Torr. The samples were cooled to $298^{o}C$ at various intervals to allow for extended data accumulation periods. After XPS analysis, the composition of the resulting silicide was determined using 2·0 MeV $^{4}He^{+}$ backscattering.

C. RESULTS AND DISCUSSION

1. The Bulk Ni Silicides

An understanding of the nature of the chemical bonding within the bulk Ni silicides is required to interpret the photoemission spectra obtained for the various interfaces found in the Ni-Si system. The Ni2p spectra of Ni metal, Ni_2Si, and NiSi are shown in Figure 6. To

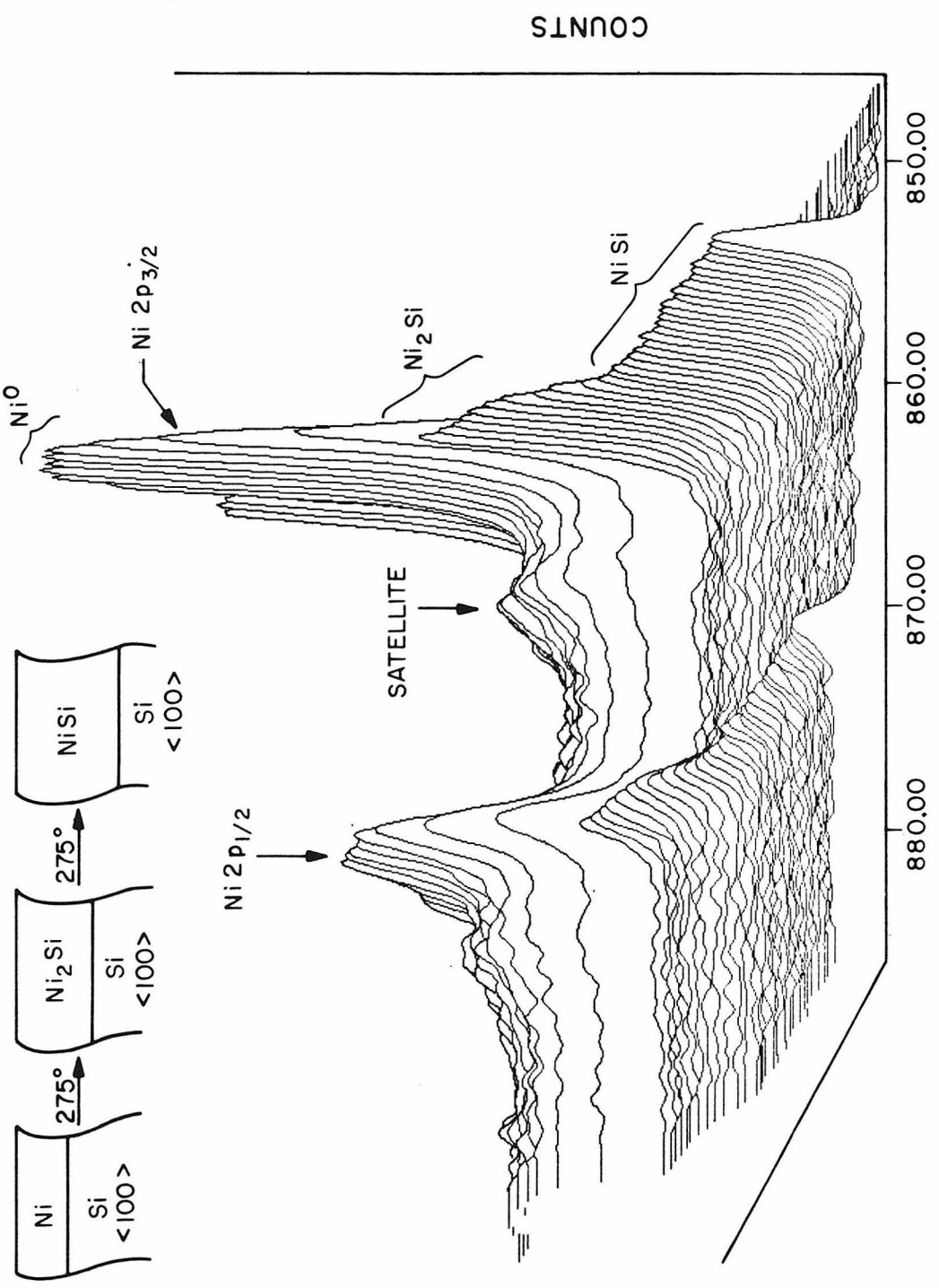

Figure 6: 3-dimensional plot of the Ni 2p XPS spectra. The Z-axis represents time. The spectra illustrate the sequential planar growth of the bulk nickel silicides.

obtain these spectra, a Si substrate with a 500 Å Ni overlayer was heated to 275°C in the analyzer chamber of the XPS spectrometer. The native Ni oxide was removed prior to heating as discussed earlier. The spectra were taken at approximately five minute intervals. The progression of the Ni silicide phases as diagrammed in Figure 1 is clearly demonstrated by the intensity changes in the Ni 2p region in Figure 6. The initial increase in the Ni^{o} signal after ∿15 minutes of heating is due to the desorbtion of the residual oxygen and carbon overlayer contaminants. As the Ni_2Si and NiSi phases advance within the observation depth of the spectroscopy, the Ni 2p intensities decrease. This is expected since photoemission intensities are proportional to the atomic density of the emitting atoms. The satellite line on the low kinetic energy side of the Ni $2p_{3/2}$ and Ni $2p_{1/2}$ core lines is characteristic of metallic nickel and is seen to decrease in intensity as the silicide phases are produced. The spectral progression demonstrates clearly defined Ni_2Si and NiSi phases. The Ni $2p_{3/2}$ binding energy corresponding to each of these spectra is shown in Figure 7. The Ni metal binding energy is observed at 852.4 eV. As the Ni_2Si phase advances into the observation depth, the Ni $2p_{3/2}$ signal shifts 0.6 eV upfield to 853.0 eV. The Ni $2p_{3/2}$ core line for NiSi shifts an additional 0.5 eV upfield to 853.5 eV. The Si 2p core level lines corresponding to Ni_2Si and NiSi fall at binding energies of 98.85 eV and 98.75 eV, respectively.

An increase in the Ni 2p binding energy with a corresponding decrease in the Si 2p energy occurs as the sample progresses from Ni_2Si to NiSi. This indicates more Ni→Si charge transfer in NiSi

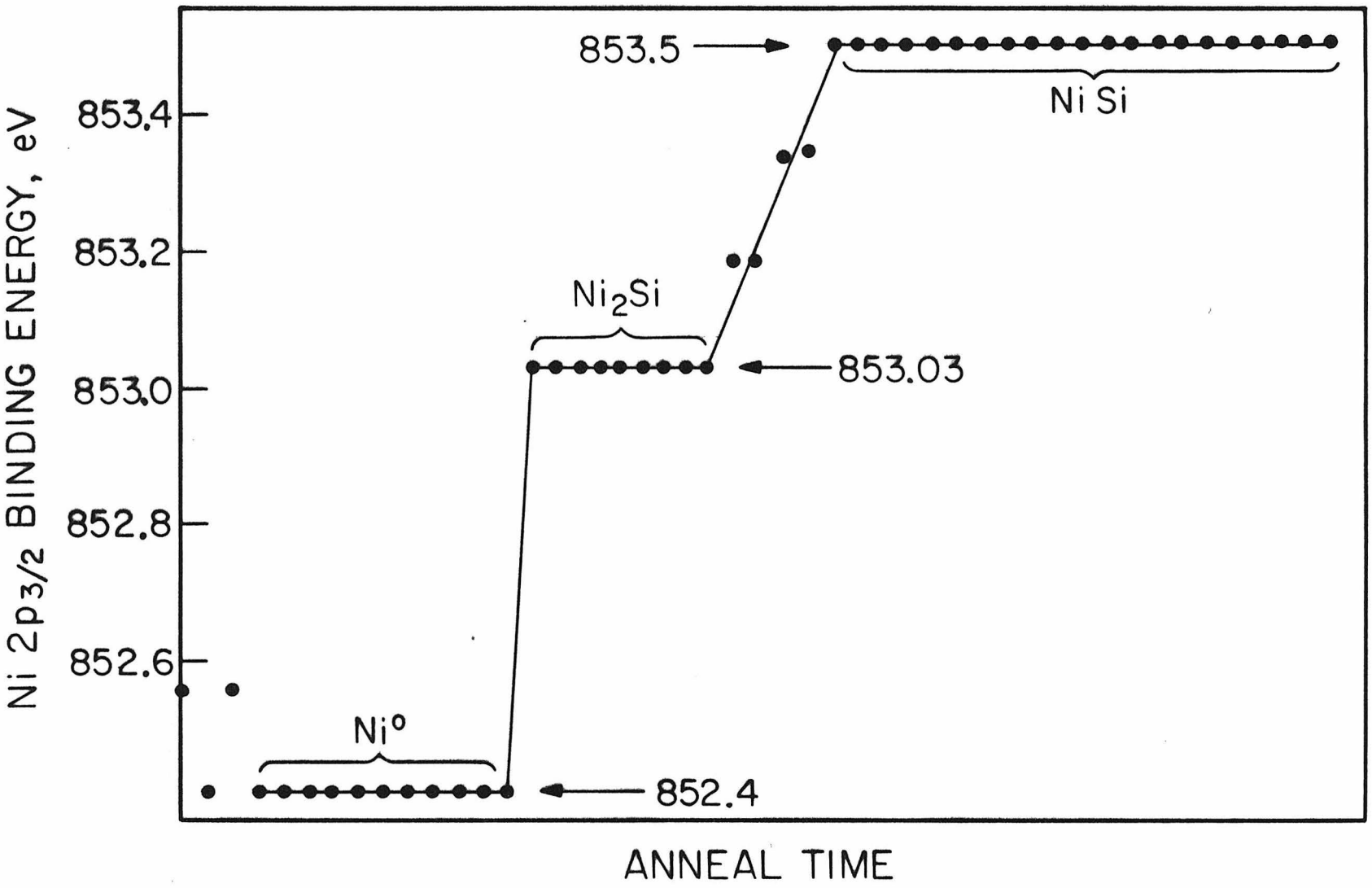

Figure 7: Plot of the peak maxima in the Ni 2p region corresponding to figure 6.

relative to Ni_2Si. Further, the Si 2p level in both Ni_2Si and NiSi falls at a lower energy than that found for n-type silicon. This indicates more electron density is present on the Si atom in the silicides than on the sp^3 hybridized Si of pure silicon. The Allred and Rochow electronegativities for Ni (1.75) and Si (1.74) suggest the ionic character of the Ni-Si bond is negligible and does not contribute to the charge transfer. The increased charge density around Si observed upon Ni-Si bonding is consistent with donation from the filled d orbitals of Ni to the empty d orbitals of Si. This postulated $(d\rightarrow d)_\pi$ interaction is reasonable in light of the extensive literature reporting analogous bonding between group IV elements and transition metals. It is well known that the empty d orbitals of Si, Ge, and Sn have a role in the chemistry of these elements, but only in the last 10-15 years has there been evidence presented for strong π interactions with transition metals. Several infrared studies of the carbonyl stretching region in silicon cobalt tetracarbonyls as well as molecular orbital calculations on these compounds[19] have led to the conclusion of partial $(d\rightarrow d)_\pi$ double bond character in the Si-Co bond due to overlap of filled $3d_{xz}$ and $3d_{yz}$ Co orbitals with empty $3d_{xz}$ and $3d_{yz}$ Si orbitals. Additional infrared studies[20-24] of other transition metal carbonyls with the group IV elements Si, Ge, and Sn suggest the presence of $(d\rightarrow d)_\pi$ interaction between the group IV element and the transition metal. Further agreement with this bonding concept is found in nuclear quadrupole resonance studies[25] and also in dipole moment work which demonstrates that the distribution of charge in the metal-silicon bond is $M(\delta^+)$-$Si(\delta^-)$. In addition to the spectroscopic studies mentioned

above, x-ray structural data for numerous compounds with Si-M bonds (where M = Fe, Co, Mn, Rh, Pt) are consistent with significant $(d\rightarrow d)_{\pi}$ interactions.[26-27] The support for the $(d\rightarrow d)_{\pi}$ partial double bond character in these studies is derived from the fact that the observed metal-Si distances are all substantially shorter than bond lengths predicted from the sum of the appropriate covalent radii.

The known structures for Ni_2Si and NiSi can be used to support the postulated $(d\rightarrow d)_{\pi}$ electron donation from Ni to Si. To determine whether the observed Ni-Si bond is shorter than that expected for a single bond, as would be the case if significant $(d\rightarrow d)_{\pi}$ character was present in the bond, an estimate of the hypothetical single bond length must be made. Prediction of the single bond length is difficult and the simple sum of the covalent radii cannot be expected to correlate well with the observed bond lengths for several reasons. First, bond lengths depend upon the bond number n. Second, orbital hybridization plays an important role. The dependence of the bond length on the bond number is given by the Pauling expression[28]

$$D(n) = D(1) - 0.60 \log n \qquad \text{(III-1)}$$

where n is the bond number and D(1) is the single order bond length (n=1). The single order bond length, between atoms A and B may be calculated by correcting the sum of the single order covalent radii for differences in electronegativity.[28]

$$D(1)_{A-B} = R_A + R_B - C \left|X_A - X_B\right| \qquad \text{(III-2)}$$

where R_A and R_B are the single order covalent radii, X_A and X_B are the electronegativities of atoms A and B, respectively, and C is the Schonmaker-Stevenson coefficient. This expression is valid only when the single order covalent radii correspond to the same orbital hybridization as that found between atoms A and B in the structure of interest. Thus, hybridization effects are very important. It is known, for example, that the single bond radius decreases rapidly with increasing amount of d character in the bond orbitals for the transition metals.[28]

The typical application of Pauling's empirical expressions involve the following procedure: 1) calculation of the single order bond length, D(1), of interest using III-2, 2) determination of the appropriate bond numbers, n, from the valency and coordination number of the bonding atoms in the structure of interest, and 3) estimation of the bond lengths for the structure of interest using III-1. If the calculated and observed bond lengths agree within the limits of uncertainty, the bonding character is considered to be adequately described.

The above procedure was used to examine the bonding in NiSi and Ni_2Si. If the single order covalent radii of Ni (1.154 Å) and Si (1.173 Å) derived from pure silicon and nickel metal are used, agreement between the observed and calculated bond lengths can only be obtained by assuming a valency of 5.7 for Si and 6.3 for Ni in NiSi. In Ni_2Si, agreement requires a 3.8 valency for Si and a 6.2 and 5.9 valency for the two Ni atoms. Relative to the commonly accepted valencies of 4 for

Si and 6 for Ni, this corresponds to 2.8 and 0.6 excess electrons on Si and Ni, respectively, in NiSi. In Ni_2Si, it corresponds to a 0.4 and 0.2 electron deficiency on Si and on Ni, respectively, and a 0.4 electron excess on the second Ni atom. These results are not consistent with the observed XPS shifts found for the Ni and Si core lines in these compounds. Furthermore, the extremely large valency for Si is chemically unreasonable. We take this as evidence that hybridization effects are important and must be taken into consideration. This is further supported by examination of the structures[29-32] (Figures 8a,b) which suggest qualitatively the hybridization required for the Si and Ni bonding orbitals for the particular geometries involved. For example, in Ni_2Si, the central silicon atom in Figure 8a is bonded strongly to 3 Ni atoms in the same plane and to a total of 6 other Ni atoms in planes above and below. This suggests the Si bonding consists of something more like $(sp^2 + p)$ rather than sp^3. There are two types of Ni sites in the structure (denoted I and II in the Figure). The longer NiII-Si bond lengths (compared to NiI-Si) and the shorter NiII-NiII bond lengths (compared to NiI-NiI) are consistent with NiI bonding via d^2sp^3 hybridization and NiII with perhaps $(dsp^3 + d)$. If one includes $(d \rightarrow d)_\pi$ interactions, then the Si bonding may be described as $(sp^2 + p + d)$. The above descriptions are, of course, idealized and can only be thought of as a first-order approximation to the orbital hybridization found in the actual distorted compounds.

The incorporation of hybridization into an estimation of single bond radii is difficult. Empirical equations relating the single bond

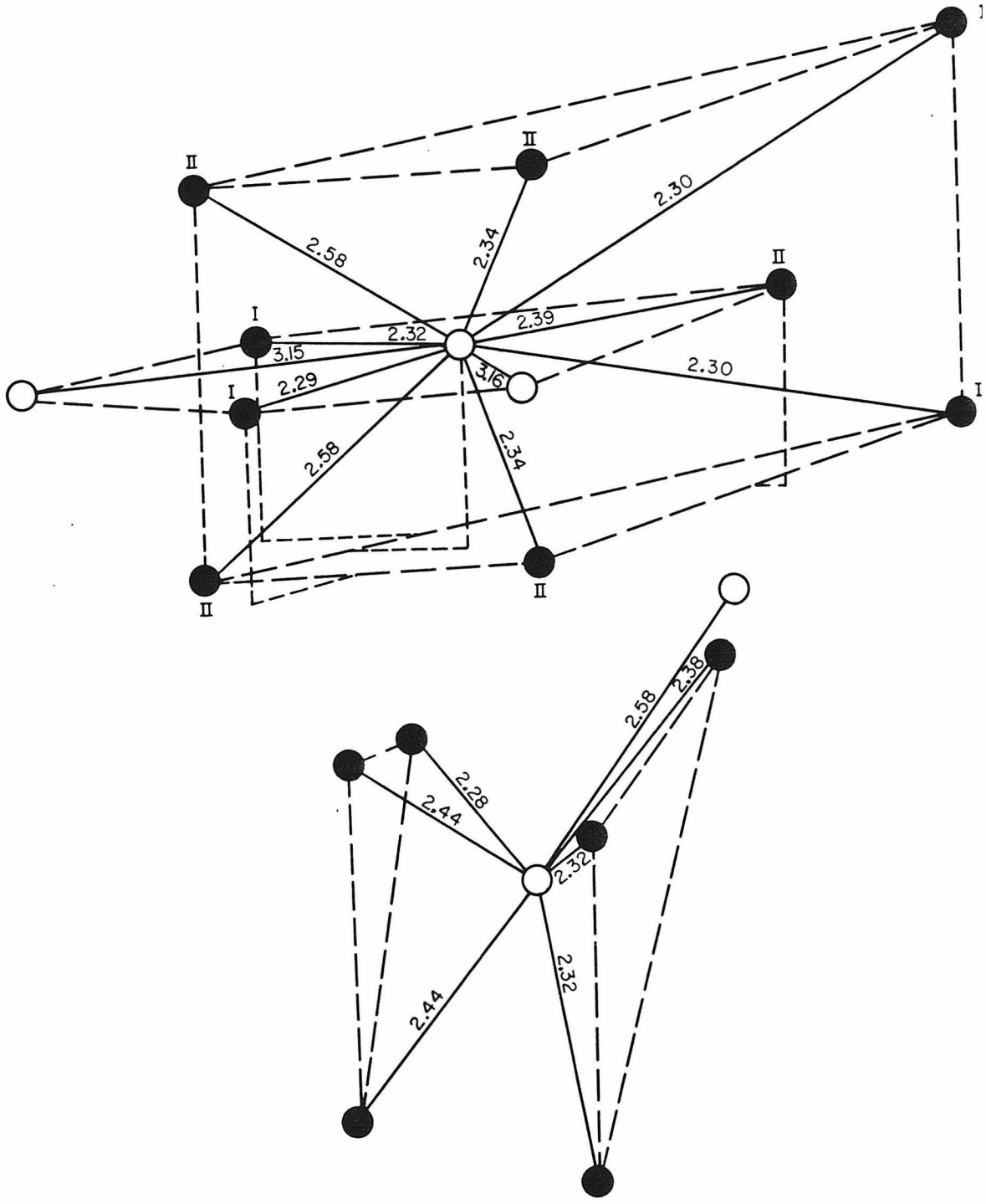

Figure 8: Coordination environment for the Si atom in Ni_2Si (upper drawing) and NiSi (lower drawing). Closed circles correspond to Ni atoms.

radius of a transition metal to the degree of hybridization of the bonding orbitals have been formulated, but only for a limited number of metals. The approach we have taken, in effect, is to reverse the procedure outlined previously. That is, assuming a reasonable valency for Ni and Si, we have determined the Si and Ni single bond radii necessary for agreement between the observed Ni-Si bond lengths in NiSi and Ni_2Si. It should be noted that the observed bond lengths for these compounds have been calculated using the atom coordinates for the unit cells.[29-30] Our calculated interatomic distances are slightly different from those reported in the literature and are used here because of the numerous typographical errors and inconsistencies in the bond lengths published in the structure reports.[33-34] Assuming normal Ni and Si valencies of 6 and 4, respectively, agreement between the observed and calculated bond lengths for Ni_2Si can be obtained with R_{Si} = 1.19 Å, R_{NiI} = 1.12 Å, and R_{NiII} = 1.16 Å. These results are tabulated in Table 1. In NiSi, a Ni valency of 6 and Si valency of 4 lead to radii that are physically unreasonable and inconsistent with the XPS shifts (1.00 Å for Si and 1.25 Å for Ni). Only if the valencies are made equal, $V_{Si} = V_{Ni} = 5$, can a reasonable agreement be obtained. For this situation, we calculate R_{Si} = 1.21 Å and R_{Ni} = 1.07 Å. These results are tabulated in Table 2. When compared to the single order covalent radii for Ni (1.154 Å) and Si (1.173 Å) obtained from pure silicon and nickel metal, these derived radii indicate that charge is being transferred from Ni to Si, supporting the postulated $(Ni\ 3d \rightarrow Si\ 3d)_{\pi}$ interaction. In addition, these radii are consistent with the XPS core level shifts obtained for NiSi and Ni_2Si. The large

decrease in the Ni radius in going from Ni_2Si ($R_{NiI,II}$ = 1.12 Å, 1.16 Å) to NiSi (R_{Ni} = 1.07 Å) is consistent with the large 0.5 eV shift observed in the Ni 2p photoemission spectra. The slight increase in the Si radius from Ni_2Si (R_{Si} = 1.19 Å) to NiSi (R_{SI} = 1.21 Å) is consistent with the smaller 0.1 eV shift observed in the Si2p spectra.

In summary, the proposal that $(Ni3d \rightarrow Si3d)_\pi$ interactions are responsible for the chemical shifts in the Ni2p and Si2p core levels in Ni_2Si and NiSi is supported by two observations. First, there exists an extensive body of literature providing evidence for the significant role of $(d \rightarrow d)_\pi$ interactions in the bonding between transition metals and group IV elements. Second, applying the empirical relationships derived by Pauling to the known Ni_2Si and NiSi structures leads to the conclusion that charge is transferred to Si from Ni upon Ni-Si bond formation and, further, that more charge is transferred in the case of NiSi than Ni_2Si. Since the ionicity of the Ni-Si bond is negligible, the only way Si may obtain a negative charge in excess of that found in pure Si is to utilize the empty 3d orbitals to accept electrons from the filled 3d orbitals of Ni. Thus, the notion of some $(d \rightarrow d)_\pi$ bonding character in Ni_2Si and NiSi is consistent with both the XPS data and the known crystal structures.

2. The Si/Ni_2Si Interface

The Si/Ni_2Si interface may be examined by monitoring a sample of Si deposited on Ni as a function of time during *in situ* silicide formation. The emerging photoemission signals from the Ni core levels

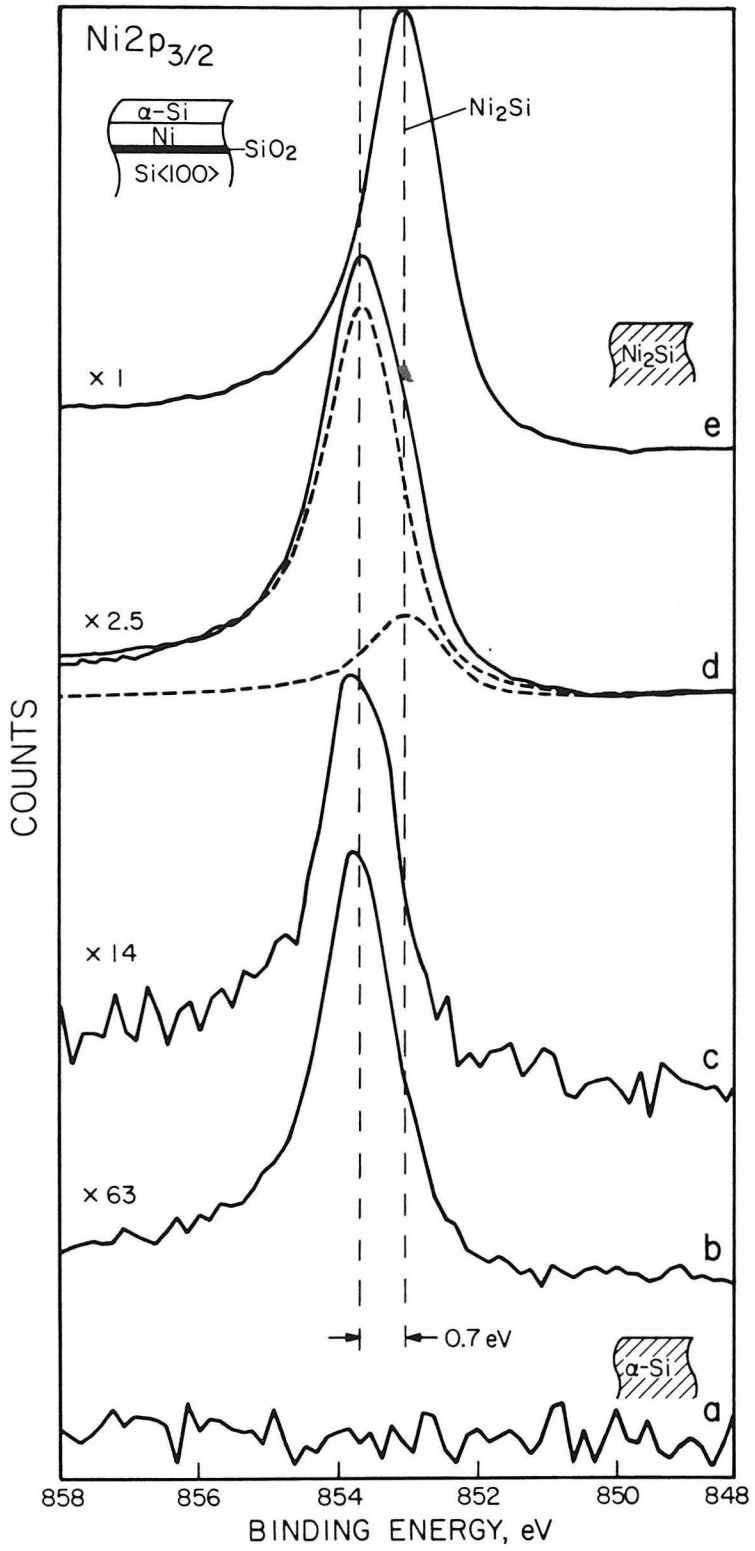

Figure 9: The Ni $2p_{3/2}$ spectra obtained as a function of time as the Si/Ni_2Si interface advanced toward the sample surface. The dashed spectra in (d) represent components determined using least square criterion. The lineshape determined for Ni_2Si in (e) was used for these component peaks.

allow one to interrogate the advancing Si/Ni_2Si reaction front. The gross features of the progression of the Ni and Si core lines for this sample are shown in Figure 3 and were discussed in detail in section A. To study the details of the core level chemical shifts in Ni as the interface and bulk silicide regions advance within the spectroscopy observation depth, the Ni $2p_{3/2}$ core line was examined. The Ni $2p_{3/2}$ line was chosen for three reasons: 1) it has a large photoelectron cross section compared to other Ni core lines ($\sigma_{Ni2p} = 22.2$, $\sigma_{Ni3p} = 2.2$, $\sigma_{Ni3s} = 0.9$), 2) it is a relatively narrow line compared to other Ni core levels and 3) it does not suffer any interference from its spin-orbit component Ni $2p_{1/2}$ or from any other photoelectron or Auger line. Figure 9 plots the progression of the Ni $2p_{3/2}$ signal obtained for the Si on Ni sample at various intervals during silicide formation. In Figure 9a, the reaction front has not advanced far enough to be within the sampling depth of the spectroscopy and, correspondingly, no Ni 2p signal is observed. The first Ni 2p signal (Figure 9b), which must necessarily correspond to the interface, appears at a binding energy of 853.7 eV. As the sample heating continues, the Ni 2p signal increases in intensity (Figure 9c). After approximately a 25-fold increase in intensity, a shoulder appears on the low binding energy side at 853.0 eV (Figure 9d) and grows in intensity until it dominates the spectrum completely (Figure 9e). The $^4He^+$ backscattering spectra for this sample is shown in Figure 4. From these spectra it can be seen that the end phase corresponding to Figure 9e is Ni_2Si. Some unreacted Ni still remains at the SiO_2/Ni interface, but it is not within the observation depth of XPS. The thickness of the Si overlayer when the

Ni signal is first detected (Figure 9b) may be estimated using the known exponential dependence of photoemission intensity on overlayer thickness,[13]

$$\frac{I_{Ni}\ (\text{Si overlayer})}{I^{o}_{Ni}} = e^{-x/(\lambda^{Si}_{Ni}\ \sin\theta)} \qquad \text{III-3}$$

where I_{Ni} (Si overlayer) is the Ni 2p intensity with a Si overlayer of thickness x, I^{o}_{Ni} is the intensity of the Ni 2p when the Si overlayer has been consumed, λ^{Si}_{Ni} is the escape depth of Ni 2p electrons through a Si overlayer, and θ is the angle between the plane of the sample and the detector. Using this relationship, we have found that at the point where the interfacial signal of Figure 9b is observed, the thickness of the Si overlayer is $2.6\lambda^{Si}_{Ni}$. Assuming an escape depth of 25 Å, as has been determined for Si2p electrons from crystalline Si[14], the calculated Si overlayer thickness is ∿65 Å. This serves as a reasonable estimate because the escape depth in amorphous Si should be greater than that found for crystalline Si; however, the escape depth of Ni 2p electrons should be smaller than that found for Si 2p electrons due to the kinetic energy dependence of the electron escape depth.

The Si 2p spectra corresponding to the Ni 2p spectra in Figure 9 are shown in Figure 10. In Figure 10a, only the signal from the amorphous Si overlayer is detectable. As the Ni_2Si advances, the spectra in Figure 10b thorugh 10e are obtained. Unlike the emerging Ni 2p signal discussed above, one is unable to distinguish between the bulk Ni_2Si and the interfacial Si 2p signal. Furthermore, the Si^{o} overlayer and Ni_2Si appear to fall at the same binding energy. These

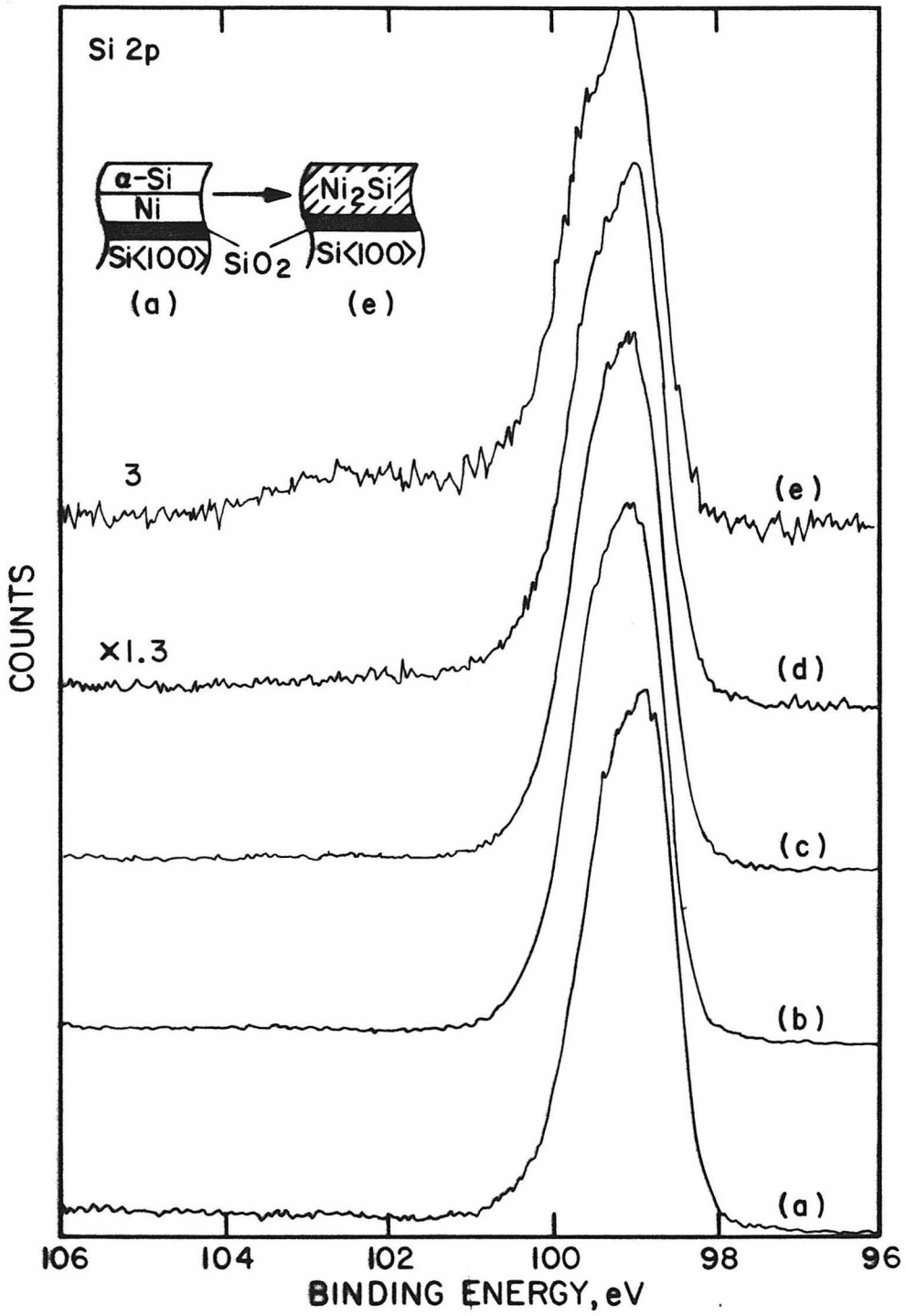

Figure 10: The Si 2p XPS spectra corresponding to the Ni core level spectra in figure 9.

problems arise for several reasons. First, unlike the Ni signals, the weak interfacial Si is lost because it overlaps with the intense signal from the amorphous Si overlayer. Second, when comparing binding energies from the Si semiconductor to those from the metallic Ni_2Si, final state relaxation effects, as well as referencing problems, may interfere. Relaxation shifts are a result of the passive electrons in the solid relaxing toward the positive hole created by the photoemission process[25], and are expected to be different for semiconductors and metals. The determination of the core level binding energies for semiconductors becomes an added problem because they are referenced to the Fermi level of the material which can vary with doping.

The first Ni 2p signal that emerges as the Ni_2Si reaction front advances into the observation depth of the spectroscopy is observed 0.7 eV higher in binding energy (Figure 9b) than the Ni 2p found for the end phase Ni_2Si (Figure 9e). This first Ni signal, which must necessarily correspond to the Si/Ni_2Si interface, demonstrates that the transition region is far from being chemically abrupt as various theoretical studies in the past have assumed. Instead, the interface consists of a transition layer of significant thickness and of a composition different from either the pure semiconductor or the bulk silicide.

By examining the chemical shift of the Ni 2p interface signal in detail, additional information concerning the local environment of the Ni atoms in this transition layer may be gained. We circumvent the ambiguities in the chemical shifts caused by final state relaxation and

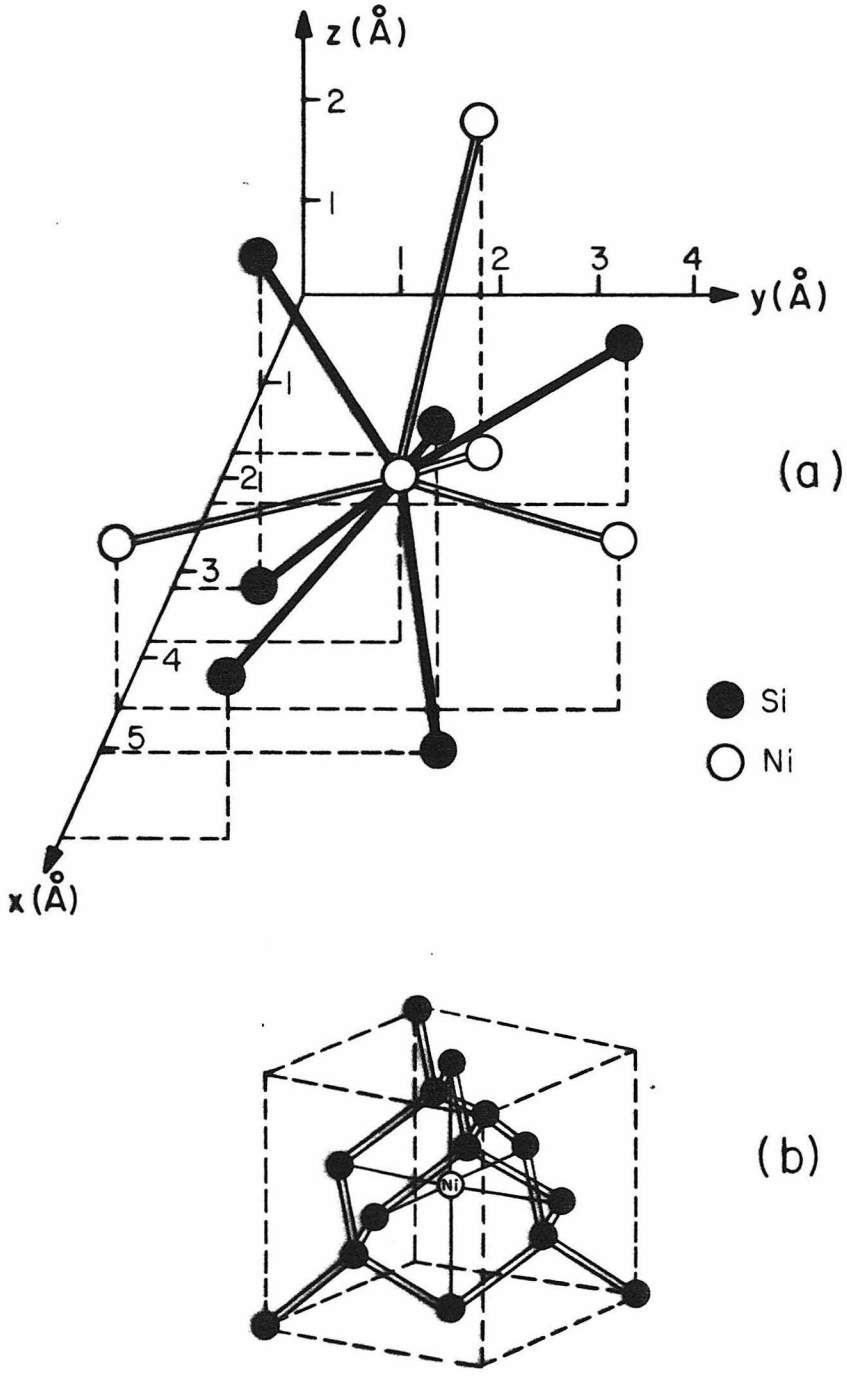

Figure 11: Coordination environments of the Ni atom in (a) NiSi and (b) in the interstitial voids of a single crystal Si lattice.

reference levels as mentioned previously by referring the interfacial Ni 2p binding energy to that found for the final phase Ni_2Si. The final state relaxation contribution to the chemical shifts is expected to be similar in both situations since bulk Ni_2Si is metallic and the interfacial region is expected to be metallic or semi-metallic. In the previous section, it was shown that the Ni 2p binding energies in the bulk silicides decrease in the order NiSi > Ni_2Si > Ni^o. These spectra indicated that charge is transferred from Ni to Si upon Ni-Si bond formation. The degree of charge transfer is determined by the number and strength of the heteropolar bonds formed within the structure. In Ni_2Si, the NiI environment consists of 4 Si and 8 Ni atoms, while the NiII is bonded to 5 Si and 8 Ni atoms. In the less nickel rich silicide NiSi, the coordination around the Ni consists of 6 Si and 4 Ni atoms. The decrease in the Ni-Si bonding and increase in the Ni-Ni bonding in Ni_2Si relative to NiSi is consistent with the relative ordering of the Ni2p binding energies. The Ni 2p signal from the interface falls 0.7 eV higher than that found for Ni_2Si, but only 0.2 eV higher than that for NiSi. This indicates that the local coordination environment of Ni atoms at the interface is considerably more rich in Si than that found for Ni in Ni_2Si, but only slightly richer than that found in NiSi.

Consider the limiting case for the Ni environment at the Si/Ni_2Si interface. This would consist of a single Ni atom in a pure Si lattice. There are essentially two possibilities for the Ni: it may exist in the Si lattice at either a substitutional or an interstitial site. The substitutional site is inconsistent with the observed chemical shift.

In a substitutional site, the Ni atom is bonded to only four Si atoms and one would expect the resulting Ni 2p core level to be much lower in binding energy. An interstitial site, on the other hand, is consistent with the observed binding energy. The tetrahedral bonding in Si results in the formation of Si "cages" with voids sufficiently large to allow the presence of a Ni atom. A Ni atom in such a void would see six Si atoms in a octahedral orientation and four Si atoms in a tetrahedral orientation. This is illustrated in Figure 11b. In Figure 11a, the coordination environment around Ni in NiSi is shown. It consists of six Si atoms in a distorted octahedron (bond lengths: 2.39 A, 2 at 2.44 A, 2 at 2.32 A, 2.28 A) and four Ni atoms in a slightly distorted tetrahedron (bond lengths: 2 at 2.70 A, 2 at 2.65 A). To approximate the bonding environment of a Ni atom in an interstitial site in pure Si, one need only replace the four tetrahedrally bonded Ni in NiSi with Si atoms. The distance from the central Ni atom to the tetrahedral sites is greater than the distance to the octahedral sites. In NiSi, the tetrahedral distances of 2.65 A and 2.70 A correspond to bond numbers of only 0.15 and 0.12, respectively. This means that the presence of Si atoms at these tetrahedral sites would increase the Ni → Si charge transfer, but only slightly. This would explain the Ni 2p binding energy for the interface region being only slightly greater than that found for NiSi. We suggest, therefore, that the initial interface signal in Figure 8b corresponds to Ni situated in the interstitial sites within the Si lattice. This gives the Ni a ligancy of 10, with six Si atoms placed octahedrally and four Si atoms placed tetrahedrally.

It should be noted that defining the local environment around the Ni atom at the interface in no way defines the stoichiometry of the compound that is present, if indeed a discreet compound exists. One would expect, in fact, a transition region graded in composition ranging from the limiting case of a single Ni atom in a Si cage to the Ni environment found in Ni_2Si. The increasing asymmetry on the low binding energy side of the Ni 2p peak in Figures 8b through 8d strongly supports this possibility.

To summarize, the Ni 2p spectra obtained as the Si/Ni_2Si interface advances toward the sample surface support the following conclusions:

1) There exists a transition region between Si and Ni_2Si of significant thickness and of a composition different from either pure Si or pure Ni_2Si. An estimation of the interfacial width will be presented in a later section.

2) The Ni atoms present in the interfacial region are in a local environment that is more rich in Si than that found for Ni in Ni_2Si.

3) The increasing asymmetry of the Ni2p lines as the signal emerges strongly suggests this transition region is not a unique silicide phase, but rather is graded in composition.

4) The initial Ni2p spectra (Figure 8b), which corresponds to the first detectable interface signal, is consistent with a single Ni atom located interstitially in a pure Si lattice.

The third point is consistent with work reported by N. Cheung, *et. al*, which concluded that Ni atoms deposited on a Si substrate are

located preferentially at the tetrahedral site in the Si lattice cage.[35] This was demonstrated with thin-crystal channeling experiments.

3. The Ni/Ni_2Si Interface with an Amorphous Si Substrate

The Ni/Ni_2Si interface may be studied by monitoring the photoemission signals from a sample of Ni deposited on amorphous Si during *in situ* silicide growth. In this situation, the emergent Si core level signals are examined as the Ni/Ni_2Si reaction front advances into the observation depth of the spectroscopy. The gross features of the core level progression can be seen in Figure 12. In Figure 12a , only photoemission signals from the Ni overlayer are observed. As the Ni/Ni_2Si front advances, core level signals from Si atoms may be detected (Figure 12b). As the reaction proceeds, the Si signals become more intense with a corresponding decrease in the Ni core level intensities until the Ni overlayer has been completely consumed (Figure 12d). The $^4He^+$ backscattered spectra corresponding to the spectra in Figure 12d is shown in Figure 13. It can be seen that the final phase is Ni_2Si. The second phase NiSi began to form after the consumption of the Ni overlayer, but it is not within the observation depth of the spectroscopy. The Si 2p core line was examined in detail to determine relative chemical shifts between the interface region and the bulk Ni_2Si. This line was chosen because it is the narrowest available line in spite of the overlap between the Si $2p_{1/2}$ and Si $2p_{3/2}$ spin-orbit components.

Figure 14 plots the progression of the Si 2p signals obtained for the Ni/Si sample as a function of time during silicide formation. In

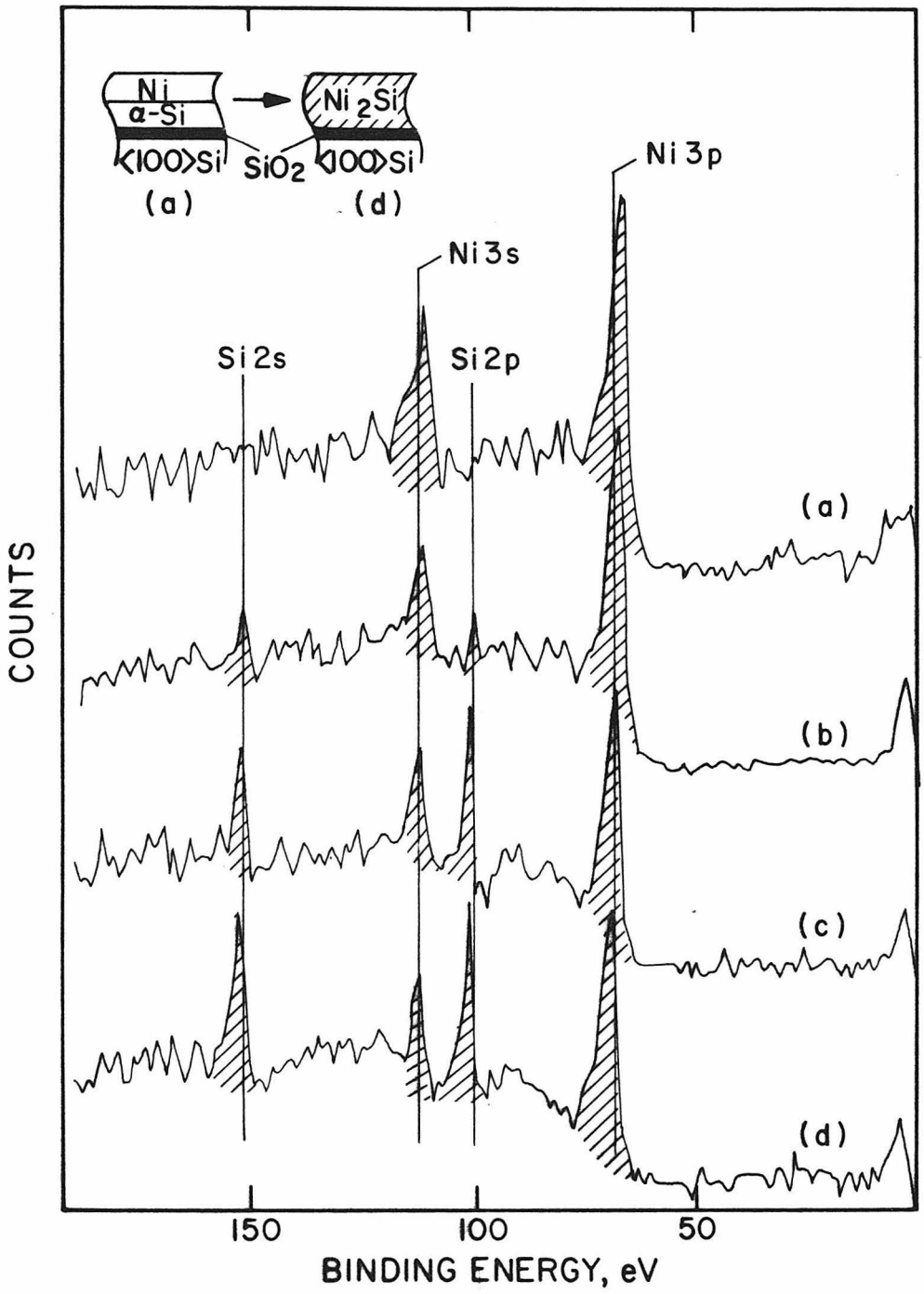

Figure 12: Wide scan XPS spectra showing the progression of the Si and Ni core lines as the Ni/Ni_2Si interface advances into the observation depth.

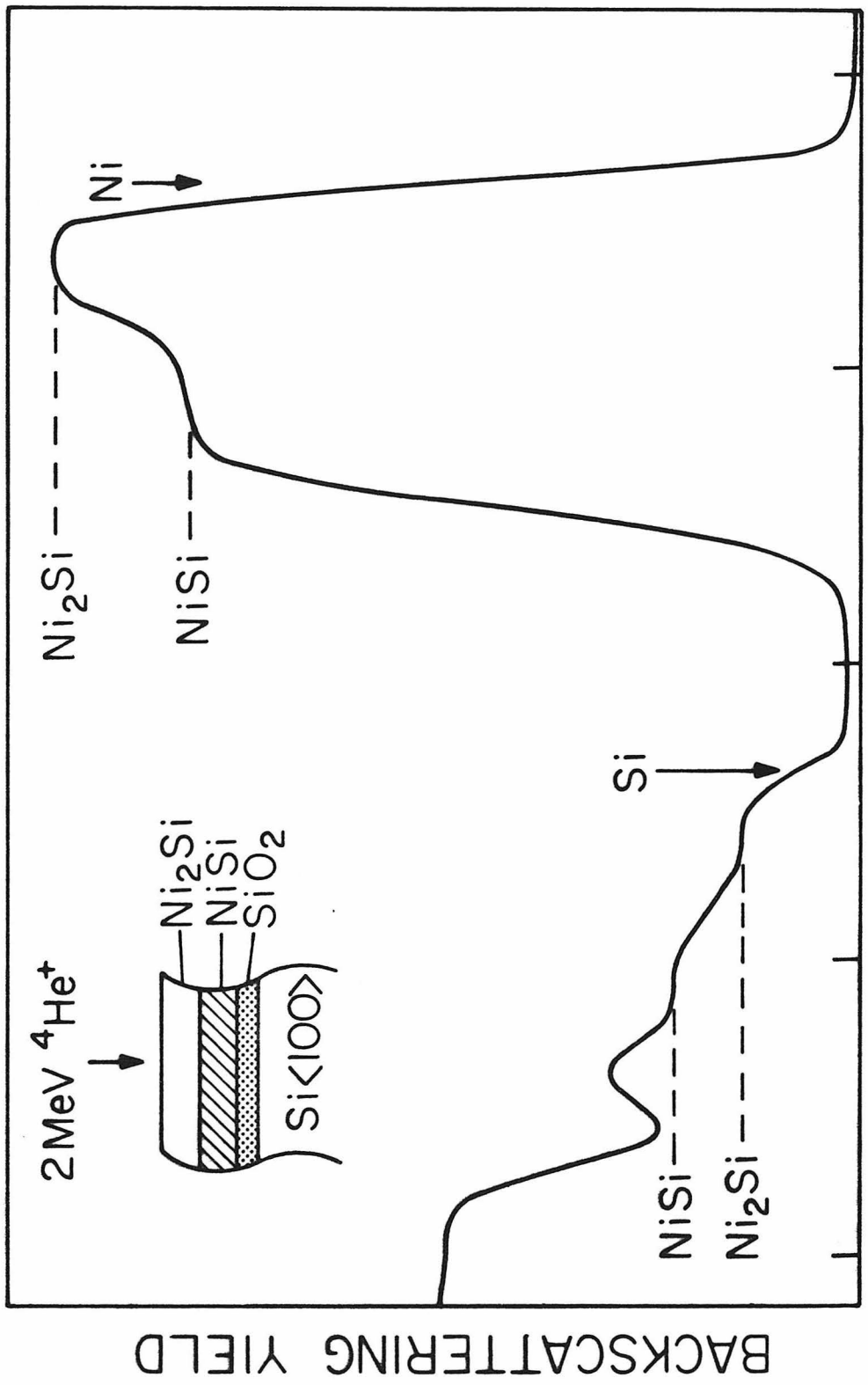

Figure 13. $^{4}He^{+}$ backscattered spectrum of the end phase of the dynamical growth experiment.

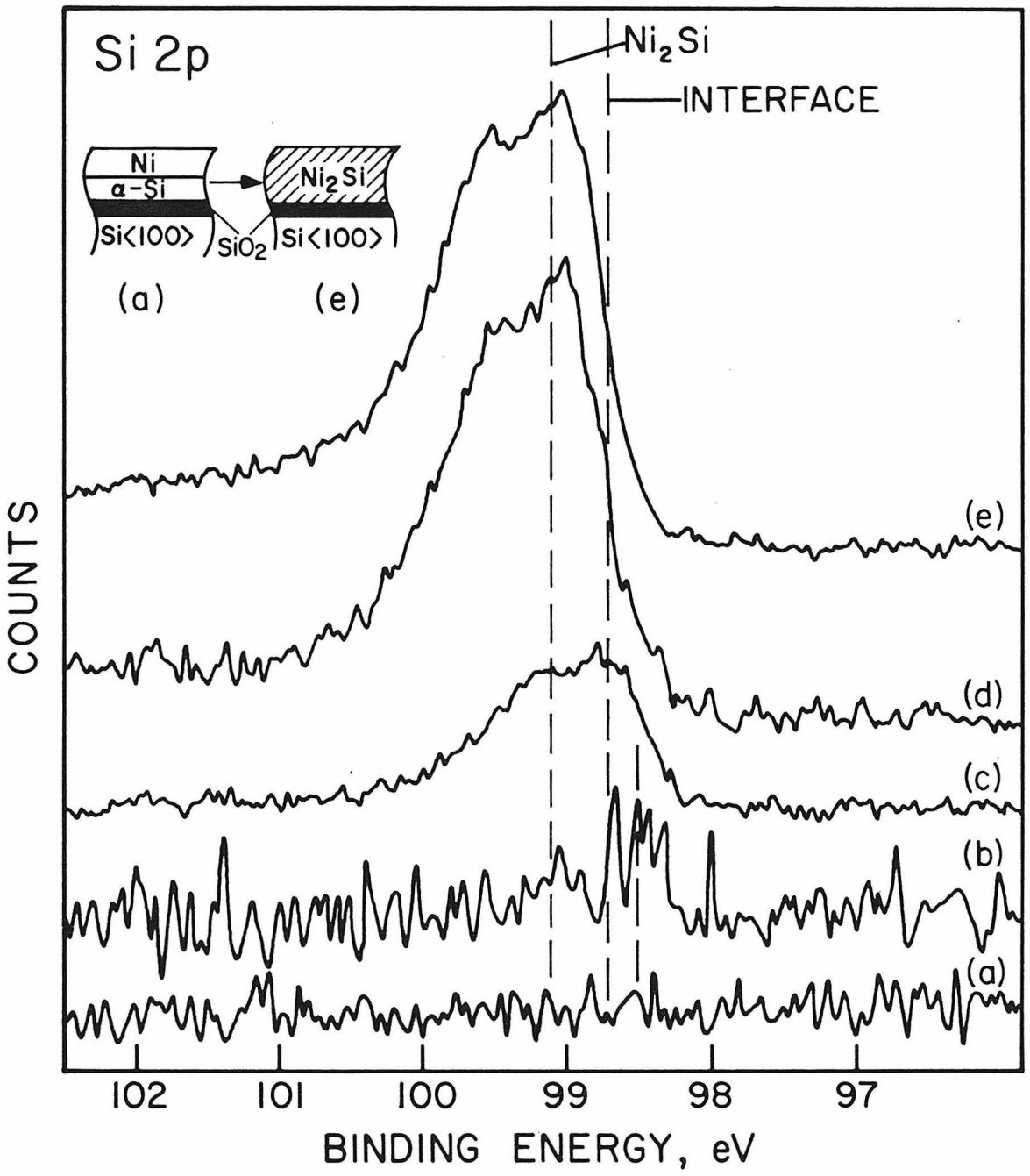

Figure 14: The Si 2p XPS spectra obtained as a function of time as the Ni/Ni_2Si interface approaches the sample surface.

Figure 14a the silicide reaction front has not yet advanced within the observation depth and thus no Si 2p intensity is detected. With continued heating, the Ni/Ni_2Si reaction front advances until the first weak Si 2p signal is observed at 98.5 eV (Figure 14b and at 98.7 eV a short time later Figure 14c). The Si 2p position in Figure 14b is only an estimation since the low signal to noise ratio makes an accurate determination of its binding energy difficult. In the final spectrum, Figure 14e, the thin film has reacted completely to form Ni_2Si as determined by $^4He^+$ backscattering. The Si 2p signal from this end phase falls at a binding energy of 99.1 eV. The thickness of the Ni overlayer when the first Si 2p signal is detected has been determined to be ~22 Å using the exponential dependence of the Si 2p signal on the overlayer thickness (equation III-3). An escape depth for Si 2p electrons through Ni of 15 Å was assumed.

The Ni $2p_{3/2}$ spectra corresponding to the Si spectra in Figure 14a, 14c-d are shown in Figure 15. As the silicide front advances, the Ni $2p_{3/2}$ binding energy shifts 0.5 eV upfield from its value of 852.5 eV in Ni metal (Figure 15a) to 853.0 eV in the bulk Ni_2Si (Figure 15d). The characteristic satellite structure accompanying the Ni 2p metal line (~858 eV) decreases in intensity and a second broader and less intense energy loss structure appears at ~861 eV. The interfacial Ni 2p peak is not observable because of overlap with the intense signal from the Ni overlayer. The gradual shift of the Ni 2p line from Ni metal to Ni_2Si is suggestive of an interface with a graded composition.

The first Si 2p that emerges as the Ni_2Si reaction front advances into the information depth of XPS is observed 0.4-0.6 eV lower in

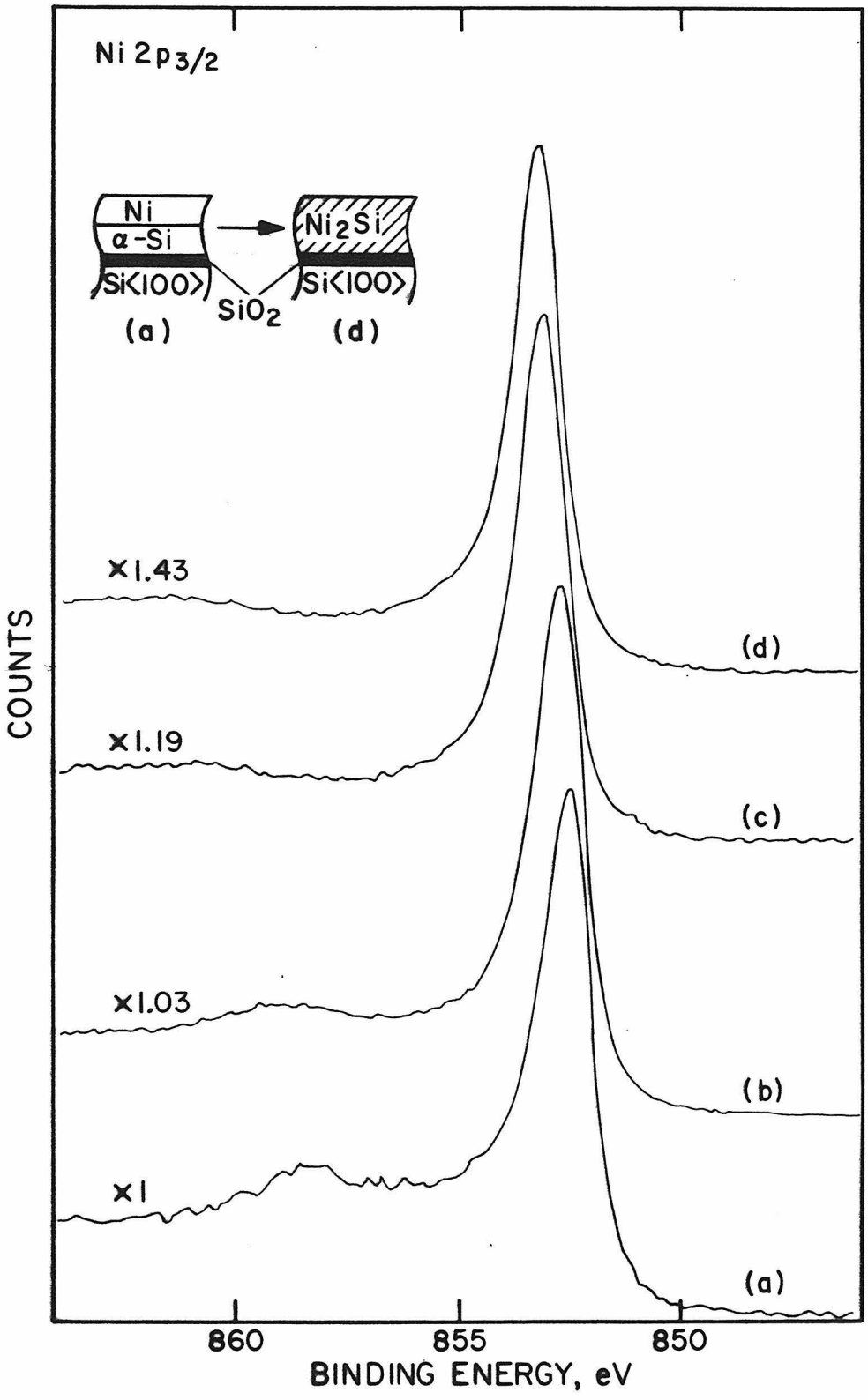

Figure 15: The Ni $2p_{3/2}$ spectra corresponding to the Si core lines in figure 14.

binding energy (Figure 14b,c) than the Si 2p found for Ni_2Si (Figure 14e). As in the case for the Si/Ni_2Si, this observation alone demonstrates that the Ni/Ni_2Si interface consists of a transitional layer of composition different from either the pure Ni^o or the bulk Ni_2Si. The 0.4-0.6 eV shift of the interfacial Si 2p relative to Ni_2Si is quite large when compared to the small shift of 0.1 eV between the Si 2p in NiSi and Ni_2Si. Recall that in NiSi, each Si atom is surrounded by six Ni atoms and one Si atom. In Ni_2Si, the Si environment consists of five NiII, four NiI, and two Si atoms (Figure 8a,b). In the metal rich silicide there are more Ni atoms in the Si coordination sphere than in NiSi but considerably more Ni-Ni interactions occur. The net result is that the Si 2p in Ni_2Si falls at a higher binding energy than the Si 2p in NiSi. This was demonstrated somewhat more quantitatively in a previous section using the empirical expressions of Pauling. In order for the Si 2p electrons from the interfacial region to experience such a large chemical shift downfield, a relatively large excess of negative charge must be present on the Si atom relative to the normal sp^3 hybridized Si in elemental Si. The Si atom in NiSi and Ni_2Si is already six and nine coordinate in Ni. The large excess charge on Si at the interface can only be explained if the Si is present in an even more Ni rich environment than that found in the bulk silicides. We suggest that the limiting case of Si substituted in the fcc lattice of Ni metal is consistent with the low binding energy observed for the initial Si 2p signal. In this situation, Si is 12 coordinated in Ni. This would permit a large overlap in the filled Ni 3d orbitals and the normally empty Si 3d orbitals, allowing for a large ($d \rightarrow d$) π interaction and,

hence, a large accumulation of excess charge on the Si relative to a normal sp^3 hybridized atom.

A Si atom substituted in the Ni lattice would be a metallic-like silicon. Pauling calculates that the metallic radius of a silicon atom with a ligancy of twelve is 1.375 Å. The corresponding radius for Ni with a coordination number of twelve is 1.244 Å. One can then predict that the Ni-Si bond length for Si substituted in the Ni lattice is 2.629 Å.

One may test the hypothesis that the first observed Si 2p signal in Figure 14 corresponds to a Si atom with a ligancy of twelve Ni atoms by examining the compound Ni_3Si. This compound has been shown to have the cubic crystal structure of $AuCu_3$.[36] In this structure, an Au atom is surrounded by twelve Cu atoms in a cubo-octahedron.[37] Each Cu atom has four Au and eight Cu atoms in the same arrangement. The Au-Cu bond length is 2.65 Å. If the spectra in Figure 12b,c correspond to a Si with ligancy twelve, then the Si 2p binding energy of Ni_3Si should fall 0.4-0.6 eV downfield of the Si 2p of Ni_2Si. Unfortunately, the preparation of Ni_3Si is not straightforward and examination of its core levels by XPS must await future experiments.

As mentioned in the discussion on the Si/Ni_2Si interface, knowledge of the local environment around the Si atom in the Ni/Ni_2Si interface does not define the stoichiometry of the compound present. The data indicate that in fact, the transition region is composed not of a unique composition, but rather of a graded one. Evidence for this is derived from 1) the gradual shift of the Ni 2p signals in

Figure 15 and 2) the shift of the Si 2p from 98.5 eV (Figure 14b) to 98.7 eV Figure 14c) as the interface advanced.

In summary, the following conclusions concerning the Ni/Ni_2Si interface are supported by the Si 2p and Ni 2p core level spectra obtained during *in situ* silicide growth.

1) A transitional layer is present between Ni and Ni_2Si with a composition different from either pure Ni or the bulk Ni_2Si silicide. Estimations of the width of this layer will be presented in a later section.

2) The Si atoms in this transition region must be in a substantially more Ni rich environment than that found for Si in Ni_2Si.

3) The transition region cannot be described as a unique silicide phase, but rather as a layer of graded composition.

4) The first detectable Si 2p signal in Figure 12 is consistent with a metallic-like Si with a high ligancy. We suggest this is due to a Si atom substituted in the fcc lattice of Ni.

4. The Ni/Ni_2Si Interface with a Crystalline Si Substrate

The Ni/Ni_2Si interface was also examined using a <100> Si substrate instead of the amorphus Si material discussed above. Again, the emergent Si 2p signal was monitored with time as the Ni/Ni_2Si reaction front advanced during the *in situ* heat treatment. The progression of the Si 2p position and intensity is plotted in Figure 16.

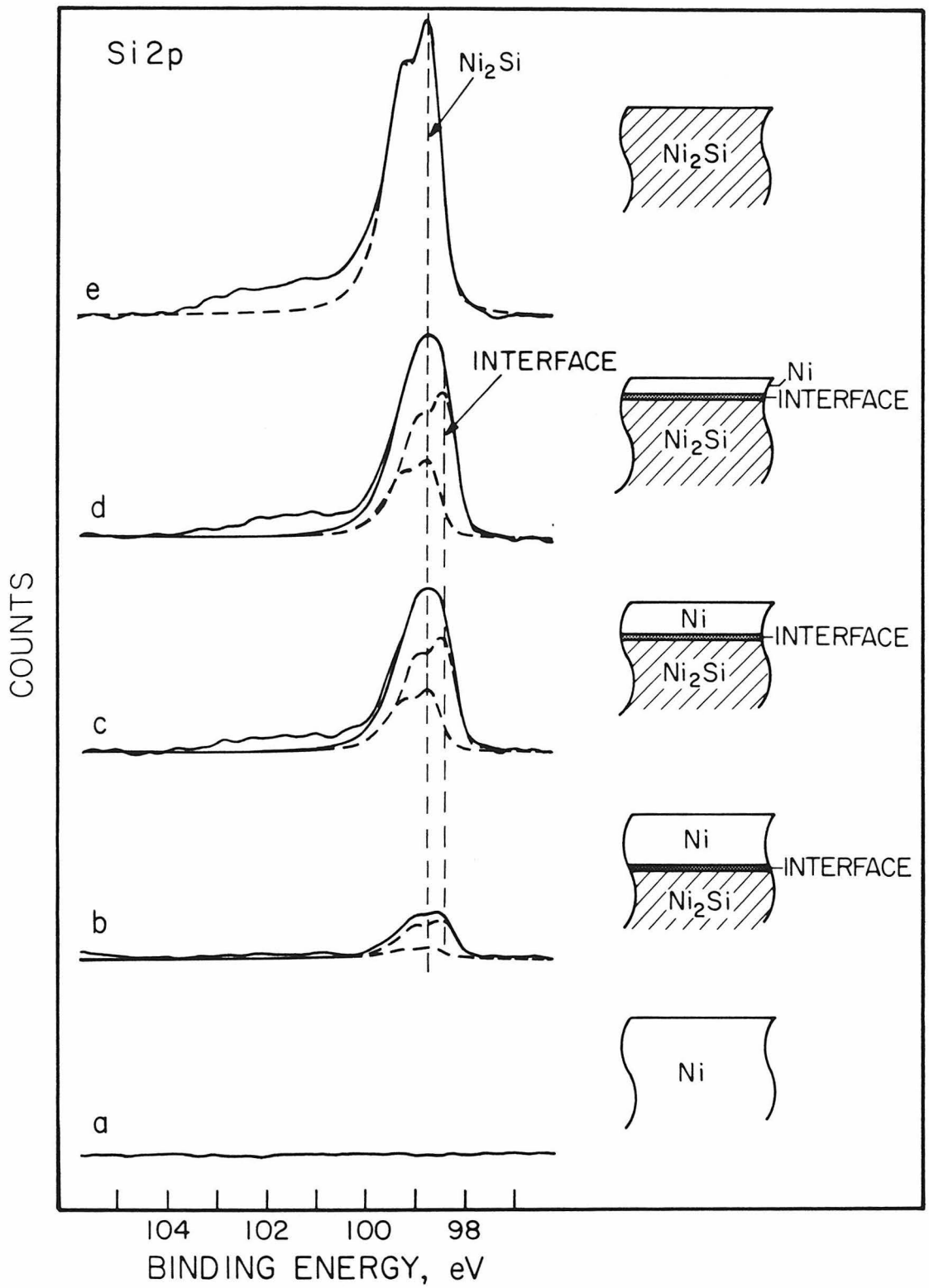

Figure 16: The Si 2p spectra obtained as the Ni/Ni_2Si interface advanced toward the sample surface. The dashed spectra in (b) - (d) represent peak components determined using least square criterion. The dashed spectrum in (e) is of a clean Si substrate (shifted in energy for comparison).

In Figure 16a no Si 2p intensity is detected since the reaction front has not progressed into the observation depth. As the Ni/Ni_2Si front proceeds toward the surface, the spectra shown in Figure 16b through 16d are obtained. In the final spectrum, Figure 16e, the reaction has completely consumed the Ni film yielding an end product of Ni_2Si. Notice in Figure 16e that the 0.6 eV spin-orbit splitting of the Si 2p line is clearly resolvable. A spectrum of clean Si (the dotted spectrum) has been plotted over the spectrum of the bulk Ni_2Si to delineate the silicide signal from the broad low intensity signal appearing on the high binding energy side. Previous studies have shown this intensity to be due to silicon suboxides that are formed as the silicide reaction front sweeps out the impurity oxygen present in the evaporated Ni films.[24] This will be discussed in more detail in Chapter V. In figures 16b through 16d, the characteristic Si 2p spin-orbit splitting is no longer resolvable. This suggests that the peak envelope consists of at least two closely spaced signals. To test this hypothesis, two signals corresponding to a bulk and an interfacial signal were fitted to the data using a least squares minimization criterion. The clean Si 2p signal shown in Figure 16e was used as the lineshape model for the bulk and interfacial signals. The position found for bulk Ni_2Si in Figure 16e was held constant while the height of this signal and the position and height of the interface signal was allowed to vary in each of the spectra in Figures 16b and 16d. This procedure corresponds to a three parameter analysis of the observed line shapes. In this figure, the fitted spectra and their sum are plotted over the raw data. Three features of the fitted spectra suggest that they are a reasonable estimation

of the composite peaks within the raw data envelope. First, the position of the interface signal was found to remain constant for spectra 16b through 16d. Secondly, the ratio of the intensity of the interface signal to the intensity of the bulk Ni_2Si signal was found to be the same in Figure 16c as in Figure 16d. As will be discussed in the following section, theory predicts that this ratio should be constant. In Figure 16b, the ratio is somewhat larger than that found for Figures 16c and 16d, but this may be attributed to the interfacial region not yet being entirely within the observation depth of the spectroscopy at this early stage. Thirdly, the 0.4 eV shift of the Si 2p interface signal relative to the bulk Ni_2Si signal is completely consistent with the shift (0.4-0.6 eV) found for the interface signal using an amorphous substrate (Figure 14).

The similarity of the chemical shifts for the Si 2p interface signal between that obtained with an amorphous substrate and that found using a crystalline substrate indicates that the Si environments in these two situations are the same. The details of this chemical environment were discussed in the previous section. The essential difference between the Ni/Ni_2Si interfaces grown on crystalline and amorphous Si substrates is the width of the transitional phase. This is discussed in more detail in the following section where it is shown that the interfacial width using a crystalline substrate is 2-3 times narrower than that found using an amorphous substrate.

5. Interfacial Widths

The widths of the Ni/Ni_2Si and Si/Ni_2Si transition regions can be estimated from the ratios of the bulk Ni_2Si and interface photoelectron intensities. The photoemission intensity at a given energy in a homogeneous material is

$$dI = F\alpha Dke^{-x/\lambda}dx \qquad \text{III-4}$$

where F is the x-ray flux, α is the photoionization cross-section in a given shell of a given atom for a given x-ray energy, D is the atom density of the given element, k is a spectrometer factor which includes detection efficiency and geometrical factors, x is the distance through the material the electron must travel, and λ is the electron escape depth.

Consider the case of the Ni/Ni_2Si interface shown in Figure 17. Using equation III-4, the Si 2p intensity from the interface I_{Si}^{int}, and from the bulk Ni_2Si, I_{Si}^{bulk}, may be easily calculated.

$$I_{Si}^{bulk} = F\alpha k D_{Si}^{bulk} \lambda_{Si}^{bulk} e^{-\Delta x/(\lambda_{Si}^{int}\sin\theta)} e^{-\Delta x'/(\lambda_{Si}^{Ni}\sin\theta)} \qquad \text{III-5}$$

$$I_{Si}^{int} = F\alpha D_{Si}^{int} \lambda_{Si}^{int} \left(1-e^{-\Delta x/(\lambda_{Si}^{int}\sin\theta)}\right) e^{-\Delta x'/(\lambda_{Si}^{Ni}\sin\theta)} \qquad \text{III-6}$$

where D_{Si}^{int} and D_{Si}^{bulk} are the atomic densities of Si in the interfacial region and in the bulk Ni_2Si, respectively; λ_{Si}^{int} and λ_{Si}^{bulk} are the

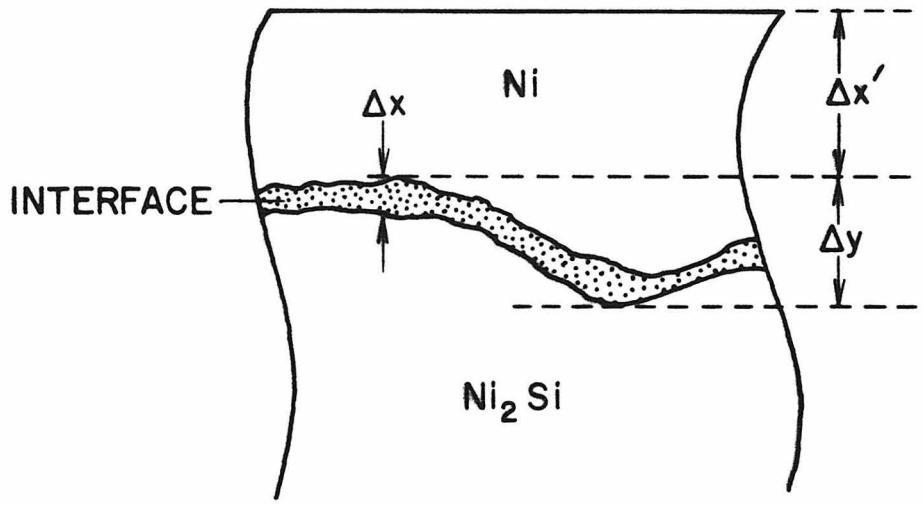

Figure 17: Schematic of the Ni/Ni_2Si interface.

electron escape depths of the Si 2p electrons in the interfacial region and bulk Ni_2Si, respectively; and θ is the angle between the detector and sample plane (38.5^{o}). The ratio of the Si 2p intensity from the interfacial region to the intensity from the Ni_2Si is determined by the interfacial width Δx and is independent of the thickness of the Ni overlayer. That is

$$\frac{I_{Si}^{int}}{I_{Si}^{bulk}} = \frac{D_{Si}^{int}\,\lambda_{Si}^{int}}{D_{Si}^{bulk}\,\lambda_{Si}^{bulk}} \left(e^{\Delta x/(\lambda_{Si}^{int}\sin\theta)} + 1\right) \qquad \text{III-7}$$

The value of Δx is a measure of the average interface width. Large scale undulations of the interface, Δy, as shown in Figure 17 do not affect the estimations for Δx since $I_{Si}^{int}/I_{Si}^{bulk}$ is independent of the thickness of the Ni overlayer. An analogous equation can be written for the case of a Si overlayer using the Ni 2p interface and bulk Ni_2Si signal intensities.

There are two limiting cases to be considered. If the interfacial region is sufficiently wide, then I^{int}/I^{bulk} will be much greater than unity and initially, only the interface signals should be seen as the silicide reaction front advances. As the interface reaches the sample surface and then dissipates, the bulk Ni_2Si signal should begin to dominate the spectra. This wide interfacial region characterizes the situation in Figures 9 and 14 where deposited Si and Ni films were used. Equation III-7 may be rewritten as

$$\Delta x = \lambda_{Si}^{int} \sin\theta \ \ell n \left[\frac{I_{Si}^{int}/I_{Si}^{bulk}}{R} + 1 \right] \qquad \text{III-8}$$

where $R = \dfrac{D_{Si}^{int} \lambda_{Si}^{int}}{D_{Si}^{bulk} \lambda_{Si}^{bulk}}$

$D_{Si}^{int} < D_{Si}^{bulk}$ and $\lambda_{Si}^{int} \sim \lambda_{Si}^{bulk}$ since the interface consists of a Ni-rich silicide. We estimate that the interface signal will appear to dominate when the bulk Ni_2Si intensity is only 0.1 of the interface intensity. This corresponds to $\Delta x > 1.5\ \lambda_{Si}^{int}$. This places a lower limit on the Ni/Ni_2Si interface width of 22 Å if a "metallic like" escape depth of 15 Å[38] is assumed.

Analogously, a lower limit of $1.5\ \lambda_{Ni}^{int}$ may be placed on the Si/Ni_2Si interface width. This again corresponds to a transitional width of at least 22 Å if λ is 15 Å.

The Ni/Ni_2Si interface grown on a crystalline Si substrate is the second limiting case to be considered. Here, the $I_{Si}^{int}/I_{Si}^{bulk}$ ratio is such that the Si 2p signals corresponding to both the interfacial and bulk Ni_2Si are detected simultaneously. From Figures 14c and 14d, the ratio of interface to bulk signal is found to be 1.67. Since the Ni/Ni_2Si interface consists of a Ni-rich silicide, again $D_{Si}^{int} \approx D_{Si}^{bulk}$ and $\lambda_{Si}^{int} \sim \lambda_{Si}^{bulk}$. This corresponds to $\Delta x > 0.6\ \lambda_{Si}^{int}$. Assuming a 15 Å escape depth, this corresponds to a lower limit of 9 Å for the interface width. If the density of Si atoms at the interface was only one-half that found in bulk Ni_2Si, this would give an upper bound for the estimation of Δx of 14 Å. Although the absolute values of these

interfacial widths depend on the accuracy of the assumed escape depth, a relative comparison of the widths should be quite reliable. The essential difference between the Ni/Ni_2Si interface using a crystalline substrate as compared to an amorphous substrate is that the former is 2 - 3 times narrower ($0.6\ \lambda_{Si}^{int}$) than the latter ($1.5\ \lambda_{Si}^{int}$).

D. SUMMARY

In this chapter a new approach for studying silicide/semiconductor and silicide/metal interfaces has been developed. The approach utilizes the exponential attenuation of photoemission intensities to examine the advancing planar interfacial region. This is done by dynamically monitoring the *in situ* formation of the silicide. The technique has two major advantages over the traditional approaches used to examine interfacial regions. First, it allows the examination of a realistic interface; that is, an interface which is bounded on either side by an extended solid. Secondly, this dynamic approach allows investigation of the interface without the chemical and structural perturbations caused by conventional ion and chemical profiling.

The chemical nature of three interfaces in the Ni-Si system were investigated: The Si/Ni_2Si interface and the Ni/Ni_2Si interface using both an amorphous and crystalline Si substrate. $^4He^+$ back-scattering was used to follow the progression of the thin film reaction and to provide quantitative information on atomic composition.

The bonding in the bulk silicides Ni_2Si and NiSi was first examined using the empirical relationships of Pauling. It was shown that the observed Ni and Si core level shifts, as well as the known structures for these compounds, are consistent with the presence of significant (Ni 3d→Si 3d) π interactions.

The interfacial experiments demonstrated that at the Si/Ni_2Si transition region, the local environment of the Ni atoms is more Si-rich than that found for Ni in Ni_2Si. This transition layer is not a unique silicide phase, but rather is graded in composition. The first detectable Ni $2p_{3/2}$ signal is consistent with a single Ni atom located in the octahedral/tetrahedral voids in a pure Si lattice. This supports channeling studies reported by N. Cheung, *et al.*, which concluded that Ni atoms deposited on crystalline Si are located preferentially at the tetrahedral site in the Si lattice. K. N. Tu has proposed an interstitial mechanism to explain the low-temperature formation of the near-noble metal silicides. This mechanism postulates that the metal atom diffuses into an interstitial site in the Si lattice and thereby assists in bond breaking. The XPS data presented here support this model. The width of the Si/Ni_2Si interface was determined to be at least $1.5\lambda_{NI}^{int}$, where λ_{Ni}^{int} is the escape depth for Ni 2p electrons in the interfacial layer. A lower limit of 22 Å may be placed on the width of transition layer assuming λ_{Ni}^{int} is 15 Å.

The Ni/Ni_2Si interface was studied using both amorphous and crystalline Si as a substrate. In both cases it was found that the Si atoms in the transition region were in a substantially more Ni rich environment than that found for Si in Ni_2Si. The transition layer is

again of graded composition. The first detectable Si 2p signal is consistent with a metallic-like Si with a high ligancy. We propose this signal is due to Si substituted in the fcc lattice of Ni metal. In this environment, Si is bonded to twelve Ni atoms. The essential difference between the Ni/Ni_2Si interface using a crystalline substrate as compared to an amorphous substrate is that the former is 2-3 times narrower (0.6 λ_{Si}^{int}) than the latter (1.5 λ_{Si}^{int}). Assuming λ_{Si}^{int} is 15 Å, the lower limit on the interfacial width using an amorphous substrate is 22 Å, while a crystalline substrate yields an interface at least 9 Å wide.

Table 1: Bond Distances and Bond Numbers for Ni_2Si

Central Atom	Bonded Atom	Observed Distance (Å) and Multiplicity	Bond Number
Si	Ni II	2.58 (2)	0.41
	Ni II	2.34 (2)	1.04
	Ni II	2.39 (1)	0.86
	Ni I	2.30 (2)	1.04
	Ni I	2.32 (1)	0.97
	Ni I	2.29 (1)	1.08
	Si	3.15 (2)	0.05
			Σ = 7.99
Ni I	Si	2.30 (2)	1.04
	Si	2.32 (1)	0.97
	Si	2.29 (1)	1.08
	Ni I	2.70 (2)	0.17
	Ni II	2.54 (2)	0.36
	Ni II	2.62 (1)	0.26
	Ni II	2.72 (2)	0.18
	Ni II	2.71 (1)	0.19
			Σ = 6.00
Ni II	Si	2.58 (2)	0.41
	Si	2.34 (2)	1.04
	Si	2.39 (1)	0.86
	Ni I	2.54 (2)	0.36
	Ni I	2.62 (1)	0.26
	Ni I	2.72 (2)	0.18
	Ni I	2.71 (1)	0.19
	Ni II	2.58 (1)	0.36
	Ni II	2.59 (1)	0.34
			Σ = 5.99

Table 2: Bond Distances and Bond Numbers for NiSi

Central Atom	Bonded Atom	Observed Distance (Å) and Multiplicity	Bond Number
Si	Ni	2.44 (2)	0.54
	Ni	2.32 (2)	0.86
	Ni	2.28 (1)	1.00
	Ni	2.38 (1)	0.68
	Si	2.58 (1)	0.53
			Σ = 5.01
Ni	Si	2.44 (2)	0.54
	Si	2.32 (2)	0.86
	Si	2.28 (1)	1.00
	Si	2.38 (1)	0.68
	Ni	2.65 (2)	0.15
	Ni	2.70 (2)	0.12
			Σ = 5.02

References

1) P. S. Ho, T. Y. Tan, J. E. Lewis, G. W. Rubloff, J. Vac. Sci. Technol., 16 (5), 1120, (1979)

2) D. J. Fertig, G. Y. Robinson, Solid State Electron, 19, 407 (1976)

3) J. A. Roth, C. R. Crowell, J. Vac. Sci. Technol., 15, 1317 (1978)

4) J. L. Freeouf, G. W. Rubloff, P. S. Ho, T. S. Kuan, Phys. Rev. Lett., 43, 1836 (1979)

5) J. A. Roth, Thesis, University of Southern California, Materials Science Department

6) K. N. Tu, W. K. Chu, J. W. Mayer, Thin Solid Films, 25, 403 (1975)

7) R. W. Bene, R. M. Walser, Proceedings of the Symposium on Thin Film Phenomenon - Interfaces and Interactions, eds. J. E. Baglin and J. M. Poate (Electrochemical Society, Princeton, N. J., 1978) p 21

8) C. S. Fadley, R. J. Baird, W. Seikhaus, T. Novakov, S. A. L. Bergstrom, J. of Electron Spectrose., 4, 93 (1974)

9) D. M. Scott, P. J. Grunthaner, B. Y. Tsaur, Paper presented at the 156th Meeting of the Electrochemical Society, Los Angeles, 1979 (to be published in the Proceedings of the Symposium on Thin Film Interfaces and Interactions, 1980)

10) J. C. Fuggle, D. J. Fabian, L. M. Watson, J. Electron Spect. and Related Phenom. 9, 99 (1976)

11) C. Kittel, Introduction to Solid State Physics, Fourth Edition (Wiley, New York, 1971) ch. 7 and 8

12) G. K. Wertheim, S. Hufner, J. Inorg. Nucl. Chem., 38, 1701 (1976)

13) T. A. Carlson, G. E. McGuire, J. of Electron Spectrosc., 1, 161 (1972/73)

14) J. M. Hill, D. G. Royce, C. S. Fadley, L. F. Wagner, F. G. Grunthaner, Chem. Phys. Lett., 44, 225 (1976)

15) R. L. Martin, D. A. Shirley in Electron Spectroscopy: Theory, Techniques, and Applications, C. R. Brundle and A. D. Baker, eds. (Academic Press, New York, N. Y.) 1977

16) A. L. Allred, E. G. Rochow, J. Inorg. Nucl. Chem., 5, 264, (1958)

17) A. P. Hagen, A. G. MacDiarmid, Inorg, Chem., b, 686, 1941 (1967)

18) O. Kahn, M. Bigorgne, J. Organometal. Chem., 10, 137 (1967)

19) A. D. Berry, E. R. Corey, A. P. Hagen, A. G. MacDiarmid, F. E. Saalfeld, B. B. Wayland, J. Amer. Chem. Soc., 92, 1940 (1970)

20) N. A. D. Carey, H. C. Clark, Inorg. Chem., 7, 94 (1968)

21) W. A. G. Graham, Inorg. Chem., 7 771 (1968)

22) W. Jetz, P. B. Simons, J. A. J. Thompson, W. A. G. Graham, Inorg. Chem., 5, 2217 (1966)

23) D. J. Patmore, W. A. G. Graham, Inorg. Chem., 6, 981 (1967)

24) R. Ugo, S. Cenini, F. Bonati, Inorganica Chem. Acta. 1:3, 451 (1967)

25) T. L. Brown, P. A. Edwards, C. B. Harris, J. L. Kirsch, Inorg. Chem., 8, 763 (1969)

26) K. W. Muir, J. A. Ibers, Inorg. Chem., 9, 440 (1970)

27) Ljubica Manojlovic-Muir, K. W. Muir, J. A. Ibers, Inorg. Chem. 9 447 (1970)

28) L. Pauling, The Nature of the Chemical Bond, 3rd Edition, (Cornell University Press, Ithaca, N.Y., 1960)

29) K. Toman, Acta. Cryst., 4, 462 (1951)

30) A. J. C. Wilson, ed., Structure Reports, 15, 107

31) J. M. Andrens, F. B. Koch, Solid State Electron., 14, 901 (1971)

32) K. Toman, Acta. Cryst., 5, 329 (1952)

33) W. B. Pearson, ed., Structure Reports, 19, 180

34) A. J. C. Wilson, ed., Structure Reports, 16, 123

35) N. Cheung, J. W. Mayer, Submitted to Phys. Rev. Lett.

36) A. J. C. Wilson, ed., Structure Reports, 15, 108

37) W. B. Pearson, The Crystal Chemistry and Physics of Metals and Alloys, (John Wiley and Sons, New York, 1972)

38) D. R. Penn, J. Elect. Spectrosc and Related Phenom., 9, 29 (1976)

39) K. N. Tu, Appl. Phys. Lett., 27, 221 (1975)

CHAPTER IV

UHV DEPOSITIONS OF THIN Ni FILMS ON Si <100>

A. INTRODUCTION

In the previous chapter, it was shown that the Ni/silicide and Si/silicide interface could be studied by dynamically monitoring the advancing silicide reaction front during *in situ* growth. This allowed examination of the interfacial region in its "native habitat"; that is, with an extended solid on both sides. In this chapter, a complementary approach is presented which allows examination of the as-deposited interface between nickel and silicon. These experiments follow the development of the chemical properties of the interface as sequential monolayers of metal are evaporated *in situ* on a silicon substrate. This approach has been used in several recent studies to investigate the properties of the Pd/Si[1-3] and Pt/Si[3] interfaces during the initial stages of silicide formation. The technique has an advantage over the conventional ion milling approach since it avoids the chemical and structural perturbations induced by the sputtering process. Its only disadvantage is that is is an approximation of the true interface, which is a point that is often overlooked. The true interface is bounded on both sides by an extended solid. The presence of this solid will impose different bonding restrictions on the interfacial atoms than will the presence of a vacuum. In particular, the stoichiometry and local bonding geometries of the compounds formed within this transition region could be strongly influenced by the nature of the extended overlayer and the strain

induced by its presence. To defend the monolayer deposition technique, two basic facts must be established. First, it must be shown that the interface signal obtained when only a few atomic layers of metal are present on the silicon substrate still persists (appropriately attenuated) when many atomic layers of the metal are present. One may then conclude that such a signal is indeed a good representation of the true interface and is not solely a result of surface reconstruction or some other phenomenon caused by the termination of the solid by a vacuum. Second, it must be demonstrated that the chemical shift observed for the metal at monolayer and sub-monolayer coverages is not due to aggregation effects. Even in the complete absence of any chemical interaction between the Ni and the Si substrate, atomically dispersed Ni is not expected to display the same characteristics as bulk Ni metal.[4-5] Neither of the above two points have been addressed in the published literature. Unless they are taken into consideration, any attempt to define the stoichiometry and bonding within the true interface is questionable.

This chapter is divided into two sections. The first section is concerned with the room temperature deposition of Ni metal on Si <100>. The development of the interface is monitored by examination of the photoemission signals from the Si and Ni core levels as sequential atomic layers of Ni are deposited. In the second part, the effect of substrate temperature on these core level signals is investigated.

B. EXPERIMENTAL

The results reported here were all obtained on n-type <100> Si substrates with a resistivity of 1 to 10 Ω-cm. Prior to loading into the XPS analyzer, the Si surface was cleaned under a N_2 atmosphere by spinning a 3/8 inch by 3/8 inch Si sample at 3600 rpm and adding dropwise 200 µl of 1:10 HF in ethanol, followed by 500 µl of absolute ethanol. The sample inlet port of the spectrometer is connected to the N_2 drybox so that no further exposure of the sample to ambient contamination occurred after etching. This procedure was found to produce an essentially contaminant free Si surface. No Si oxide was detectable and only a small amount of residual carbon and oxygen (<< monolayer) attributable to absorbed water and solvent were observable.

The Ni evaporations were performed *in situ* in the XPS spectrometer at a pressure of 2-5 x 10^{9} Torr. The base pressure was 5 x 10^{-10} Torr. The Ni was evaporated from a resistively heated wire mounted ∿2½ cm away from the sample. A shutter was used to shield the sample from the source to minimize sample heating.

Where *in situ* reactions were performed, the samples were heated to 548°K. The pressure during the heating was better than 2 x 10^{-9} Torr. The samples were cooled to 298°K for data accumulation.

The XPS spectra were obtained using a modified HP 5950A spectrometer, which is described in more detail in Chapter II. After XPS measurements, samples were removed for examination and calibration of the atomic composition by $^{4}He^{+}$ backscattering.[13]

C. RESULTS AND DISCUSSION

1. Room Temperature Depositions of Ni on Si <100>

The as-deposited Ni/Si interface was investigated by monitoring the Ni 2p and Si 2p photoelectron signals as thin Ni films were evaporated *in situ* onto a clean Si <100> substrate. These core lines were chosen because of their high photoelectron cross-section relative to the other available core lines and because they suffer no overlap with other photoelectron or Auger peaks. Figure 1 shows the broad energy spectra of 1280 eV obtained after twenty sequential depositions of Ni onto Si. The thickness of the deposited Ni ranged from 8.0×10^{13} Ni/cm^2 to 1.9×10^{16} Ni/cm^2, as determined with $^4He^+$ backscattering using an independently calibrated standard. The first spectrum in the foreground is that of the clean Si substrate. The Si 2p and Si 2s lines at ∿100 eV and ∿150 eV, respectively, are the only observable photoelectron signals. There is no detectable carbon or oxygen present on the surface. As sub-monolayer coverages of Ni are deposited, the Ni 2p core line at ∿850 eV becomes observable. As sequentially more Ni is added, the Ni 2p and the Ni Auger manifold (500-800 eV) begin to dominate the spectra. During the course of the evaporations carbon 1s and oxygen 1s signals are detectable. These are impurities accumulating during the evaporations and are probably source related. The carbon contamination level stays relatively constant throughout the sequence, while oxygen is observed only in the last 5-6 depositions. The stepped appearance in the spectral background is due to electrons that have suffered extrinsic energy losses.[6] These electrons were initially excited to the energy of

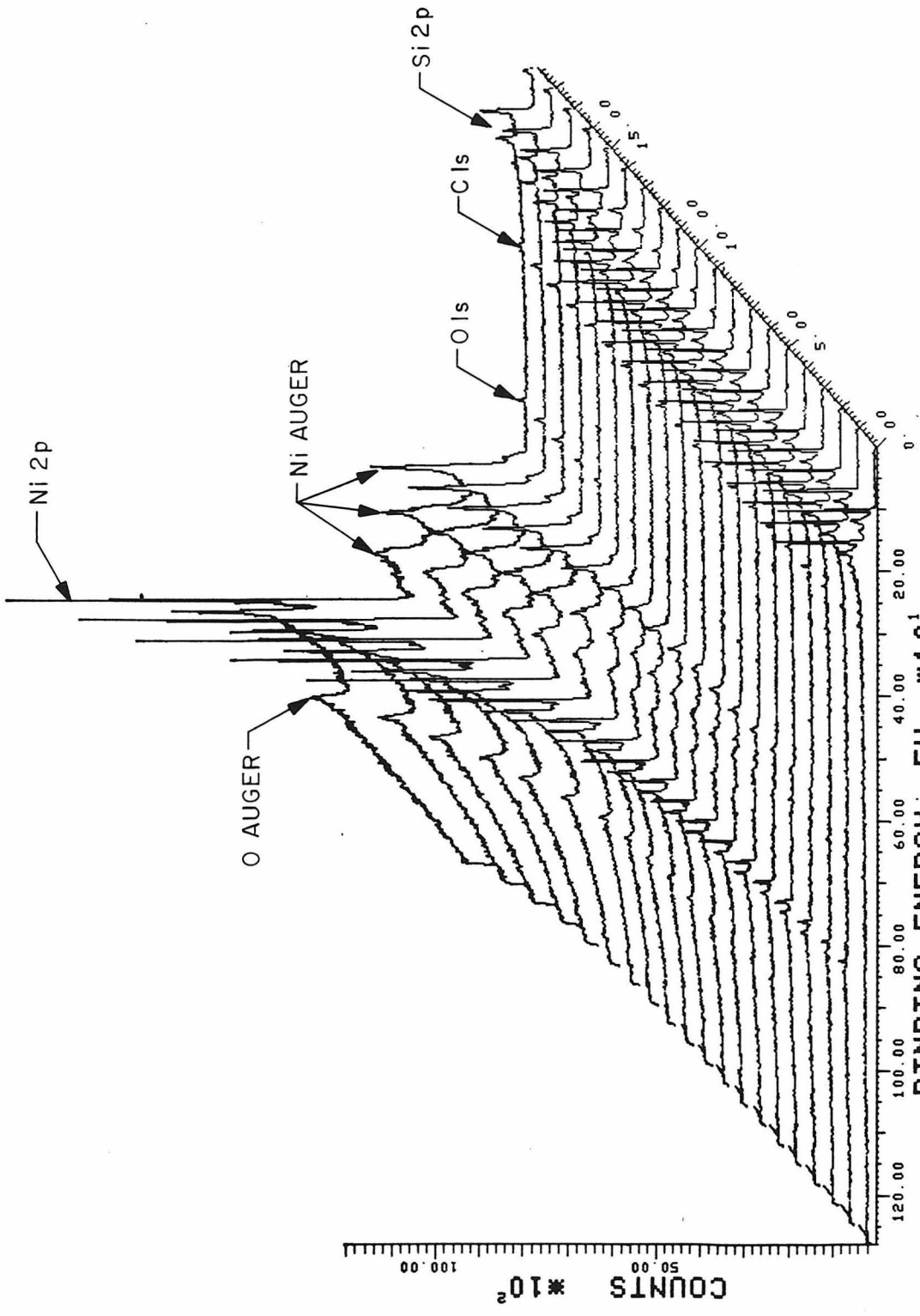

Figure 1: 3-dimensional plot of the wide scan XPS spectra obtained as a function of increasing Ni coverage.

the parent photoelectron peak but later lost energy to inelastic scattering events while passing through the solid. The decrease in the background beginning at 1000 eV is a result of a decrease in the analyzer transmission function for low kinetic energy electrons. Figure 2 displays an expansion of the 50-150 eV region of Figure 1. Here the details of the Si 2p evolution may be seen more clearly. The spectrum in the foreground again corresponds to the pure Si substrate. As sequentially more Ni is evaporated, the Si 2p peak at ∿100 eV decreases in intensity because of attenuation by the metal overlayer. In the final spectrum, which corresponds to 1.9×10^{16} Ni/cm^2, Si is no longer detectable. The broad peak at ∿117 eV is a plasmon, which is an inelastic loss structure due to the excitation of collective valence electron oscillations. This structure is also seen to decrease with the Si 2p intensity. The weaker Ni 3p and Ni 3s core lines at 68 eV and 112 eV, respectively become more intense as the Ni overlayer increases.

In order to study the details of the chemistry occurring at the Ni/Si interface, the Ni 2p and Si 2p core lines were examined in more detail. In Figure 3, the Ni $2p_{3/2}$ spectra for each of the sequential depositions are shown. The first detected Ni $2p_{3/2}$, corresponding to 8.0×10^{13} Ni/cm^2, occurs at 853.6 eV. For the Si <100> surface, one monolayer of Si atoms corresponds to 6.8×10^{14} atoms/cm^2. Using this number, the first Ni 2p spectrum corresponds to 0.1 monolayer of Ni. The Ni 2p position eventually shifts to that found for Ni metal at 852.5 eV as more Ni is added. The large chemical shift of 1.1 eV indicates that the initial monolayers of Ni experience strong

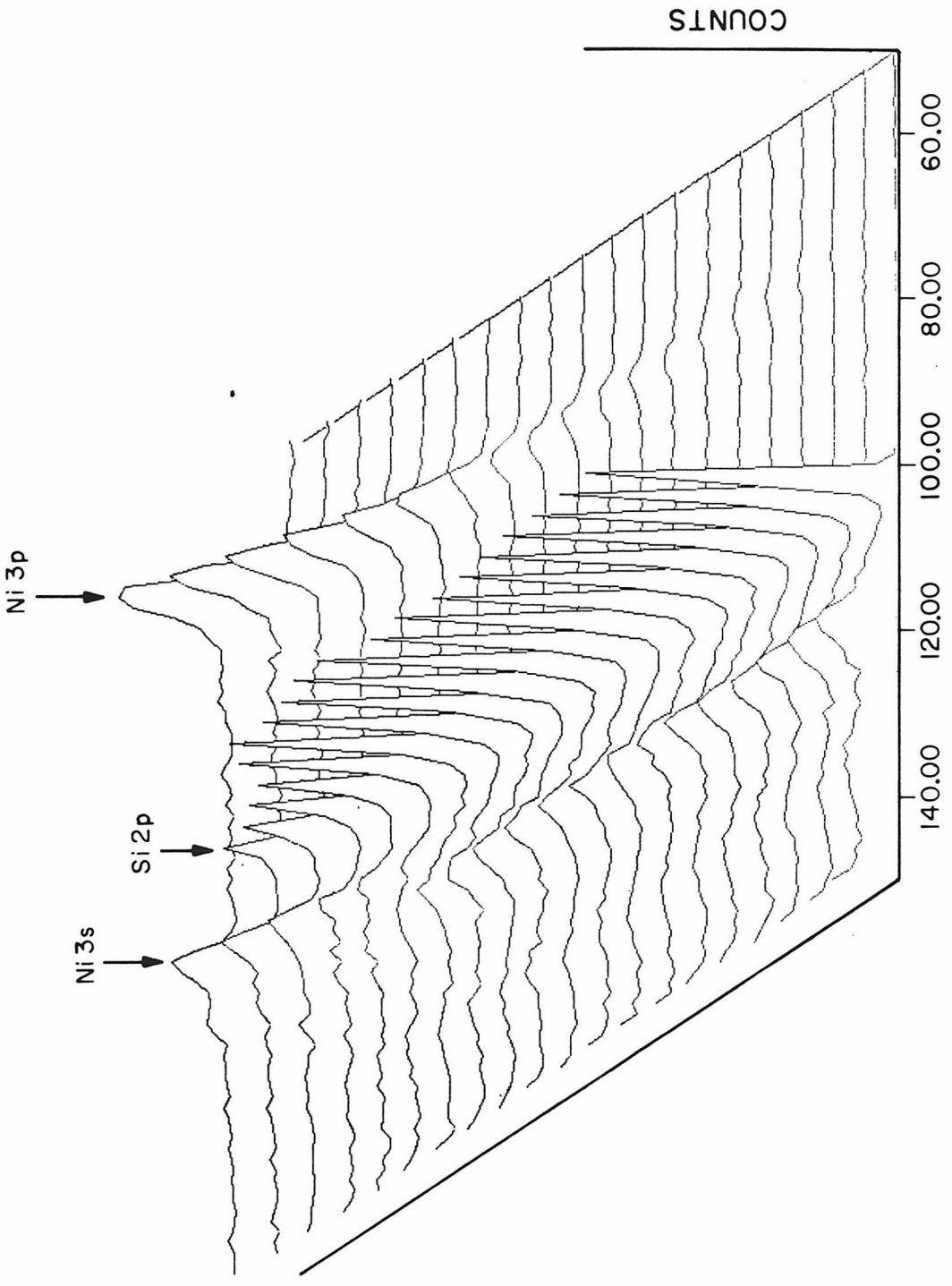

Figure 2: 3-dimensional plot showing in expanded detail the progression of the Ni and Si core lines as a function of increasing Ni coverage.

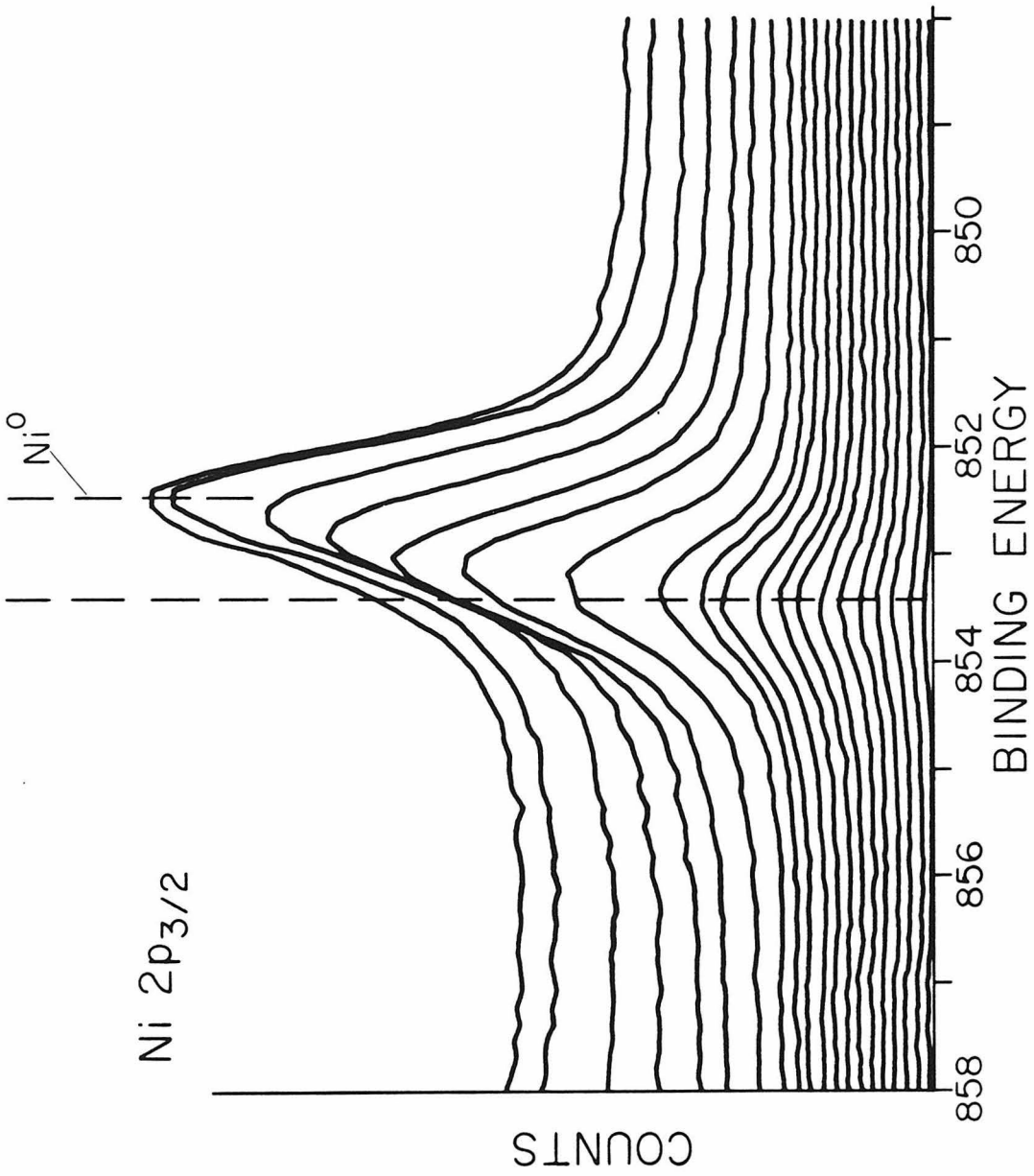

Figure 3: The Ni $2p_{3/2}$ spectra obtained after sequential depostions of thin Ni films on <100> Si.

chemical interactions with the Si substrate even at room temperature. Aggregation effects can be ruled out with variable temperature studies on a non-reactive substrate. This will be discussed in section B-2. The high binding energy interface signal persists for many depositions before beginning to shift toward the Ni metal position. Approximately 5-6 monolayers of Ni are present when the shift begins. This suggests that the signal may be a reasonable representation of the true interface, but certainly the effect of the vacuum on the interface structure cannot be disregarded. This point will be discussed further later. The fact that the Ni 2p signal shifts gradually from the interfacial binding energy to that for Ni metal without a significant increase in the full width of the signal suggests a compositional gradient rather than a sharply defined interfacial compound.

In Figure 4, the Si 2p signals corresponding to the Ni $2p_{3/2}$ signals discussed above are shown. These spectra are plotted in reverse — the pure Si substrate signal is in the background. As sequentially more Ni is deposited, the Si 2p intensity decreases as expected from attenuation by the metal overlayer. Notice in the initial spectra, the Si $2p_{1/2}$ - Si $2p_{3/2}$ spin orbit splitting is resolved. As the Ni overlayer continues to build, this resolution is lost. Toward the end of the sequence, the Si 2p spectra appear as broad unresolved peaks. This may be explained as follows. A large part of the initial Si 2p signal arises from the underlying crystalline substrate. As more Ni is deposited, the Si atoms at the Ni/Si interface represent a larger and larger contribution to the total signal relative to the underlying substrate Si. Spectra in

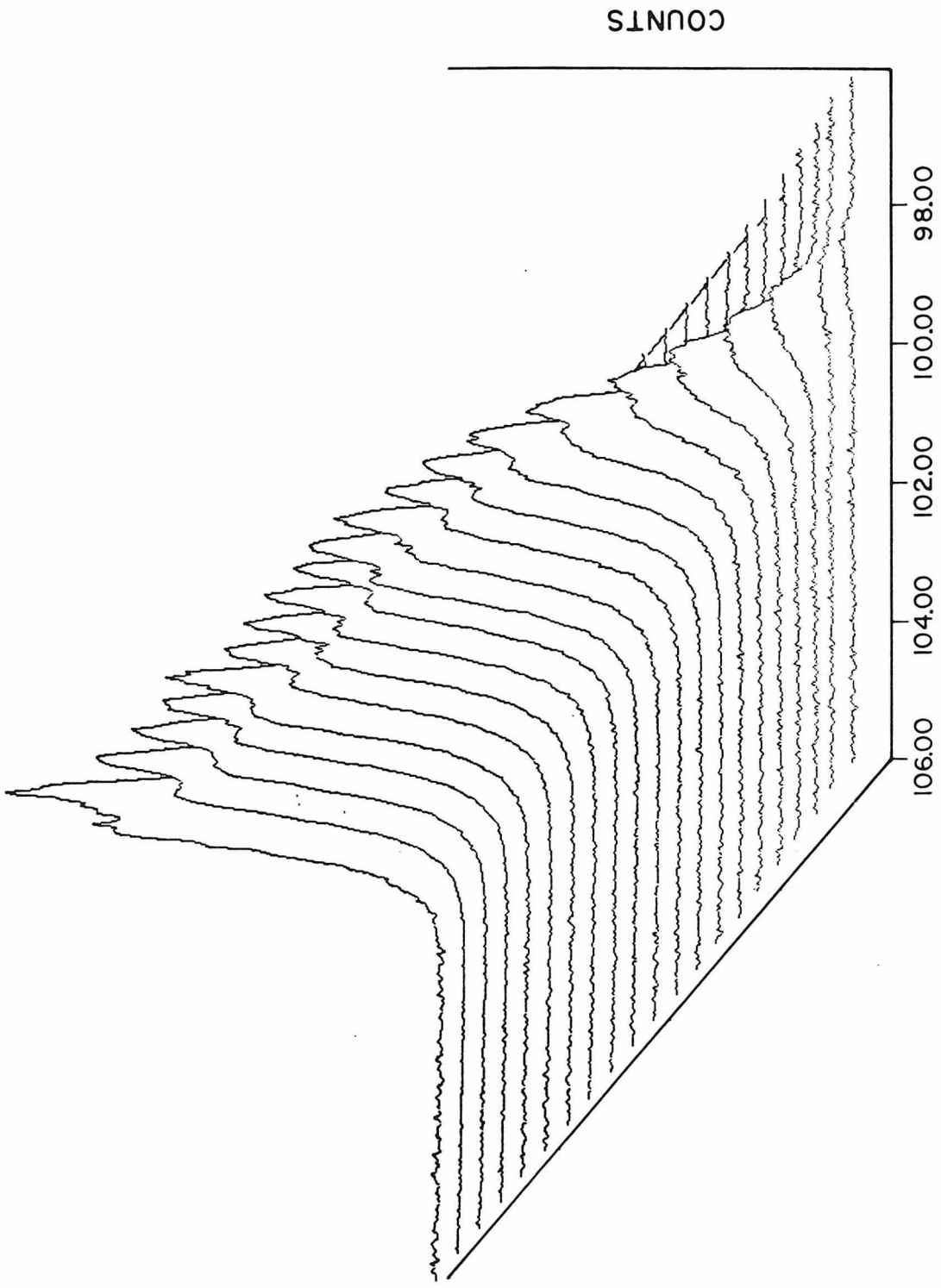

Figure 4: 3-dimensional plot of the Si 2p XPS spectra as a function of increasing Ni coverage.

which the spin-orbit splitting is not resolved suggest the presence of two peaks chemically shifted from one another by 0.3 - 0.6 eV (the spin-orbit splitting is 0.6 eV). When sufficient Ni has been deposited, the signal from the interface should dominate the Si 2p spectrum. Further evidence for this Si 2p interface signal is presented in the following.

The relative shifts of the Ni 2p and Si 2p signals are best illustrated in Figure 5. In the top curve, the binding energy of the Ni $2p_{3/2}$ core line is plotted versus Ni coverage. Notice that the position of the line remains constant at various submonolayer coverages and relatively constant up to several monolayers coverage before gradually shifting to the Ni metal binding energy at 852.2 eV. As mentioned previously, this gradual shift is suggestive of a graded interface rather than a sharply defined interfacial compound. The Si 2p binding energy versus Ni coverage is shown in the lower curve. The initial decrease in the binding energy from 99.25 to 99.15 eV for 0 and $\sim$0.15 monolayer coverages, respectively, is attributable to band bending. It is consistent with work reported by Spicer, *et al.*,[7] which demonstrated that Fermi level pinning occurs at 0.1 - 0.2 monolayers of metal coverage. As the Ni coverage increases, the Si 2p gradually shifts to lower binding energy relative to the Si substrate. This indicates the presence of a chemically shifted Si 2p interface peak, which was first suggested earlier due to the inability to resolve the spin-orbit components in the Si signal. Like the Ni 2p signal, the shift of the Si signal is smooth and gradual, again consistent with a graded interface. Because of attenuation by the Ni overlayer, the

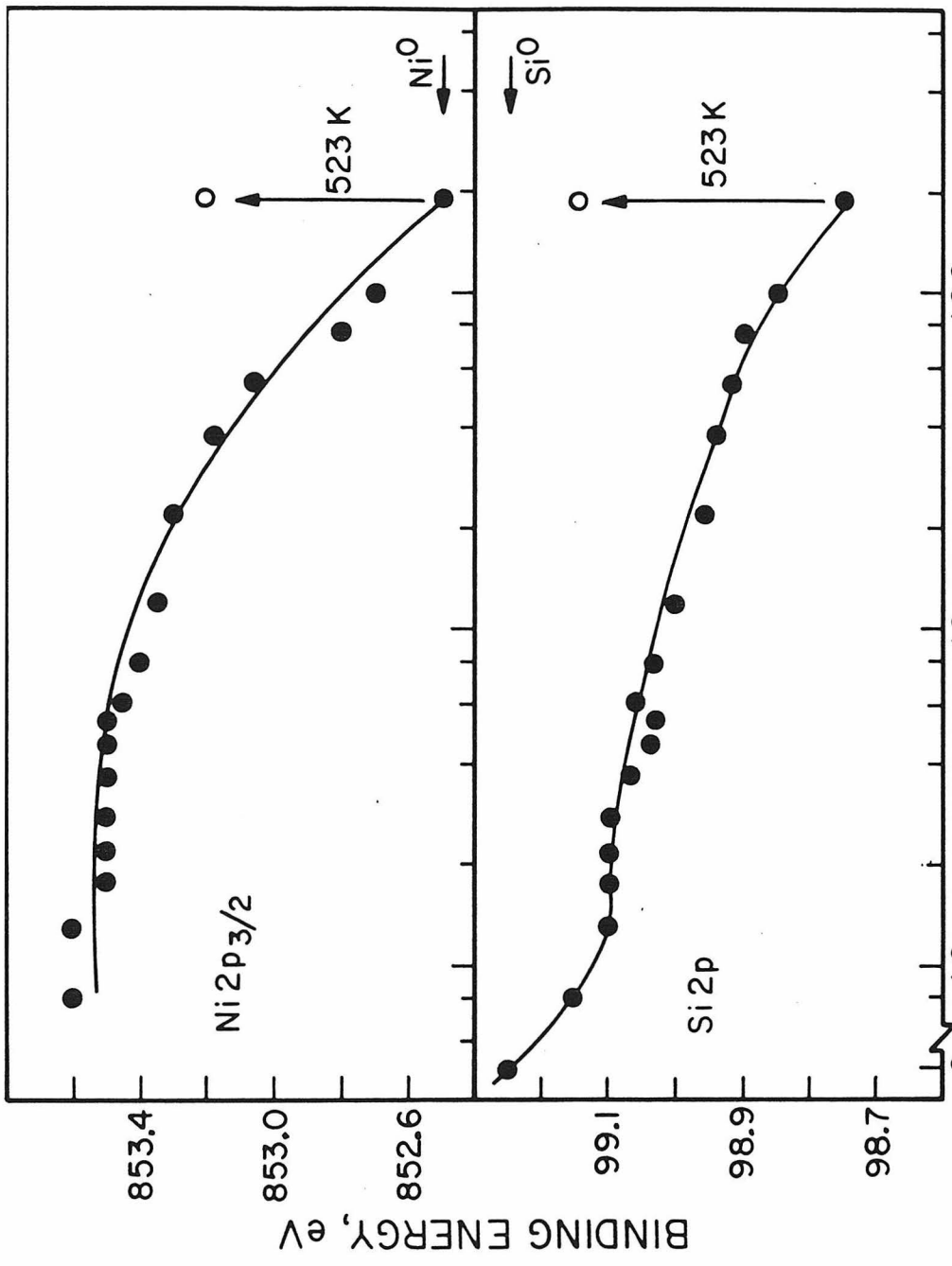

Figure 5: Plot of the Ni $2p_{3/2}$ and Si 2p maxima as a function on Ni coverage.

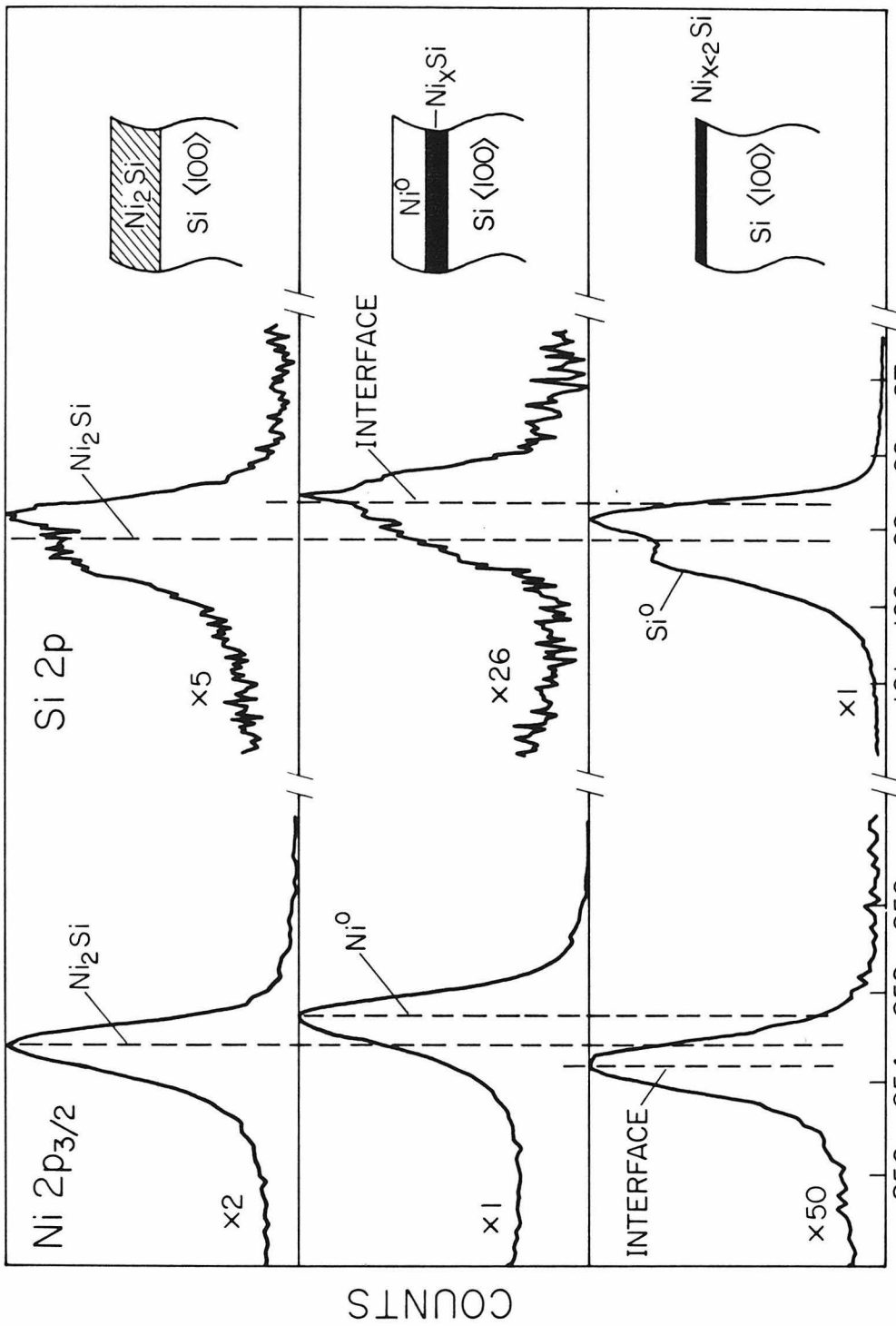

Figure 6: The Ni $2p_{3/2}$ and corresponding Si 2p spectra obtained after (a) ∿ 0.2 monolayers of Ni on <100> Si, (b) ∿30 monolayers of Ni on <100> Si, and (c) final 250° heat treatment.

last observable Si signals correspond to the region of the interface next to the Ni^{o} overlayer. Conversely, the first Ni 2p signals represent the interfacial region next to the Si^{o} substrate. Notice that the first Ni 2p signals are shifted toward higher binding energy relative to Ni metal, while the last Si 2p signals are shifted toward lower binding energy with respect to pure Si. This is consistent with charge transfer from Ni to Si occurring at the Ni/Si interface. After 1.9×10^{16} Ni/cm^2 have been deposited and a pure Ni metal signal established, the sample was heated *in situ* to form Ni_2Si. The resulting Ni 2p and Si 2p binding energies are plotted in Figure 5 for comparison. It can be seen from the differences in binding energy that although the interfacial Ni and Si atoms have clearly reacted at room temperature, the reaction product is not the bulk phase Ni_2Si.

Figure 6 summarizes the Ni 2p and corresponding Si 2p signals for a <100> Si substrate with ∿0.1 monolayer Ni (Figure 6a), ∿30 monolayers Ni (Figure 6b), and the Ni_2Si film after heat treatment (Figure 6c). The Ni 2p signal in Figure 6a corresponding to submonolayer coverage of Ni is 0.4 eV higher in binding energy than the bulk Ni_2Si signal in Figure 6c. As discussed in detail in Chapter III, this suggests that the local coordination environment of the Ni atoms at the interface is more Si rich than that found for Ni in bulk Ni_2Si. In Chapter III, the Ni 2p signal from the Si/Ni_2Si interface was found to be shifted 0.7 eV higher in binding energy than the bulk Ni_2Si signal. This was interpreted to be due to Ni bound in the interstitial voids of the Si lattice. This results in a coordination environment around Ni of six octahedrally oriented and four tetrahedrally oriented Si

ligands. In the thin Ni film experiments, the interfacial signal is only 0.4 eV upfield from Ni_2Si, indicating the Ni atom in this case sees more Si in its coordination sphere than it would in Ni_2Si, but less Si than it would in the interstitial voids of pure silicon. We suggest this 0.4 eV shift is due to Ni bound in the interstitial voids in the immediate vicinity of the silicon surface. The possibility that the Ni atom is sitting directly on the Si substrate surface is ruled out by the temperature experiments presented in the next section. Due to termination of the Si surface by vacuum, these voids may be incomplete - perhaps even "pockets". Another possibility for the difference in binding energy is that surface reconstruction may strain an otherwise perfect interstitial void. This in turn will affect the Ni-Si bond lengths and bond strengths, which can have a significant effect on the observed Ni 2p binding energy. The corresponding Si 2p in Figure 6a is that of the pure Si substrate since the reacted Si signal is too weak to be detected in the presence of the strong substrate signal.

In Figure 6b, the overlayer is sufficiently thick that only the Ni 2p corresponding to Ni metal is detected. In the respective Si 2p region, the exponential attenuation of photoemission intensities may be exploited to investigate the chemical nature of the remainder of the interfacial region. The last detectable Si 2p must necessarily correspond to the "topmost" silicon atoms of the interface. Relative to the Si 2p signal from the bulk Ni_2Si shown in Figure 6c, the Si 2p interface signal is shifted 0.5 eV toward lower binding energy. This indicates that the Si atoms in this region are in a more Ni-rich

local environment than that found in Ni_2Si. In Chapter III, the first Si 2p interface signal for the Si atom at the Ni/Ni_2Si interface was found to be 0.4-0.6 eV downfield of the Ni_2Si signal. This was interpreted to mean that a metallic-like Si was substituted in the fcc lattice of Ni metal. In this environment it has a ligancy of 12 Ni, which accounts for its extremely low binding energy relative to Si^o. Because of the similarity in the Si 2p binding energies obtained for Si at the Ni/Ni_2Si interface and for Si at the "top most" region of the Ni/Si interface, we interpret the latter signal as also being due to Si substituted in the fcc lattice of Ni metal. Because $\sim$30 monolayers of Ni have been deposited at the time this signal is observed in the thin film experiment, it is quite reasonable that the limiting Si environment at the Ni_xSi_y/Ni interface should be the same as the limiting environment found at the Ni_2Si/Ni interface.

Notice that the binding energy of the Si 2p core level from Ni_2Si (Figure 6c) is observed at an energy similar to that obtained from the core level of the Si substrate (Figure 6a). This is attributable to the difference in final state relaxation anticipated for semi-metal and semiconductor materials and also to the referencing ambiguities encountered with semiconductors. We avoid these problems by referencing the interface signals to the final Ni_2Si phase rather than to the initial Si substrate.

To summarize Figure 6, the first detectable Ni 2p signal and the last detectable Si 2p signal indicate that the Ni/Si transition region cannot be described as a single unique phase. Instead, these signals indicate the presence of a chemically graded transition region which

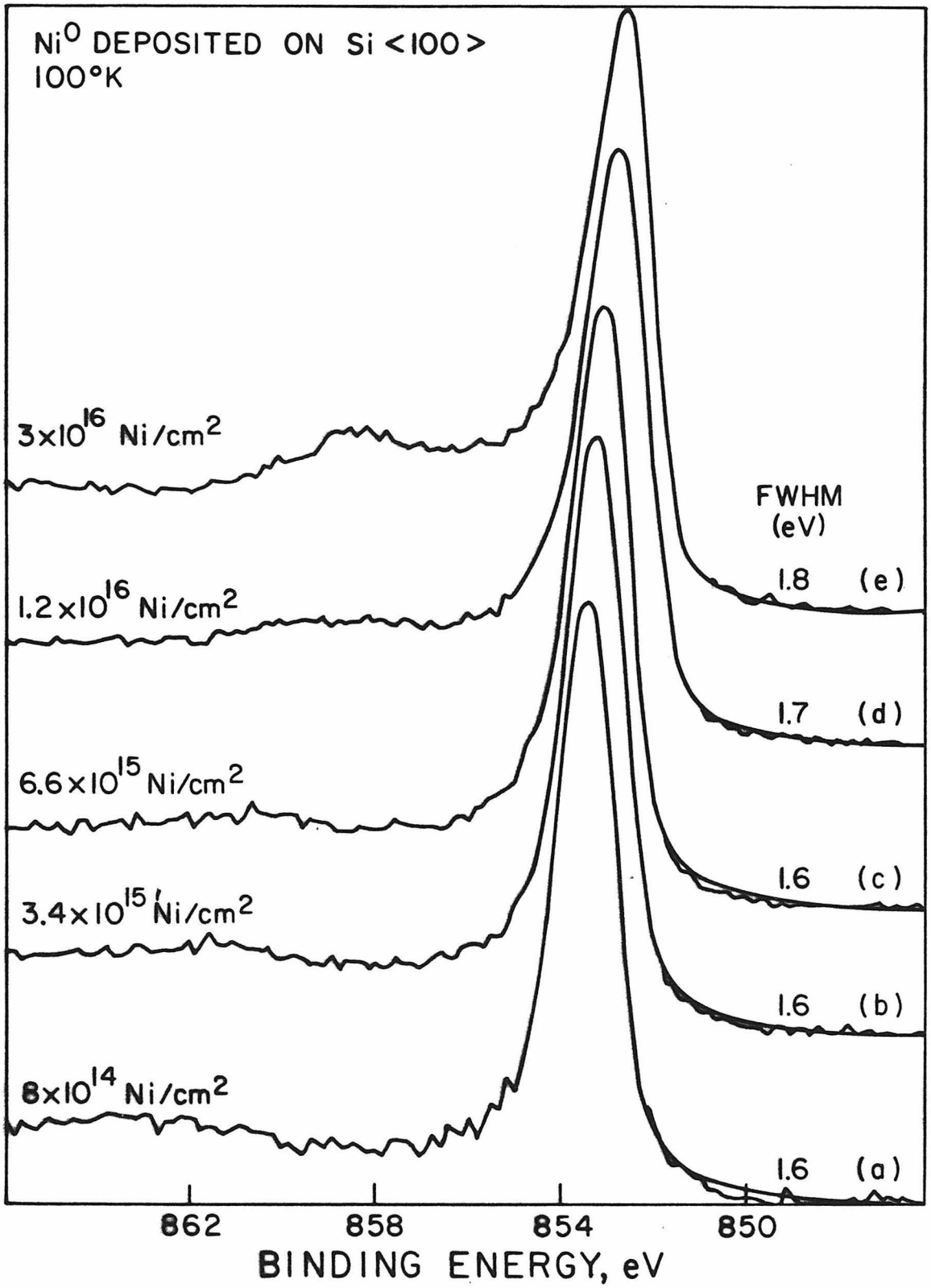

Figure 7: The Ni $2p_{3/2}$ spectra corresponding to various Ni coverages on Si <100> at 100° K.

ranges in stoichiometry from Ni atoms in the Si interstitial voids on the <100> Si side of the interface to Si atoms substituted in the fcc lattice of Ni metal on the Ni^{o} side of the interface. The possible presence of Ni_2Si or some other bulk Ni silicide between the boundaries of this interface cannot be directly determined from these experiments. However, if the interfacial width is relatively narrow, it seems unlikely that a precise compound stoichiometry could be defined.

2. Substrate Temperature Effects

The chemical nature of the Ni/Si interface as a function of the substrate temperature during the Ni depositions was investigated. Samples were cooled *in situ* to 100°K before metal deposition. This temperature was maintained throughout the Ni evaporation procedure and during the data accumulation periods. Where higher substrate temperatures are indicated, the sample prepared at 100°K was allowed to warm *in situ* to that temperature. The sample was allowed to remain at that temperature for at least one hour before beginning data accumulation. This allowed time for the sample to reach a steady-state composition.

Figure 7 displays Ni $2p_{3/2}$ spectra obtained at various Ni coverages on a Si <100> substrate at 100°K. The Ni coverages range from 8×10^{14} Ni/cm^2 (∿1.2 monolayers) to 3×10^{16} Ni/cm^2 (∿44 monolayers). In Figure 7a, which corresponds to a 1.2 monolayer coverage, the Ni 2p falls at a binding energy of 853.4 eV. As the Ni coverage increases, the binding energy shifts downfield until it reaches that

of pure Ni metal at 852.6 eV. The full width at half maximum (FWHM) for the Ni 2p signals is indicated in the figure. The peaks maintain the FWHM of 1.6 eV through a Ni coverage of 6.6×10^{15} Ni/cm^2 ($\sim$9.7 monolayers). At higher coverages, there is an increase in the signal width to 1.7 eV and finally to 1.8 eV. There are two possibilities for this increased width: 1) the peak envelope may contain some small intensity from underlying Ni species with slightly different chemical shifts or 2) it may simply be a result of the increased asymmetry characteristic of the Ni metal signal. The large chemical shifts observed for the low coverages of Ni clearly indicate that a substantial chemical interaction is occurring between the Ni and the Si substrate, even at 100°K.

Figure 8 shows the Ni $2p_{3/2}$ binding energies obtained at several temperatures (100°, 298°, 523°K) as a function of the Ni coverage. In the lower curve, Ni metal was deposited on a Si substrate with $\sim$25Å thermal oxide. An oxidized substrate was chosen to compare with the <100> Si substrate in the upper curve since it has been demonstrated that Ni films on SiO_2 will not react to form silicides even at temperatures as great as 800°C.[8] Consider the case of Ni on SiO_2 first. In the lower curve, the initial data points at each of the three temperatures correspond to a Ni coverage of 6×10^{14} Ni/cm^2 or $\sim$1 monolayer Ni. At a substrate temperature of 100°K, the Ni 2p signal is observed at 853.99 eV. This extremely high binding energy cannot be explained by the Ni atom being oxidized at the surface. If that were the case, as the temperature increased one would expect more oxidation to occur. Instead, one finds that at temperatures of 298°K

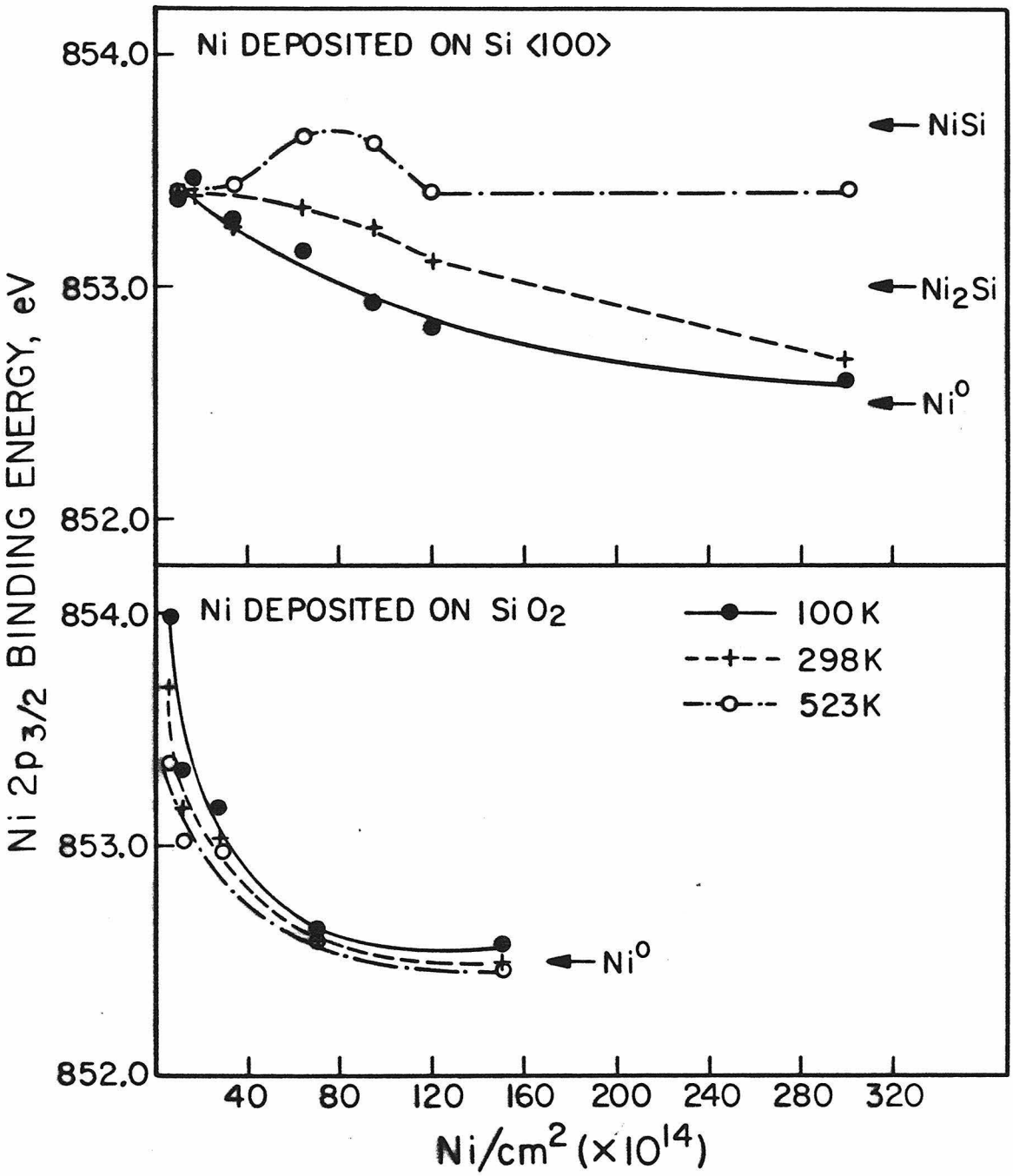

Figure 8: Plot of the Ni $2p_{3/2}$ maxima as a function of Ni coverage and substrate temperature. The upper curves correspond to Ni deposited on crystalline Si. The lower curves correspond to Ni deposited on SiO_2.

and 523^{o}K, the Ni 2p binding energy is reduced to 853.68 eV and 853.35 eV, respectively. In addition, analysis of the appropriate electrochemical potentials indicates Ni metal is unable to reduce SiO_2. The shift of the binding energy to lower values as the temperature is increased is more consistent with the degree of aggregation of the Ni atoms. At low substrate temperatures, the mobility of the Ni atom on the SiO_2 surface is low and, hence, the atoms remain relatively dispersed. At higher temperatures, the mobility increases and the atoms are free to coalesce. As Ni atom clusters on the surface increase in size, their characteristics begin to approach that of Ni metal and, hence, their binding energies decrease. The tendency of the binding energy to decrease as bulk Ni is approached is related to final state relaxation affects. In a metal, the passive valence electrons are free to relax toward the positive hole created by the photoemission process. The effect is always to lower the magnitude of the binding energy because the photoelectron acquires the energy lost from the passive electrons being polarized towards the region of more attractive potential.[9] An isolated atom is deprived of these passive electrons and it is thus observed to have a higher binding energy. The tendency of Ni atoms on SiO_2 to coalesce as the temperature is increased has been documented using scanning electron microscopy.[8] It can be seen from Figure 8 that at a Ni coverage of $\sim 7.0 \times 10^{15}$ Ni/cm^2, the Ni atoms have coalesced enough that the binding energy of bulk Ni metal (852.5 eV) has been established.

Consider now the top curve with Ni deposited on Si <100>. The initial data points again correspond to approximately 1 monolayer of

Ni. In this case, the Ni $2p_{3/2}$ binding energies obtained at 100^{o}, 298^{o} and 523^{o}K all fall at 853.4 eV. Aggregation effects lead to changes in final state relaxation energy, as well as possible changes in the chemical bonding environment within the metal clusters. If these effects contributed to observed binding energies for Ni on <100> Si, a temperature dependence would be found, as in the case of Ni on SiO_2. Since different temperatures result in the same binding energy at ∿1 monolayer Ni coverage, the observed Ni 2p shift must be primarily chemical in nature.

Once aggregation effects have been ruled out, the next question that can be addressed concerns the location of the initial Ni atoms. Two possibilities exist: 1) the Ni atom is bound on the Si substrate surface or 2) the Ni atom drops into the Si lattice. It is known from marker experiments that Ni is the diffusing species in silicide formation.[10] If at a substrate temperature of 100^{o}K the Ni atom is bound on the Si surface, then one would expect it to drop inside the Si lattice at the higher temperatures. If not at 298^{o}K, then certainly at 523^{o}K. Inside the interstitial voids of the Si lattice, the Ni atom would experience a higher degree of ligancy (ten Si atoms) than it could bound to only the surface of the Si. In Chapter III, it was demonstrated that the Ni 2p signal is extremely sensitive to its exact coordination environment and, hence, one should see a large difference in the binding energies between the two cases. But in Figure 8, only one common binding energy is observed. This implies the Ni atom must have dropped into the Si lattice even at 100^{o}K. Additional evidence for this is obtained by noting that the binding

energies at ∿1 monolayer coverage are greater than the energy observed for Ni_2Si (853.0 eV). This means the initial Ni atom must have a higher degree of ligancy than that found for Ni in Ni_2Si. This is not possible if the Ni atom is bound on the surface (the details of the Ni_2Si structure may be found in Chapter III). The possibility that the Ni atom has gone substitutional in the Si lattice is also ruled out since its ligancy is only four in this environment, which is considerably less than the Ni ligancy found in Ni_2Si. A third possibility one might argue is that the initial Ni atoms bind to surface defect sites and are so securely bound that they do not proceed into the Si lattice even at the high temperatures. But notice that all three data points fall at the same energy at ∿1 monolayer of Ni. One monolayer of defects cannot reasonably exist at the substrate surface. Thus, in conclusion, the coincidence of the three initial data points can be explained by postulating that the Ni atoms must go below the Si surface, even at $100^{\circ}K$.

In Figure 8, the curve obtained at $523^{\circ}K$ with Ni deposited on Si <100> displays a maximum at $\sim 8 \times 10^{15}$ Ni/cm^2. The origin of this "hump" in the curve may be explained as follows. The Ni 2p data points just below the maximum at low Ni coverages have a lower binding energy because these signals are due to Ni atoms in the Si interstitial voids just below the substrate surface. In these Si voids, the Ni atoms have a high coordination number, but because of the termination of the solid by a vacuum, the Si voids may be only partially complete - perhaps "pockets". Over the next 5 monolayers of deposited Ni, a maximum in the curve is observed. This indicates the

Ni atoms in the environment are in a more Si-rich environment than they were initially at lower Ni coverages. In Chapter III, it was shown that the Ni 2p binding energy is extremely sensitive to the environment - not only the number of nearest neighbors, but the bond lengths and strengths can substantially affect the observed core line positions. It has been shown that a Si crystal terminated against a vacuum has 1-2 monolayers of non-registered Si atoms at the surface.[11] Interstitial Si voids are present in this region but are distorted compared to a perfect Si lattice. Channeling analysis indicates the reconstructed region is 1-2 monolayers deep, but a 0.15 Å displacement from the perfect Si crystal is required for detection by the technique.[11] Smaller distortions (<0.15 Å) probably exist many monolayers deeper. Such displacements are still high on a chemical scale. Bond length changes of several hundredths of an angstrom are sufficient to change the valence charge distribution around an atom. Thus, it is not unreasonable that the binding energy of the Ni atom could respond to reconstruction and disorder on a scale considerably smaller than that detectable by channeling techniques. Unfortunately, one is not able to quantify the effect as in channeling measurements, but it indicates a difference in the Ni environment nontheless. We suggest, then, that the peak in the curve in Figure 8 at $\sim 8 \times 10^{15}$ Ni/cm^2 is due to Ni atoms bound in the Si interstitial voids in the reconstructed region in the vicinity of the substrate surface.

After the maximum in the curve, the Si crystal is now terminated against a Ni silicide layer (Ni_xSi_y). The original reconstructed Si has been consumed. Now the Ni atoms see slightly different Si voids.

The voids are still not the perfect octahedral/tetrahedral cages found in a perfect Si crystal lattice since the presence of the Ni_xSi_y overlayer must induce some reconstruction or distortion itself. Nevertheless, the important point is that the voids encountered by the Ni at this point are again structurally distinct. The data indicate the Ni in the region is in a less Si-rich environment than it was previously (0.2 eV downfield shift). The downfield shift could also be explained by the same number of Si atoms in the Ni coordination sphere, but with weaker Ni-Si bonds due to distortion of the Si cage. The Ni 2p binding energy stays constant now as the Ni coverage increases. This is consistent with the idea that the diffusing Ni atoms must be seeing the same structural Si void as the Ni_xSi_y/Si interface proceeds into the Si crystal.

The question arises as to why the Ni environment indicated by the maximum in the 523°K curve is not observed at higher Ni coverages. After all, this region is close to the surface and should constitute a large part of the total Ni signal. We suggest the presence of the silicide layer below this original surface layer affects its structure. In particular, at this temperature it is able to reorient with respect to the layer below.

At the highest Ni coverage investigated, 2.8×10^{16} Ni/cm^2, the Ni 2p binding energy obtained at 523°K is still not characteristic of the bulk phase Ni_2Si or NiSi. This is in contrast to the case of Pd on Si where it has been reported that the bulk compound Pd_2Si is present at monolayer coverage of Pd.[12] The authors in this study, however, relied on an Auger intensity analysis for this conclusion.

The assumptions made during the course of the analysis make questionable the conclusion that Pd_2 Si is present at the interface.

The curves obtained at 100° and 298°K for Ni deposited on Si do not show the pronounced structure of the 523°K curve. Instead, they gradually shift toward the Ni metal binding energy. The gradual taper of the 100°K curve compared to the sharp drop obtained with Ni deposited on SiO_2 at 100°K indicates that substantial Ni diffusion and reaction is able to occur at this low temperature. A similar trend is observed in the 298°K curve, except that the shift in the binding energy is still more gradual. This indicates a wider reacted layer is present relative to that found at 100°K.

D. SUMMARY

In this chapter, the chemical nature of the as-deposited Ni/Si interface was investigated using multiple monolayer depositions of Ni on Si <100>. The Ni 2p and Si 2p core levels were examined as a function of Ni coverages and substrate temperature.

Using room temperature depositions of Ni metal on Si <100>, it was demonstrated that the first detectable Ni 2p signal and the last detectable Si 2p signal could be used to examine the nature of the interface. It was concluded that the Ni/Si interface could not be described as consisting of a unique well-defined compound. Instead, the data indicate the presence of a chemically graded transitional layer. This layer ranges in stoichiometry from Ni atoms bound in the Si interstitial voids on the <100> Si side of the interface to

Si atoms substituted in the fcc lattice of Ni metal on the Ni^{o} side of the interface.

When compared to the results presented in Chapter III, this chapter clearly demonstrates that the Ni atoms at the Si/Ni_2Si interface are in a more Si-rich environment than that found at the Si/vacuum interface. We proposed in Chapter III that the environment of the Ni atom corresponding to the first detectable Ni 2p signal at the Si/Ni_2Si interface consisted of the Ni atom bound interstitially in a Si void. At the Si/vacuum interface, the Ni 2p binding energies are consistent with Ni atoms bound in incomplete or distorted Si voids in the immediate vicinity of the substrate surface. The difference in the Ni 2p binding energy between the Si/Ni_2Si and Si/vacuum interface clearly indicates the presence of an extended Ni_2Si overlayer has affected the environment of the Ni atoms at the interface. Care should be exercised when drawing conclusions concerning the stoichiometry and bonding at "realistic" interfaces using data obtained from sequential depositions or "less-realistic" interfaces.

The chemical nature of the Ni/Si interface as a function of the substrate temperature was also investigated. It was shown that a substantial chemical interaction occurs between the deposited Ni and the Si substrate at temperatures as low as $100^{o}K$. Nickel metal was deposited on a SiO_2 substrate at various temperatures to investigate the effect of Ni aggregation on the observed binding energies. On SiO_2, $\sim 7.0 \times 10^{15}$ Ni/cm^2 were required to produce the binding energy characteristic of bulk Ni metal. Comparison of the Ni 2p binding energies obtained with $\sim$1 monolayer of Ni on <100> Si at

different temperatures with the results obtained on SiO_2 indicated that aggregation effects were not responsible for the observed chemical shifts.

The dependence of the Ni 2p binding energy on the substrate temperature also demonstrated that the initial Ni atoms deposited on Si surface are not bound on the surface. Instead, they drop into the interstitial Si voids. This occurs even at temperatures as low as $100^{o}K$.

The behavior of the Ni 2p binding energy as a function of Ni coverage at $523^{o}K$ indicated several distinct Ni environments were observable. In the first region, which occurs at monolayer coverages, the Ni atoms drop into the Si voids in the immediate vicinity of the substrate surface. Because of reconstruction of the sample surface due to termination by a vacuum, the Ni atoms see only partially complete Si cages. Hence, the binding energy is comparatively low. As several additional monolayers of Ni are deposited, a maximum occurs in the Ni 2p binding energy. We suggest this represents Ni atoms bound in the somewhat deeper Si voids which are complete but still distorted from the effects of surface reconstruction. A third and final plateau occurs in the Ni 2p binding energy as more Ni is deposited (>15 monolayers). We suggest this is a result of Ni atoms bound in the Si voids present in a Si lattice terminated by a Ni_xSi_y overlayer.

References

1) J. L. Freeouf, G. W. Rubloff, P. S. Ho, T. S. Kuan, Phys. Rev. Lett., 43, 1836 (1979)

2) P. S. Ho, T. Y. Tan, J. E. Lewis, G. W. Rubloff, J. Vac. Sci. Technol., 16 (5), 1120 (1979)

3) J. A. Roth, Thesis, University of Southern California, Materials Science Department

4) D. Schmeisser, K. Jacobi, Surface Sci., 88, 138 (1979)

5) C. F. Melius, T. H. Upton, W. A. Goddard III, Solid State Communications, 28, 501,1978

6) J. C. Fuggle, D. J. Fabian, L. M. Watson, J. Electron Spectros. and Related Phenom., 9, 99 (1976)

7) I. Lindau, W. E. Spicer, P. Pianetta, P. W. Chye, C. M. Gardner J. Electron Spectrosc., 15, 197 (1979)

8) R. Pretorius, J. M. Harris, M-A. Nicolet, Solid State Electron., 21, 667 (1978)

9) P. H. Citrin, D. R. Hamann, Phys. Rev. B, 10, 4948 (1974)

10) W. K. Chu, H. Kraütle, J. W. Mayer, H. Müller, M-A. Nicolet, K. N. Tu, Appl. Phys. Lett., 25, 454 (1974)

11) L. C. Feldman, I. Stengaard, P. J. Silverman, T. E. Jackman, The Physics of SiO_2 and Its Interfaces, S. T. Pantelides, ed. (Pergamon Press, 1978)

12) P. S. Ho, T. Y. Tan, J. E. Lewis, G. W. Rubloff, J. Vac. Sci. Technol., 16, 1120 (1979)

13) J. L'Écuyer, J. A. Davies, N. Matsunami, Nucl. Instru. and Methods, 160, 337 (1979)

CHAPTER V

IMPURITY EFFECTS AT THE NICKEL SILICIDE INTERFACES

A. INTRODUCTION

The technological importance of the transition metal silicides has provided the impetus for several investigations concerned with impurity phenomena in solid phase metal-silicon reactions. Such studies have demonstrated that impurities play an important role in determining the silicide phase growth sequence as well as the growth kinetics. In particular, oxygen has been shown to significantly affect silicide compound formation.[1-3]

The relative importance of impurities in interfacial studies is generally overlooked. Interface models of thin film reactions are often idealized without consideration of the unavoidable impurity content. In this chapter, the effect of oxygen contamination on the nickel-silicide interface is investigated.

In Chapter III, the Ni/Ni_2Si and Si/Ni_2Si interfaces were studied by dynamically monitoring the advancing silicide reaction front during *in situ* growth. In the course of this work, photoemission signals from oxygen and carbon impurities were routinely monitored. We observed that the intensity of the carbon and oxygen core level signals increased as the silicide reaction front advanced toward the sample surface. This is illustrated in Figure 1. The upper plot gives the C 1s and O 1s intensity as the Si/Ni_2Si interface advances. The abscissa is given

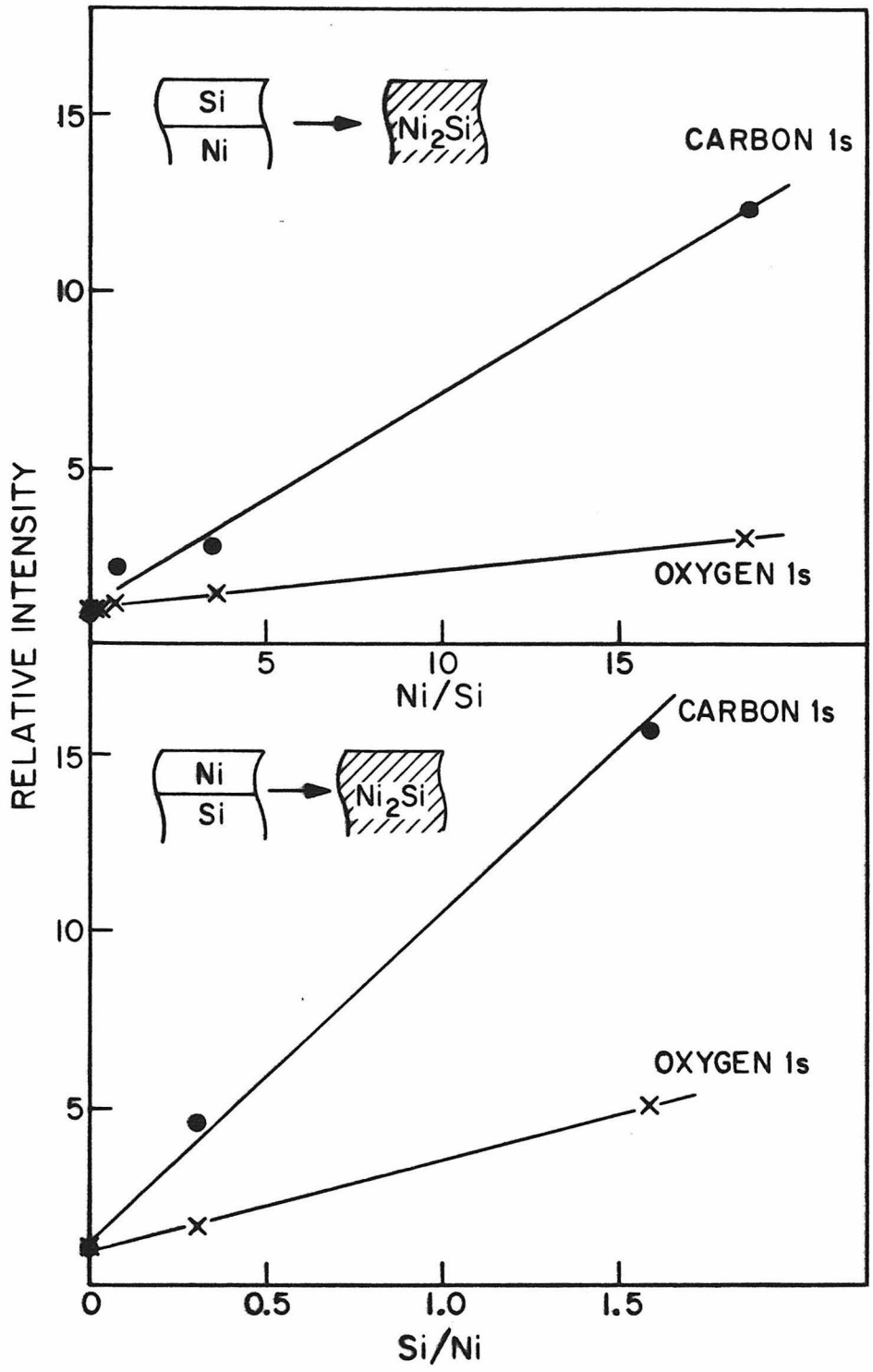

Figure 1: Plot of the carbon 1s and oxygen 1s spectral intensities as the silicide reaction front advances toward the sample surface.

in terms of the Ni $2p_{3/2}$/Si 2p intensity ratio. The units are arbitrary and are only indirectly related to the thickness of the reacted layer. The increasing Ni/Si ratio serves to indicate an advancing reaction front. The carbon and oxygen intensities at a Ni/Si ratio of zero represent the contamination level present in the evaporated Si film before any reaction has occurred. The intensity scales have been normalized to give an initial value of one for both impurities. It was found that the intensity of the signal due to oxygen within the observation depth of the spectroscopy doubled as the Si/Ni_2Si interface approached the surface. The carbon intensity increased 12-fold. A similar phenomenon was observed as the Ni/Ni_2Si interface advanced toward the sample surface as shown in the lower curve in Figure 1. Here the C 1s and O 1s intensities are plotted against the Si 2p/Ni $2p_{3/2}$ intensity ratio. The oxygen intensity increased 5-fold while the carbon intensity increased 17-fold during the course of the silicide reaction. Concurrent with the C 1s and O 1s intensity increase, a weak signal appeared on the high binding energy side of the Si 2p signal as shown in Figure 2. This was again found to occur at both the Ni/silicide and Si/silicide interfaces.

These observations were consistent with a current investigation by D. Scott concerned with the effect of oxygen on the growth kinetics of nickel silicides.[3] Using $^4He^+$ backscattering and $^{16}O(d,\alpha)^{14}N$ nuclear reactions, he has demonstrated that oxygen present in the Ni film accumulates at the Ni/Ni_2Si interface as the silicide is formed. As the oxygen content of the film increases, the growth rate of the

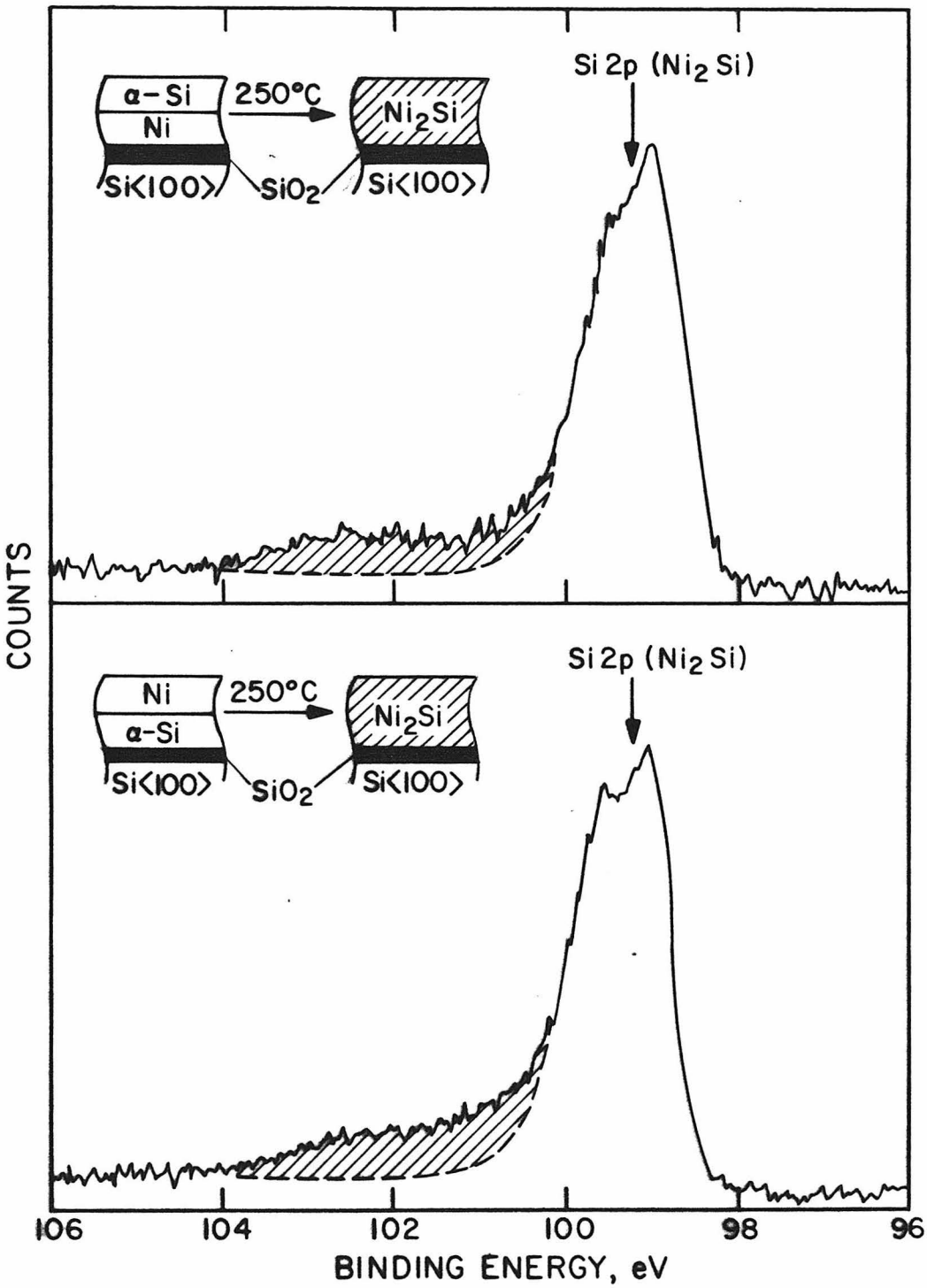

Figure 2: The Si 2p spectra corresponding to the final phase as the Si/Ni_2Si interface (upper plot) and Ni/Ni_2Si interface (lower plot) advance to the sample surface.

Ni_2Si phase decreases. If sufficient oxygen is present, a diffusion barrier is formed that prevents the consumption of the remaining Ni metal and thereby initiates the formation of the second phase NiSi.

The XPS observations and the cited results by D. Scott motivated the work presented in this chapter. In Chapter III, the low intensity signals upfield of the silicide Si 2p were attributed to impurity effects. but were not considered in the subsequent analysis of the interface data. In this chapter, the nature of these low level signals is considered in detail and its possible effect on the chemical structure of the interface is investigated. In addition, the relationship of the observed XPS signals to the diffusion barrier observed by D. Scott is examined.

B. EXPERIMENTAL

The results reported here were obtained using commercial n-type <100> Si substrates with a resistivity of 1 to 10 Ω-cm. The Si wafers were cleaned ultrasonically with trichloroethylene (TCE), acetone, and methanol and then rinsed with deionized water. Just prior to loading for evaporation, the substrate was etched in dilute HF and rinsed again in deionized water. Nickel films, 1280 Å in thickness, were e-beam evaporated at ∿ 35 Å/sec with a background pressure of ∿ 5×10^{-7} Torr.

Several wafers were then implanted with 7.64×10^{15} cm^{-2}, 1.54×10^{16} cm^{-2}, or 2.34×10^{16} cm^{-2} of $^{16}O^{+}$ at 80 KeV. This corresponds to a gaussian oxygen distribution centered ∿ 640 Å below

the Ni surface with peak concentrations of 1, 2, and 3 atomic percent, respectively. The standard deviation, σ, of the oxygen distribution is $\sim$ 330 Å. The background pressure during implantation was $\sim 5 \times 10^{-7}$ Torr.

Prior to examination by XPS, the surface contamination layer that had formed during sample transport had to be removed. A large carbon overlayer was found to be present which could not be removed with a variety of solvents (ethanol, TCE, acetone, methyl ethyl ketone) or acid etches (HCl, HF). We attribute this carbon overlayer to a pump oil contamination obtained during the ion implantation step which had been subsequently polymerized by the implantation process. The carbon contamination could only be removed by plasma oxidation. The samples were placed into a flowing N_2 dry box and first rinsed with ethanol. They were then oxidized for 10 minutes in an O_2 plasma at a pressure of $\sim$ 50 mTorr. The nickel oxide that had formed during the oxidation was etched off by spinning the sample at 3600 rpm and adding dropwise 500 µℓ of 1:1 HCl in ethanol followed by 1000 µℓ of ethanol. The sample inlet port of the spectrometer is connected directly to the N_2 dry box. Consequently, no further oxygen contamination occurred after etching.

The cleaning procedure described above is illustrated in Figure 3. Carbon, nickel and oxygen spectra are shown for each stage in the process. The top spectra were obtained after the ethanol rinse. The C 1s signal is large and almost completely attenuates the signal from the Ni metal. Some oxygen contamination is also evident, but it is

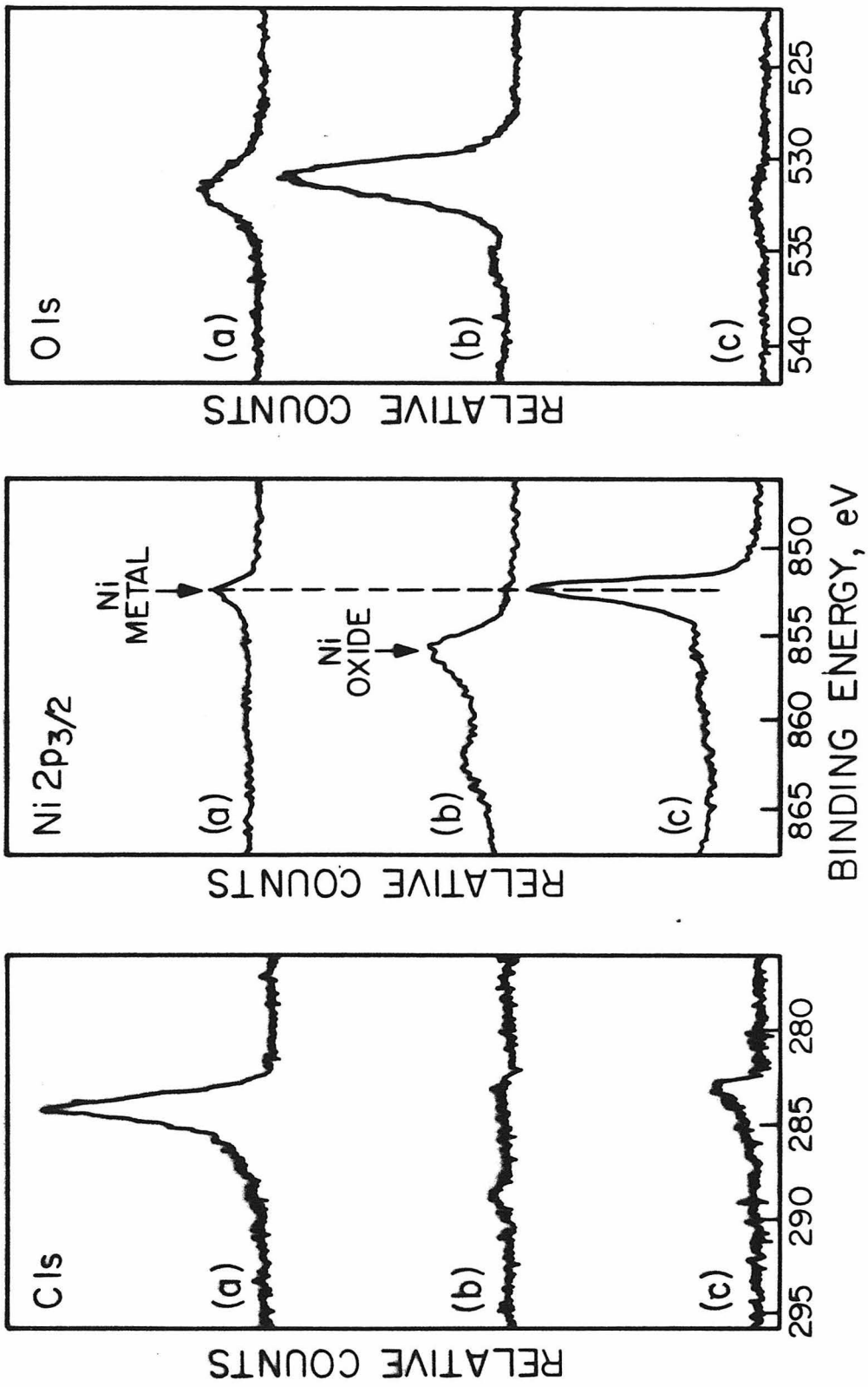

Figure 3: Plots of the carbon 1s, nickel $2p_{3/2}$, and oxygen 1s spectra obtained at various stages in the surface cleaning procedure.

not attributable to NiO since no corresponding peak is observable in the Ni 2p region. The center spectra were obtained after a 10 minute O_2 plasma oxidation. Essentially all of the carbon overlayer has been removed. A nickel oxide $\sim$ 50 Å in thickness has resulted from the oxidation. The additional peak in the Ni spectra at $\sim$ 863 eV is a satellite line characteristic of NiO. The lower panel of spectra in Figure 3 corresponds to the final sample surface obtained after a HCl/ethanol etch and ethanol rinse. A small amount of additional carbon is observed, possibly due to adsorbed solvent. The Ni oxide has been etched away and only a small residual oxygen signal remains.

After establishing sample surfaces that are free of oxide and carbon overlayer contamination, the Ni 2p, Si 2p, and O 1s core levels were monitored as the samples were heated *in situ* to 550°K in the analyzer chamber of the XPS spectrometer. Only one core level was monitored as a function of time per sample. The vacuum inside the chamber during heating was better than 2×10^{-9} Torr. After the samples had reacted completely, they were cooled to 298°K to allow for extended data accumulation on the final product.

After XPS analysis, the final oxygen distribution for each of the three implant dosages was measured by the $^{16}O(d,\alpha)^{14}N$ nuclear reaction[4] with the d^+ beam incident at 60° to the sample normal and the detector angle at 164°. The cross-sections reported by Kim et al.[5] were used to calculate the oxygen concentration.

The composition of the reaction product was determined using 2.0 MeV $^4He^+$ backscattering. The He beam was incident at 5^o to the sample normal with a detector angle of 170^o.

C. RESULTS AND DISCUSSION

The dynamic technique developed in Chapter III for examining the Ni/silicide and Si/silicide interfaces can also be used to monitor the impurity content of the Ni film during the *in situ* growth of the silicide. As before, these experiments take advantage of the effective observation depth established by the exponential attenuation of photoemission signals in solids. By monitoring the core level signals from the carbon and oxygen impurities as well as the silicon and nickel as the sample is heated *in situ*, one can follow the progression of the impurity atoms as the interfacial region advances into the observation depth. In the experiments reported here the effect of impurities at the Ni/Ni_2Si interface is examined. Oxygen contamination is introduced into the Ni film in a controlled fashion using ion implantation.

Three oxygen implant dosages were studied. These correspond to peak intensities in the oxygen distribution of 1, 2, and 3 atomic percent of the Ni matrix. Figure 4 shows the progression of the O 1s signal for each of these dosages as a function of time during *in situ* silicide formation. An unimplanted control sample is shown for comparison. This as-deposited sample is representative of the amount of oxygen normally present in the Ni film as a result of oxygen

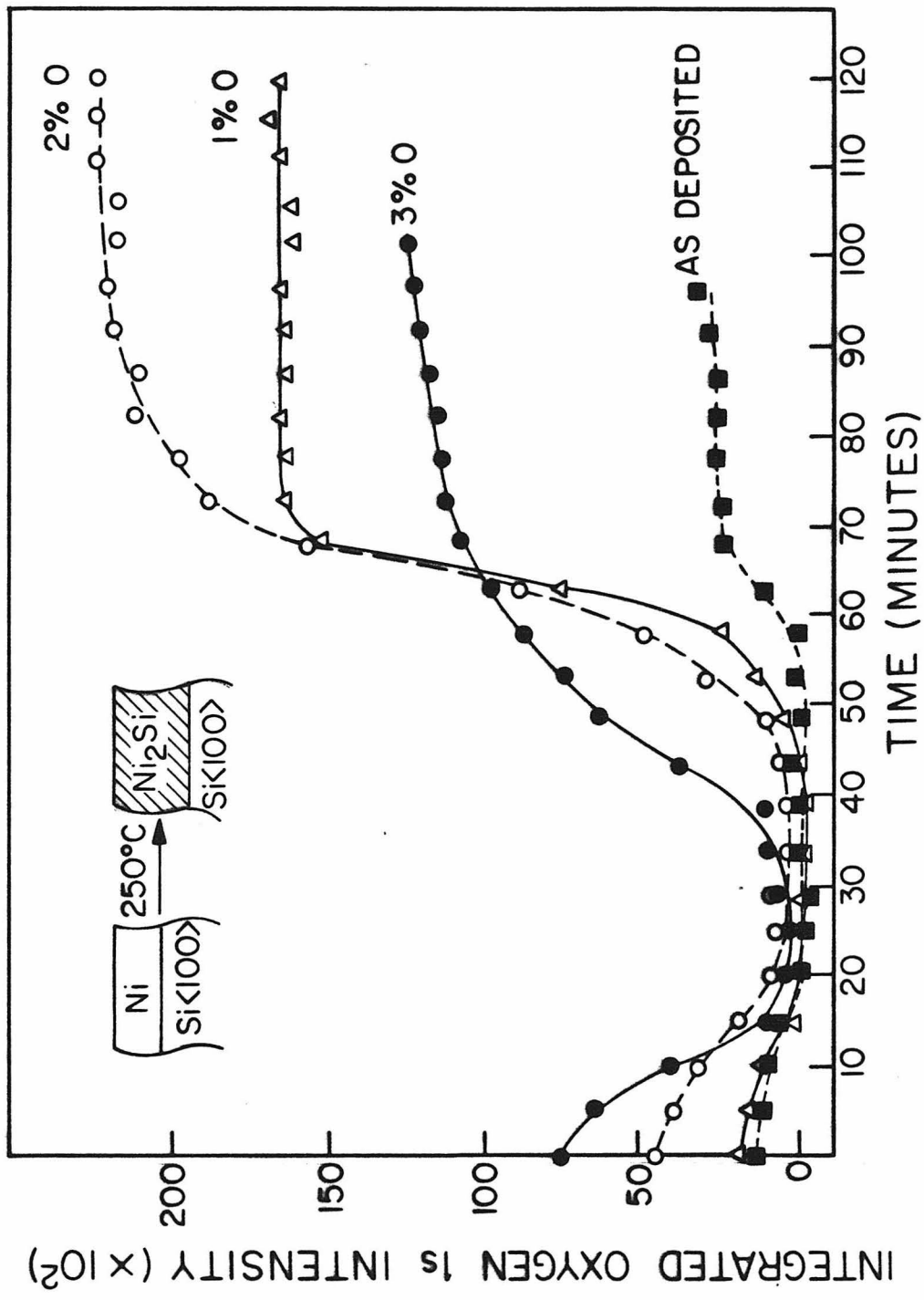

Figure 4: Plot of the oxygen 1s XPS spectral intensity as a function of time for various implant dosages.

contamination during the evaporation of the thin Ni film at 10^{-7} Torr. All four samples display an initial O 1s signal that decreases in intensity as the sample is heated. A finite amount of time is required for the sample to reach 550^{o}K. The O 1s intensity has fallen to essentially zero in all cases after heating for twenty minutes, which corresponds to a sample temperature of $\sim 480^{o}$K. We attribute this initial loss of oxygen signal to the desorbtion of oxygen containing contamination present on the sample surface after the cleaning procedure. It is interesting that the amount of overlayer contamination increases with the implant dosage. This may be related to an increase in the surface damage or defects as the dosage increases. As time progresses and the Ni/Ni_2Si interface begins to advance toward the sample surface, the observed O 1s intensity increases rapidly. The onset of the increase in the impurity signal begins at $\sim$ 35 minutes in the 3% implant. This is followed by the onset of the 2%, 1%, and as-deposited cases at 45, 50 and 60 minutes, respectively. The O 1s intensities eventually reach a maximum and remain constant throughout the remainder of the experiment. The maximum O 1s intensity obtained decreases in the order 2% > 1% > 3% > as-deposited. We attribute the apparent anomaly of the 3% O 1s maximum to the formation of a diffusion barrier as discussed in Reference 3. In such a situation, the advance of the Ni/Ni_2Si interface is impeded by the formation of a barrier which prevents the diffusion of the Ni metal necessary to maintain the solid phase reaction. On the time scale of the experiment, the Ni metal overlayer in the 3% case has not been consumed and it thus attenuates the signal from the oxygen that has accumulated at the Ni/Ni_2Si interface.

The final oxygen distributions for the samples used in the above experiments are shown in Figure 5. These distributions were obtained using the $^{16}O(d,\alpha)^{14}N$ nuclear reaction. In this technique, a profile of oxygen is obtained from analysis of the energy distribution of α particles produced by the low energy bombardment of deuterons on the sample. The depth of the oxygen atoms is deduced from the fact that the observed energy of an α particle produced at some depth x depends on the energy loss suffered by the deuterons on reaching depth x and the energy loss of the subsequent α particle in traversing the sample before reaching the detector.[6] The initial oxygen distribution before any reaction has occurred is shown by the dashed line in Figure 5. After the samples were annealed *in situ* in the XPS spectrometer the oxygen distributions indicated by the dotted curves were obtained. In each of the three cases, the oxygen has accumulated just below the sample surface. The concentration of oxygen calculated from these curves for the 1%, 2%, and 3% implant cases is 1.53×10^{16} cm^{-2}, 2.35×10^{16} cm^{-2}, and 2.96×10^{16} cm^{-2} ^{16}O, respectively. When compared to the original implant dosages, this corresponds to an increase in the oxygen concentration of 7.7×10^{15} cm^{-2}, 8.1×10^{15} cm^{-2}, and 6.2×10^{15} cm^{-2}, respectively. Because the samples were annealed in a background pressure of $\sim 2 \times 10^{-9}$ Torr, it is unlikely that the additional oxygen was introduced during the anneal step. We attribute the excess oxygen to oxidation of the sample surface that occurred during transport between the XPS experiment and the nuclear reaction measurements. The profiles in Figure 5 are markedly different from the profiles obtained by Scott on 2% implant samples annealed in a vacuum furnace with a background

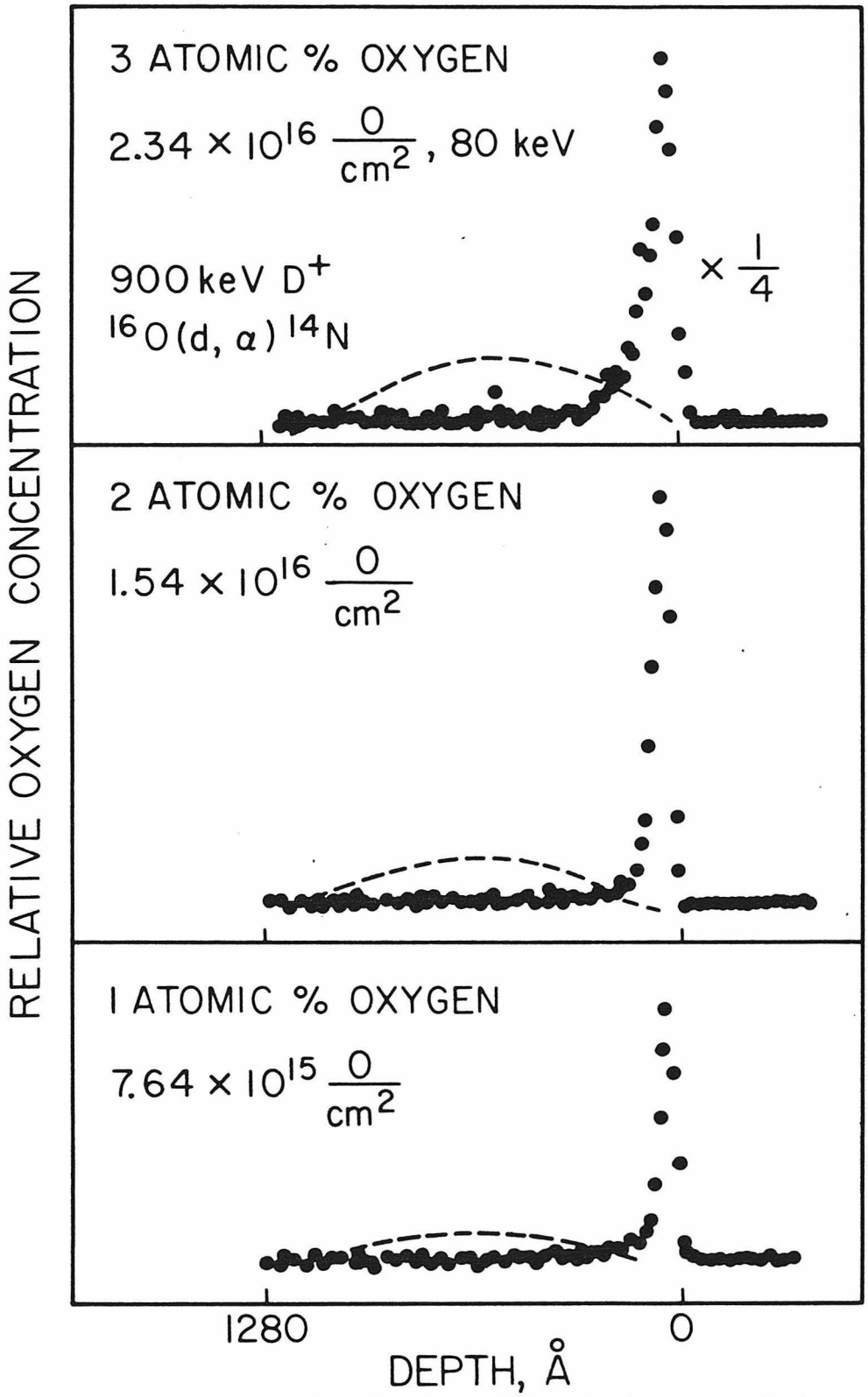

Figure 5: Nuclear reaction depth profile of the oxygen before and after silicide growth for various implant dosages.

pressure of $\sim 5 \times 10^{-7}$ Torr. Under his experimental conditions, he obtains a broad oxygen profile extending ~ 600 Å into the sample with a maximum oxygen concentration occurring at ~ 250 Å depth. He reports the Ni/Ni_2Si reaction front is stopped ~ 350 Å from the sample surface by the oxygen diffusion barrier. In contrast, we find that the 2% implant sample annealed at 2×10^{-9} Torr has entirely consumed the Ni metal overlayer and no diffusion barrier is evident. We attribute the difference between the two experiments to additional oxygen introduced from the ambient during the anneal step in the lower vacuum of the furnace. This will be discussed further in a later section.

Once it has been established that the progression of the photoemission signals from the oxygen reflects the accumulation of oxygen at the Ni/Ni_2Si interface, the question of the chemical state of the oxygen can be addressed. Several possibilities exist: (1) the oxygen is bound in the Ni metal lattice in either substitutional or interstitial sites, (2) the oxygen is bound to the silicon atoms present at the Ni/Ni_2Si interface, or (3) the oxygen is present as a mixed compound such as nickel silicate, Ni_2SiO_4. To distinguish between the above possibilities, the Ni and Si core level signals were monitored as the Ni/Ni_2Si reaction front advanced into the observation depth of the spectroscopy. Figure 6 shows the final Si 2p spectra obtained as a function of the different ^{16}O implant dosages. In the 1%, 2%, and 3% oxygen implanted samples a large SiO_2 peak is observed on the high binding energy side of the Si 2p line from the Ni silicide. In the unimplanted sample, a broad peak of low intensity is present upfield

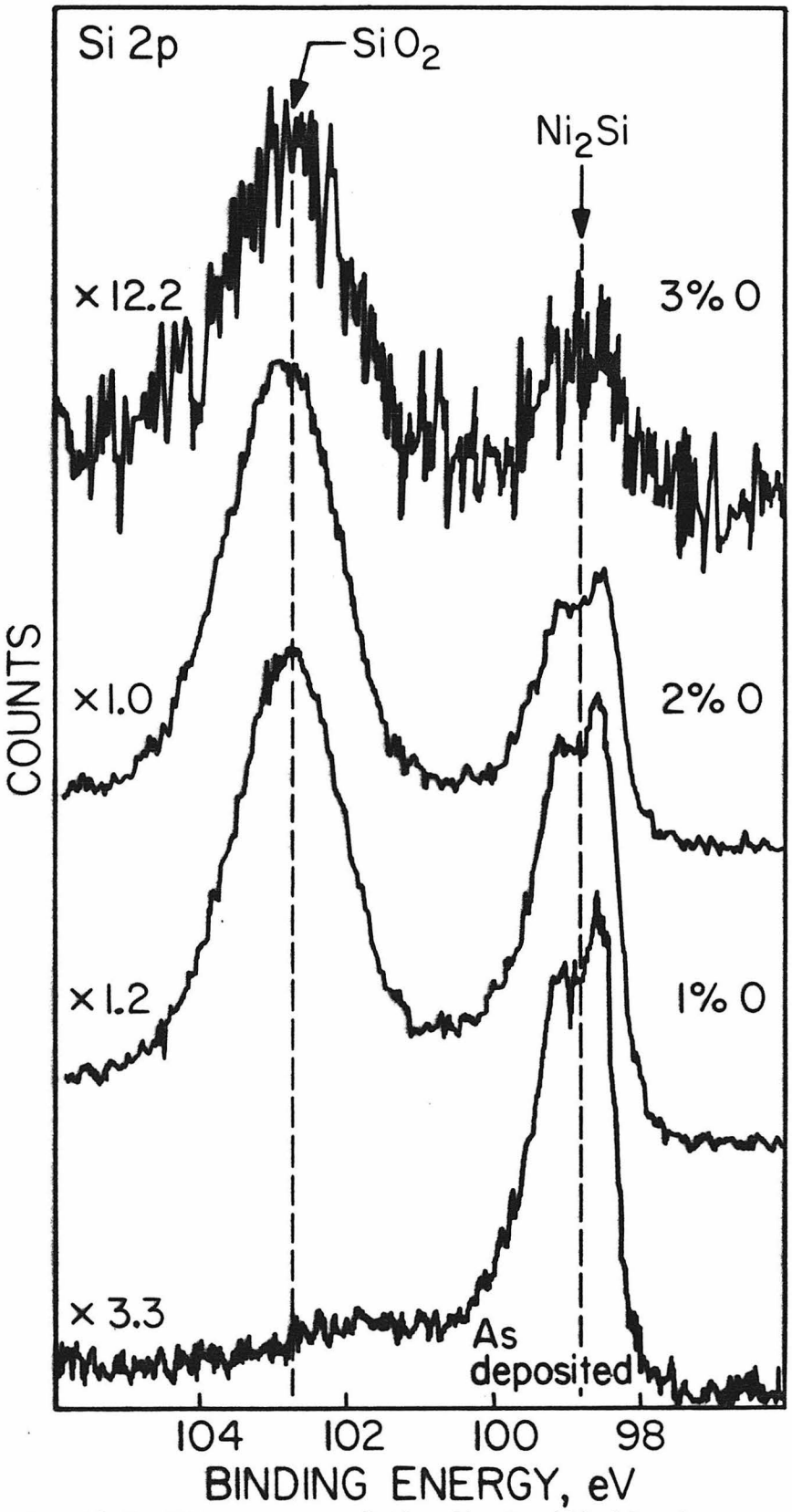

Figure 6: Si 2p XPS spectra of the final silicide phase corresponding to various oxygen implant dosages.

of the substrate signal. Its position indicates the presence of Si^{+3} and Si^{+2} suboxides Si_2O_3 and SiO.[7] The relatively weak intensity of the Si 2p signal observed for the 3% implanted sample provides further evidence that the reaction front in this case has stopped before reaching the sample surface. The Ni/Ni_2Si interface must be within 50-100 Å of the surface in order for the Si 2p signal from the silicide to be detected by XPS. The ratio of the Si 2p oxide to Si 2p silicide integrated intensity is plotted in Figure 7. There is a clear relationship between the amount of oxygen present in the Ni film before the reaction and the amount of SiO_2 observed after the reaction has been allowed to go to completion. Assuming the SiO_2 is present as a uniform layer above the silicide substrate, the ratio of the Si 2p oxide intensity, I_{ox}, to the Si 2p silicide intensity, I_{sil}, can be used to estimate the thickness x of the SiO_2 using the relationship

$$\frac{I_{ox}}{I_{sil}} = \frac{D_{ox}^{si}\,\lambda_{ox}}{D_{sil}^{si}\,\lambda_{sil}} \left(e^{x/(\lambda_{ox}\sin\theta)} + 1\right) \qquad \text{V-1}$$

where D_{ox}^{si} and D_{sil}^{si} are the atomic densities of Si in the oxide and silicide, respectively; λ_{ox} and λ_{sil} are the electron escape depths in the oxide and silicide, respectively; and θ is the angle between the plane of the sample and the detector. If we allow λ_{ox} to be 36 Å [8] and assume a "metallic-like" escape depth of 15 Å [9] for λ_{sil}, we calculate that the intensity ratios obtained for the unimplanted and the 1%, 2%, and 3% oxygen implanted samples correspond to 3.5 Å, 14.5 Å, 17.4 Å, and 24.0 Å of SiO_2, respectively.

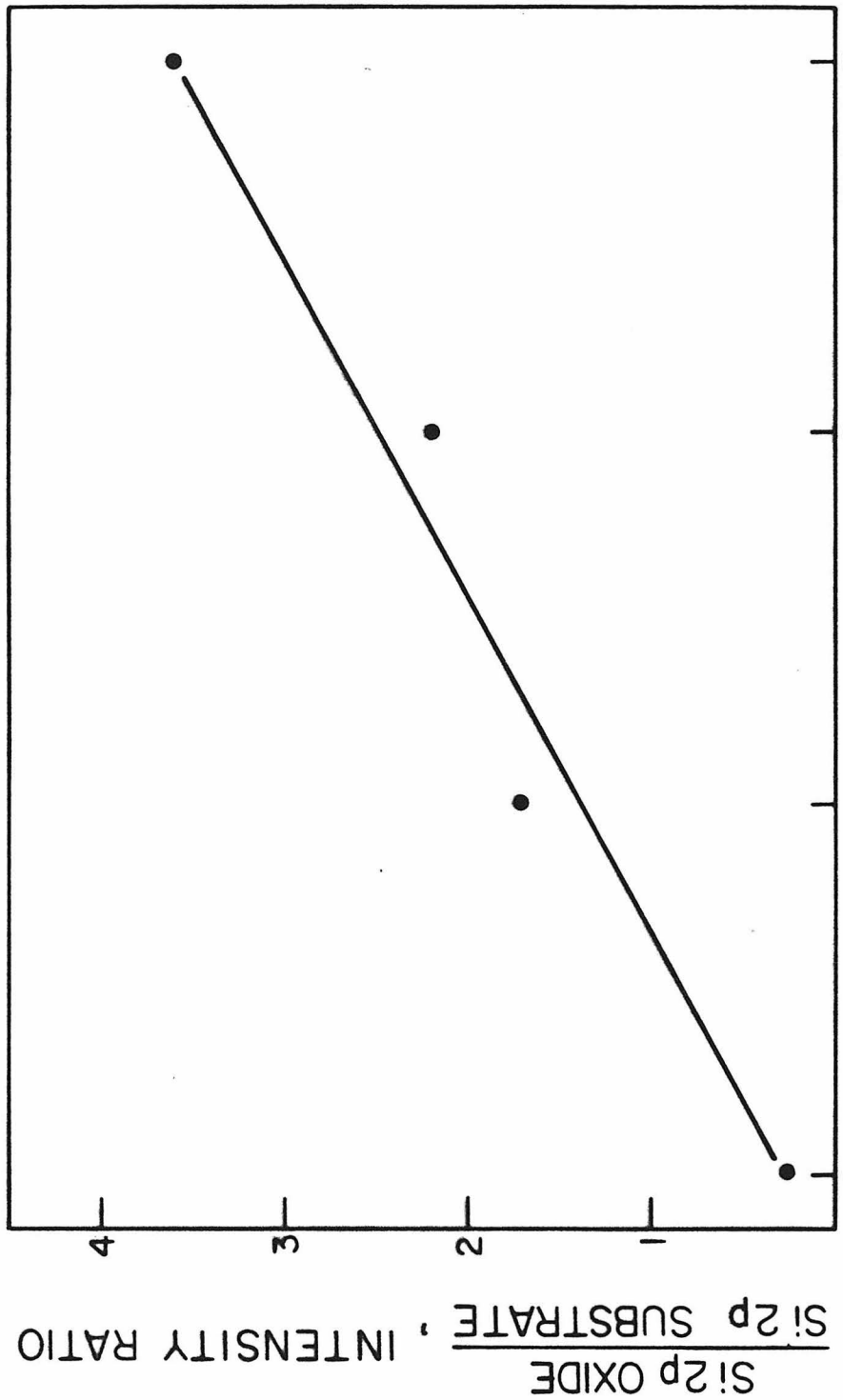

Figure 7: Plot of the Si 2p oxide/substrate ratios for the spectra given in figure 6.

The Ni $2p_{3/2}$ spectra corresponding to the Si 2p spectra in Figure 7 are plotted in Figure 8. In the as-deposited and 2% implant sample the final reaction product is observed to be Ni_2Si. In the 1% implant case, the Ni 2p is slightly higher in binding energy, indicating the reaction has been allowed to continue to the NiSi phase. In the 3% implant, only a Ni metal signal is observed. This is consistent with two features noted in previous figures: (1) the low intensity of the 0 1s profile for the 3% implant in Figure 4 indicates the oxygen signal is attenuated by the presence of an overlayer and (2) the relatively low intensity of the Si 2p signal for the 3% implant in Figure 6 indicates that both the silicide and the silicon dioxide are attenuated by an overlayer. These observations indicate a barrier preventing the diffusion of Ni metal has been formed in the 3% implant sample. The Ni/Ni_2Si interface has stopped 50-100 Å from the sample surface. No such diffusion barrier is observed in the 1% or 2% implanted samples.

To further elucidate the nature of the resulting thin films after reaction with 1%, 2% and 3% implanted oxygen, $^4He^+$ backscattering was used. Figure 9 plots the spectra obtained for the 1% and 2% samples. The spectra for the 3% sample is not shown, since it is identical to that obtained for the 2% case. The combination of XPS and RBS allows the observation of several interesting features. XPS is a surface sensitive technique and its sensitivity is limited to the top 100 Å of the sample. RBS, on the other hand, has a depth resolution of 100-200 Å as used here and is not sensitive to thin layers of material.

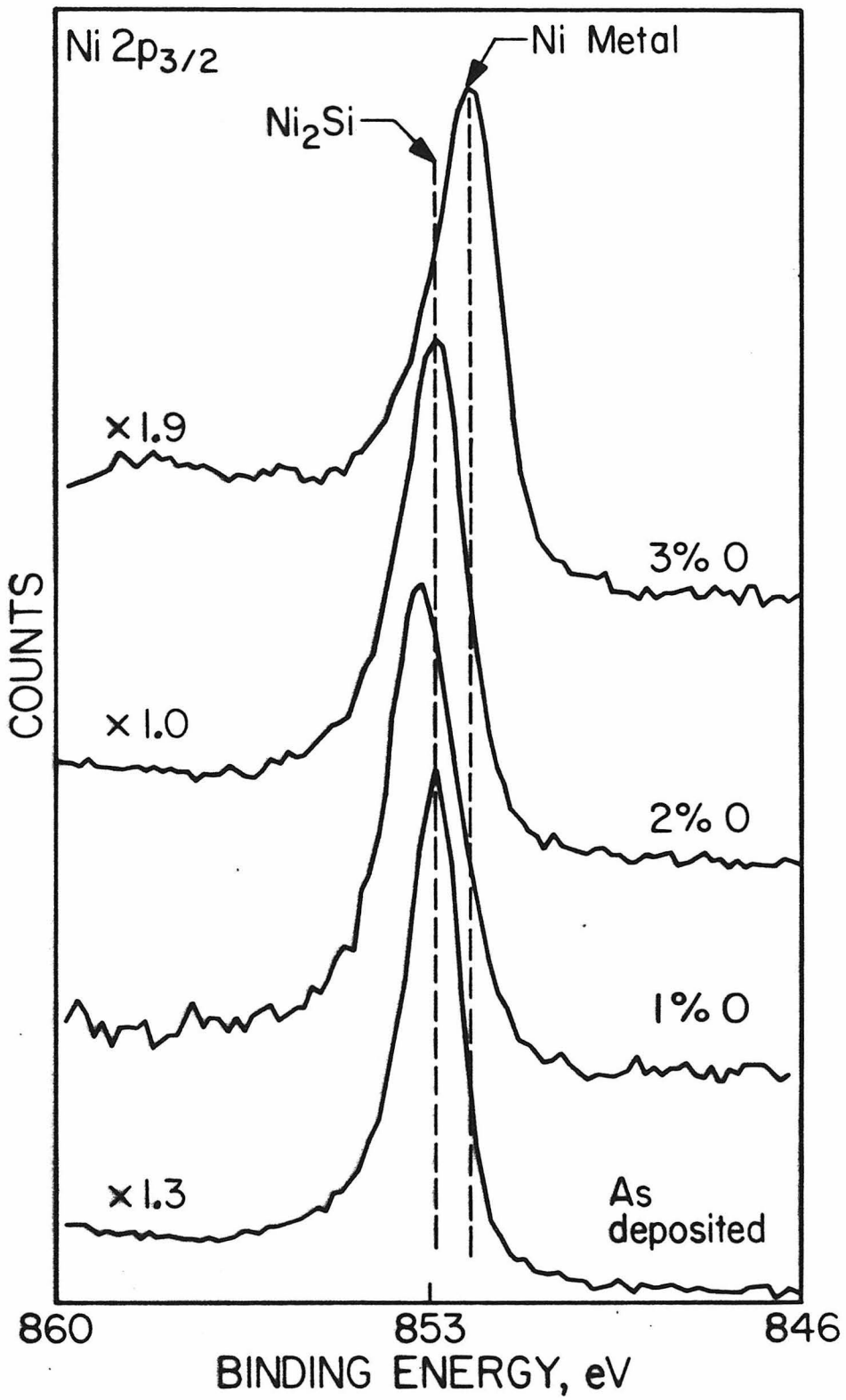

Figure 8: The Ni $2p_{3/2}$ XPS spectra of the final silicide phase obtained for various oxygen implant dosages.

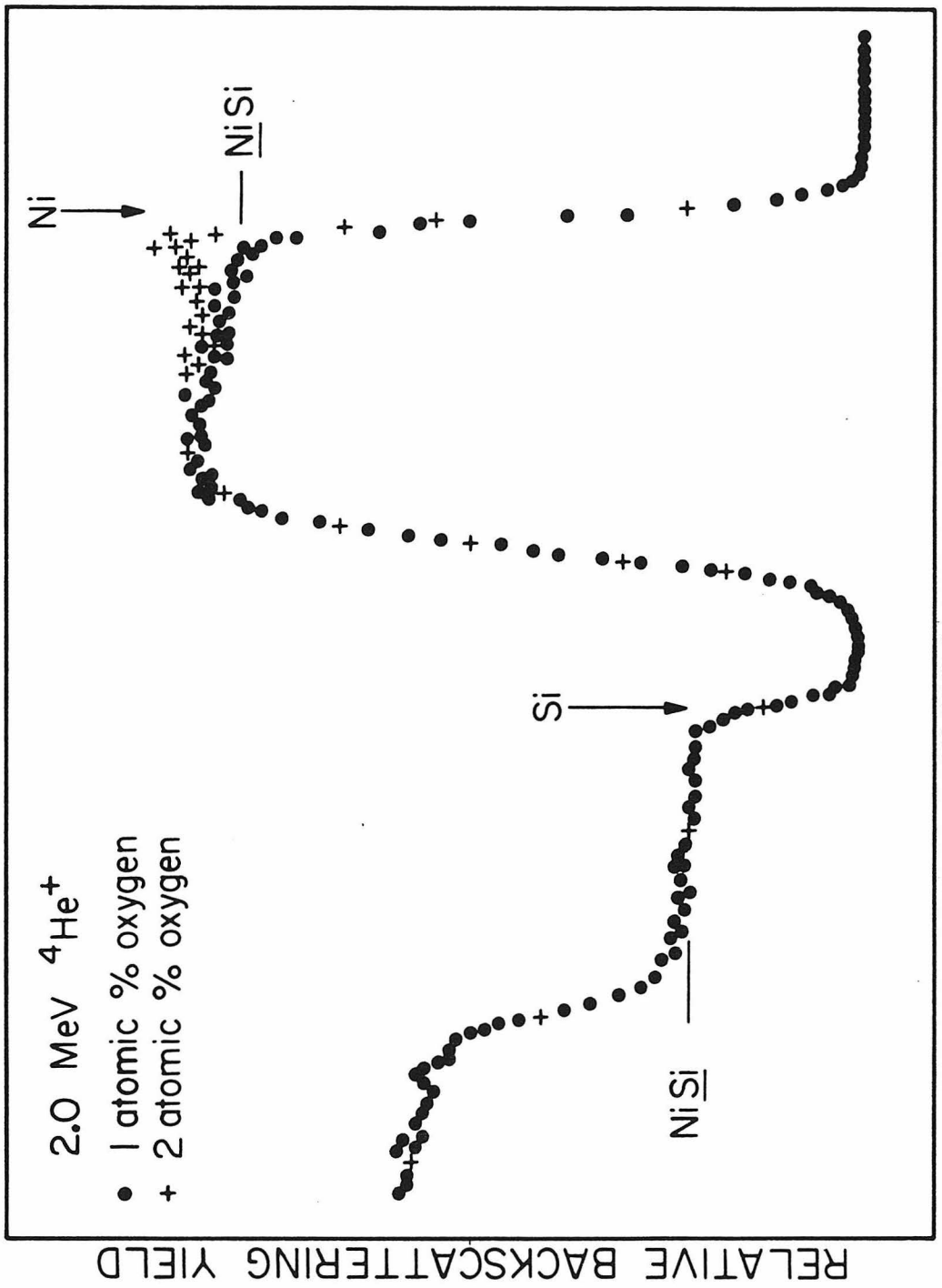

Figure 9: $^4He^+$ backscattered spectra obtained for the final silicide phase for the 1% and 2% oxygen implant dosages.

The utility of the backscattering technique lies in its ability to determine the atomic composition in the bulk of the solid. The backscattered spectrum in Figure 9 for the 1% implant indicates the thin film reaction produced the first phase Ni_2Si and then continued to entirely consume this phase to produce the second phase NiSi. This agrees with the observed Ni 2p peak in Figure 8 for the 1% implant which indicates NiSi is present on the sample surface. For the 2% case, the backscattered spectrum (Figure 9) again indicates the reaction has proceeded to the second phase NiSi. However, there is the additional presence of a small peak at the surface of the sample as indicated by the deviation from the curve obtained for the 1% implant. This peak is resolution limited and one is unable to determine the amount of Ni present in this region. The XPS spectrum obtained for the 2% implant (Figure 8) indicates the sample surface consists of the first phase compound Ni_2Si. This suggests that the oxygen that had accumulated at the Ni/Ni_2Si interface was insufficient to block the complete formation of the Ni_2Si, but that it was sufficient to prevent the NiSi reaction from completely consuming the Ni_2Si. This is the first evidence for the blockage of the second phase silicide formation by an impurity barrier. Finally, in the 3% implanted sample, a backscattered spectrum identical to that found for the 2% case is obtained. The XPS spectra in Figure 8 indicate that in this case, however, the species present on the sample surface is Ni metal. The oxygen impurity level was sufficiently high that it blocked the diffusion of the Ni metal and thus prevented the Ni/Ni_2Si interface from reaching any closer than 50-100 $\mathring{A}$ of the sample surface. Once the Ni

diffusion was blocked, the second phase NiSi began to form at the Si/Ni_2Si interface. This phase proceeded to consume the Ni_2Si until it too was within 50-100 Å of the sample surface.

The above observations establish that the oxygen concentration becomes sufficiently high to form a diffusion barrier to Ni_2Si only in the 3% implanted sample. We can now understand why the results in these experiments differ from those reported previously.[3] In the 3% implant, a total of 2.34×10^{16} $^{16}O/cm^2$ was implanted. The implanted oxygen has a gaussian profile with a peak maximum at 640 Å and a standard deviation of 330 Å. Assuming the Ni/Ni_2Si interface was stopped $\sim$ 50 Å from the sample surface, as indicated by the XPS data, one can easily calculate the percent of the oxygen profile accumulated by the advancing interface. By integrating the gaussian distribution,[10] this is found to correspond to 94% of the implanted oxygen or 2.2×10^{16} O/cm^2. This represents the amount of oxygen necessary to produce the barrier against Ni diffusion. Under different annealing conditions, Scott reports that a 2% oxygen implant is able to stop the silicide reaction front $\sim$ 350 Å from the sample surface. He indicates, however, that the total oxygen content of the film increases during the course of the experiment from the original implant dosage of 1.6×10^{16} to 3.2×10^{16} O/cm^2, excluding the contribution from the surface oxide peak. This oxygen concentration already exceeds the amount of oxygen present after a 3% implant. Given that the Ni/Ni_2Si interface stops 350 Å from the sample surface, one can again calculate the percent of the gaussian oxygen profile that must have accumulated as the interface advanced.

With a peak maximum at 640 Å and a σ of 330 Å, this corresponds to 81% of the oxygen profile being swept by the advancing Ni/Ni_2Si interface or 1.30×10^{16} O/cm^2. The difference between this value and the amount of oxygen determined to be required for formation of the barrier from the UHV experiments represents the amount of oxygen that must have been introduced from the background ambient during the anneal step in the lower vacuum. This excess oxygen contamination corresponds to 9.0×10^{15} O/cm^2. It is not unreasonable to assume this amount of oxygen could be introduced into the Ni film via grain boundary diffusion at an elevated temperature with a 10^{-7} Torr background pressure. If we take from the UHV experiments that 2.2×10^{16} O/cm^2 are required to produce the Ni diffusion barrier and assume that it is all present as SiO_2, one can estimate the thickness of SiO_2 required to stop the diffusion of Ni. If the density of SiO_2 is taken to be 2.32×10^{22} molecules/cm^3, this thickness corresponds to $\sim$ 45 Å. This estimate is higher than the 24 Å SiO_2 layer calculated previously from the Si oxide/Si substrate ratios in Figure 6. The difference in the estimates from the two techniques may be attributed to interfacial roughness. It has been reported by Crider and Poate[1] that increasing O_2 contamination in in Pt films on Si leads to increasingly irregular surfaces and interfaces in the silicide.

The XPS data have thus far suggested that the formation of SiO_2 is responsible for the barrier against Ni metal diffusion. The possibility that Ni oxide is participating in the barrier can be excluded by examination of Figure 8. The compound NiO falls at a binding energy of 854.0 eV.

No structure is observed at this energy in the final Ni 2p spectra plotted in Figure 8. The presence of the mixed compound Ni_2SiO_4 has been reported by Schaffer, et al.[11] They suggest the nickel silicate segregates at grain boundaries and thus eliminates the diffusion of the Ni metal. If Ni_2SiO_4 is responsible for the barrier observed in the experiments reported here, an intense Ni 2p signal equivalent to the oxidized Si 2p signals in Figure 6 should be present at $\sim$ 856 eV in Figure 8.[12] Again, no peak structure is observed at this binding energy in the Ni 2p spectra. If such a mixed compound is present, it is below the detection limits of the spectroscopy and, as such, cannot account for the formation of the diffusion barrier.

If all the oxygen present in the film is bound as SiO_2, then the O 1s intensity should be completely accounted for by the Si 2p oxide intensity. In the lower curves of Figure 10, the Si 2p oxide and O 1s intensities are plotted as a function of time as the Ni/Ni_2Si interface advances toward the sample surface. The initial decrease in the O 1s signal is due to the desorbtion of oxygen containing impurities on the sample surface as the temperature increases. During the first 45 minutes of the *in situ* reaction, no O or Si signal is detected. After 45 minutes, the O 1s signal begins to increase rapidly followed by the Si 2p oxide signal after 53 minutes. After 70 minutes, both signals have attained their maximum intensity and remain constant for the remainder of the experiment. The observation that the O 1s signal begins to increase before the Si 2p oxide is significant. It cannot be accounted for by a difference in electron escape depths. The kinetic energy of the

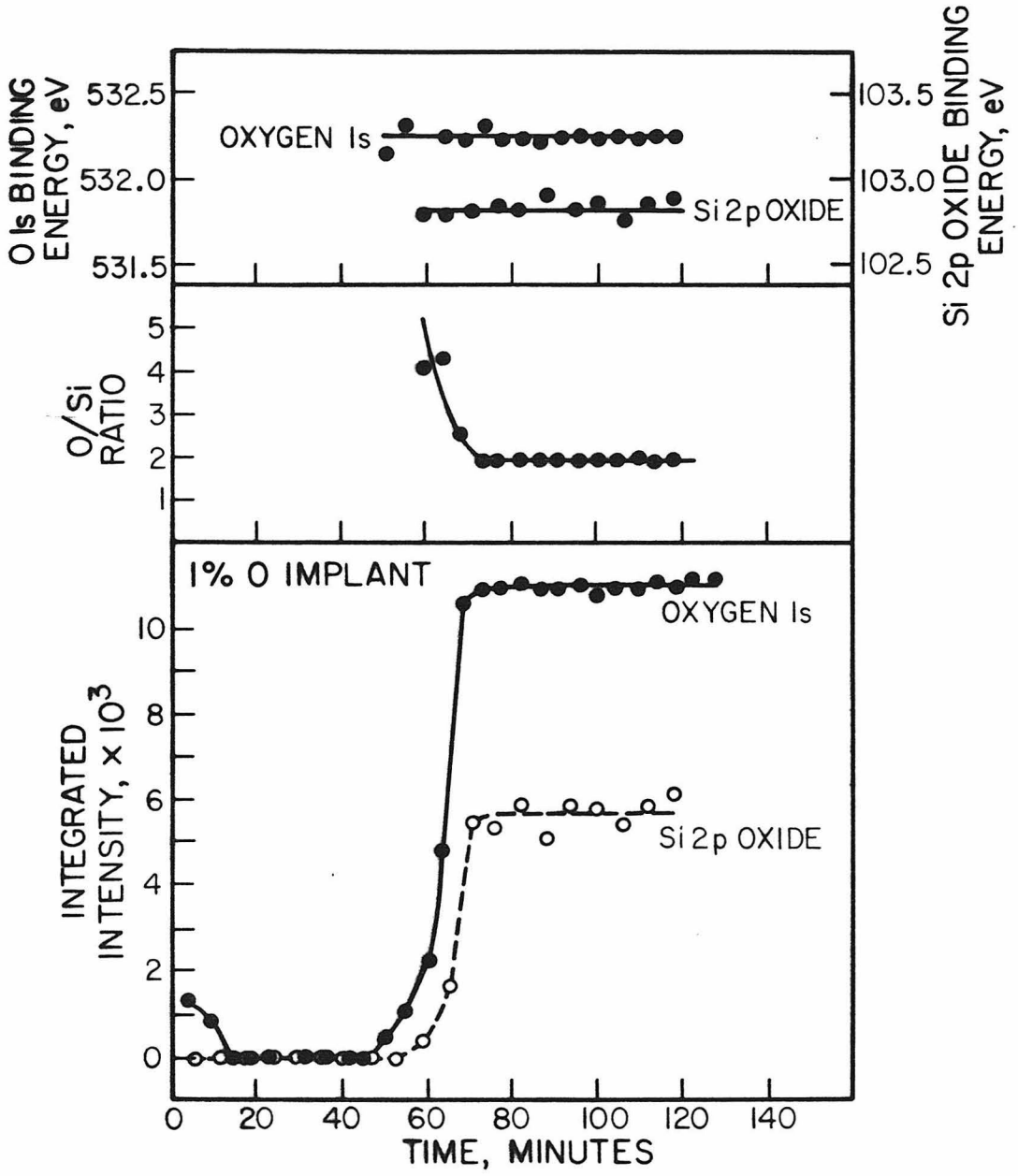

Figure 10: Composite curve giving the core line intensities, O/Si stoichiometries, and binding energy maxima as a function of time for the 1% oxygen implant dosage.

Si 2p photoelectron is greater than that of the O 1s photoelectron. On this basis alone, one would expect to observe the Si 2p signal before the O 1s. That the opposite occurs suggests there must be a front of oxygen preceding the SiO_2 layer. This is also indicated by the O/Si stoichiometry ratio plotted in the middle curve of Figure 10. A O/Si ratio of 2 indicates stoichiometric SiO_2. The experimentally measured O 1s/Si 2p intensity ratios were calibrated against a thick thermal SiO_2 oxide on Si. The use of a calibration standard allows the estimation of the stoichiometry because such unknown factors as the photoelectron cross-sections and electron escape depths are intrinsically included. In Figure 10, it can be seen that the initial onset of O 1s intensity corresponds to an O/Si ratio considerably greater than 2. This indicates that initially more oxygen is present than can be accounted for by SiO_2. When the O 1s and Si 2p signals have attained their maximum intensity, the O/Si ratio is 2. At the end of the reaction all oxygen can be accounted for by the formation of SiO_2. No additional oxygen is present in other chemical species. The upper curves in Figure 10 plot the O 1s and Si 2p oxide binding energies as the interface advances. Both the O and Si signals remain constant at 532.3 and 102.9 eV, respectively.

The O 1s and Si 2p oxide intensities for the 2% implanted sample are plotted as a function of time in the lower curves of Figure 11. Qualitatively, the curves are similar to those obtained with the 1% sample. The O 1s signal is observable after $\sim$ 45 minutes, while the Si 2p oxide line first appears after $\sim$ 55 minutes. This suggests there

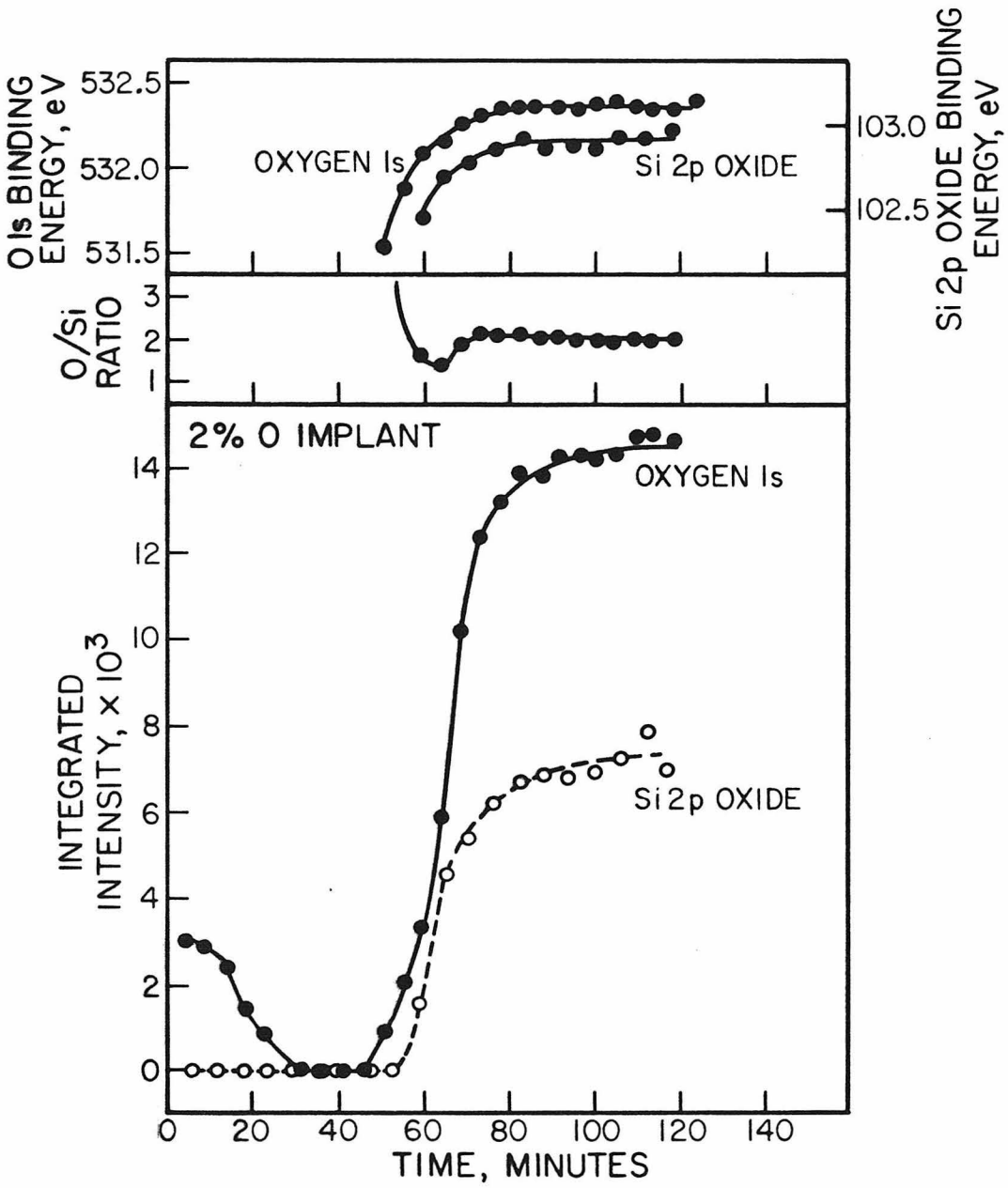

Figure 11: Composite curve giving the core line intensities, O/Si stoichiometries, and binding energy maxima as a function of time for the 2% oxygen implant dosage.

is an oxygen front prior to the SiO_2 as in the 1% implant. The O/Si ratio is greater than 2 in this region. After $\sim$ 90 minutes, the O and Si intensities reach a plateau. At this point, the O/Si ratio is 2, indicating the presence of SiO_2 with no excess oxygen. The dip in the O/Si curve indicates the presence of silicon suboxides in front of the SiO_2 region. The O ls and Si 2p oxide binding energies in the upper curves show a gradual shift from low to high binding energies as the initial signals appear. This further indicates that at least some of the excess oxygen in this region is bound as a Si suboxide such as those noted previously in the as-deposited sample. The striking difference between the 2% and 1% sample is that the increase of the Si 2p oxide and O ls intensities to their plateau is considerably more gradual in the 2% implant. This indicates that although no barrier to Ni diffusion has formed, the reaction rate has decreased. This is consistent with work reported by others on the effect of oxygen impurities on the growth kinetics of silicides.[1,3]

The decrease in the growth rate of nickel silicide is more dramatic in the 3% implanted sample as shown in the lower curves of Figure 12. In this case, 120 minutes are required for the O and Si signals to begin to reach their maximum intensities. As in the 1% and 2% samples, the early onset of the O ls intensity and the large O/Si ratio indicates a front of oxygen must precede the SiO_2 layer. The gradual upfield shift of the Si 2p oxide binding energy suggests the presence of Si suboxides preceding the stoichiometric SiO_2.

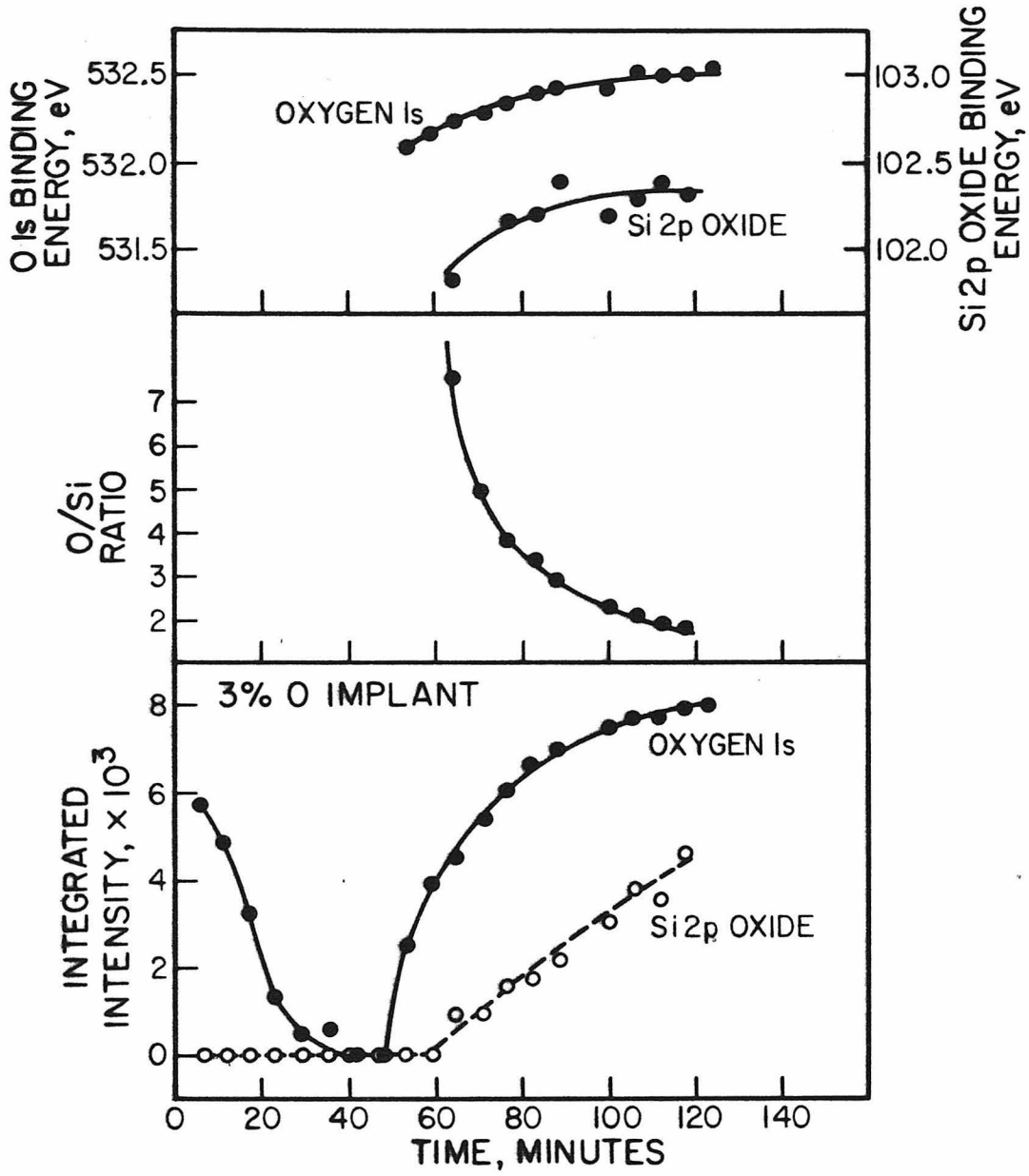

Figure 12: Composite curve giving the core line intensities, O/Si stoichiometries, and binding energy maxima as a function of time for the 3% oxygen implant dosage.

D. SUMMARY

In this chapter, the effect of implanted oxygen on the Ni/Ni_2Si interface is investigated using XPS, $^4He^+$ backscattering, and $^{16}O(d,\alpha)^{14}N$ nuclear reactions. Oxygen contamination was introduced into Ni films on <100> Si in a controlled fashion using ion implantation.

It is known from marker experiments that Ni is the moving species in the growth of Ni_2Si.[13-15] Several studies have demonstrated that impurities, particularly O_2, have a marked effect on the reaction kinetics and the phase growth sequence.[1-3, 16] This has been attributed to the formation of a Ni diffusion barrier at the Ni/silicide interface. In this chapter, the chemical nature of this barrier and its effect on the silicide interface has been examined.

The dynamic technique developed in Chapter III for the investigation of the Ni/silicide and Si/silicide interfacial regions is used to monitor the oxygen impurity content of the Ni film during *in situ* growth of the Ni silicide. Three oxygen implant dosages corresponding to peak concentrations of 1, 2, and 3 atomic percent ^{16}O were studied.

The O 1s intensity was monitored as a function of time as the implanted samples were heated *in situ* to $550^{\circ}K$. The maximum O 1s intensity attained by the samples decreased in the order 2% > 1% > 3% > unimplanted. The low intensity observed in the 3% case has been attributed to the formation of a Ni diffusion barrier which prevented the Ni/Ni_2Si interface from reaching the sample surface.

$^{16}O(d,\alpha)^{14}N$ nuclear reactions were used to obtain the final oxygen distribution profiles in each of the implanted samples. The profiles verified that the oxygen impurities had been swept forward of the Ni/silicide reaction front as indicated by the XPS data. It was determined that the amount of oxygen necessary to stop the Ni diffusion is 2.2×10^{16} O/cm^2.

The Ni 2p and Si 2p core level signals were examined after the reaction for each of the implanted samples to determine the chemical nature of the diffusion barrier. It was shown that neither Ni oxide or mixed compounds such as Ni_2SiO_4 were involved in the barrier formation. The amount of SiO_2 in the film was found to increase with the implant dosage. In the unimplanted sample, the oxygen contamination introduced during the Ni evaporation resulted in the presence of silicon suboxides Si_2O_3 and SiO at the Ni/silicide interface. In the 3% sample, both the Ni 2p and Si 2p spectra indicated the advance of the Ni/Ni_2Si interface had been stopped by the presence of a diffusion barrier. This strongly suggests SiO_2 is responsible for the Ni barrier.

Backscattering spectroscopy was used to further elucidate the nature of the thin films present after the solid phase reaction had gone to completion. In all three samples the final bulk reaction product was the second phase silicide NiSi. However, a resolution limited peak was observed on the surface of the 2% and 3% samples. The XPS spectra indicated the surface of the 2% sample consisted of Ni_2Si while the 3% sample surface was Ni metal. The combination of these techniques indicates the oxygen level in the 2% sample was not

sufficient to stop the Ni_2Si growth, but a barrier against the complete formation of the second phase NiSi did exist. In the 3% sample, the oxygen content is sufficiently high that the formation of the first phase Ni_2Si was inhibited.

Examination of the Si 2p oxide and O 1s intensity as a function of time during the *in situ* growth of the silicide allowed one to determine if the total oxygen content of the film was bound as SiO_2. It was found that a front of oxygen is present forward of the SiO_2 accumulating at the Ni/Ni_2Si interface. The presence of silicon suboxides at the SiO_2/Ni boundary was also indicated. It appears that as the advancing Ni/Ni_2Si interface encounters oxygen in the Ni film, silicon suboxides are formed. As more oxygen is encountered, Si takes on a full coordination of oxygen, forming SiO_2. When a sufficient layer of SiO_2 has formed, Ni metal is no longer able to diffuse through to the Si/Ni_2Si interface to continue to the solid phase reaction. This should occur independent of the mechanism of Ni diffusion (via grain boundary diffusion or excess lattice vacancies).

References

1) C. A. Crider, J. M. Poate, Appl. Phys. Lett., 36, 417, (1980)

2) J. B. Bindell, J. W. Colby, D. R. Wonsidler, J. M. Poate, D. K. Conley, T. C. Tisone, Thin Solid Films, 37, 441 (1976)

3) D. M. Scott, P. J. Grunthaner, B. Y. Tsaur, M-A. Nicolet, J. M. Mayer, paper presented at the 156th meeting of the Electrochemical Society, Los Angeles, 1979 (to be published in the Proceedings of the Symposium on Thin Film Interfaces and Interactions, 1980)

4) S. T. Pieraux, Nucl, Instr. Meth., 149, 289 (1978)

5) H. C. Kim, R. F. Seiler, D. F. Herring, K. W. Jones, Nucl. Phys., 57, 526 (1964)

6) A. Turos, L. Wielunski, A. Barcz, Nucl. Instr, and Methods, 111, 605 (1973)

7) F. J. Grunthaner, P. J. Grunthaner, R. P. Vasquez, B. F. Lewis, J. Maserjian, A. Madhukar, J. Vac. Sci. Technol., 16, 1443 (1979)

8) J. M. Hill, D. G. Royce, C. S. Fadley, L. F. Wagner, F. J. Grunthaner, Chem. Phys. Lett., 44, 225 (1976)

9) D. R. Penn, J. Electron Spectrosc. and Related Phenom., 9, 29 (1976)

10) P. R. Bevington, Data Reduction and Error Analysis for the Physical Sciences (McGraw-Hill, New York, 1969)

11) W. J. Schaffer, R. W. Bené, R. M. Walser, J. Vac. Sci. Technol., 15, 1325 (1978)

12) P. Lorenz, J. Finster, G. Wendt, J. V. Salyn, E. K. Zumadilov, V. I. Nefedov, J. Electron Spectrosc., 16, 167 (1979)

13) K. N. Tu, W. K. Chu, J. W. Mayer, Thin Solid Films, 25, 403 (1975)

14) W. K. Chu, S. S. Lau, J. W. Mayer, H. Müller, K. N. Tu, Thin Solid Films, 25, 393 (1975)

15) R. Pretorius, C. D. Ramiller, S. S. Lau, M-A. Nicolet, Appl. Phys. Lett., 30, 501 (1977)

16) R. J. Blattner, C. A. Evans, Jr., S. S. Lau, J. W. Mayer, B. M. Ullrich, J. Electrochem. Soc., 122, 1732 (1975)

CHAPTER VI

OTHER TRANSITION METAL/SILICON SYSTEMS

A. INTRODUCTION

In the previous chapters we have discussed the chemistry of the Ni/Ni_2Si and Si/Ni_2Si interfaces using a combination of XPS and RBS. In this discussion the dynamic experiments developed in Chapter III are extended to the Pt/Pt_2Si and Pd/Pd_2Si systems. The data presented are preliminary, but suggest a variety of interesting chemical differences as compared to the Ni system. Traditional inorganic chemistry has demonstrated that the 4d and 5d transition metals show similar bonding trends. The 3d metals often exhibit strikingly different chemistry in comparison. This examination of the Ni, Pt, and Pd systems offers the opportunity to examine the solid state chemistry of these elements in a homologous series of compounds.

B. EXPERIMENTAL

Crystalline Si <100> (n type, 1-10 Ω-cm) wafers were used as the substrates for the deposition of thin Pt and Pd films. The substrate was cleaned ultrasonically with TCE, acetone, and methanol and rinsed with deionized water. Just prior to evaporation, the wafers were etched with dilute HF, rinsed with deionized water, and blown dry with N_2. Approximately 500 $\mathring{A}$ of Pt or Pd were e-beam evaporated onto the clean substrates with a background of $\sim 5 \times 10^{7}$ Torr.

Prior to examination of the samples with XPS, the Pd and Pt surface oxides that had formed during sample transport were removed by etching. The Pd oxide was removed by spinning a 3/8 x 3/8 inch sample at 3600 rpm and adding dropwise 500 µl of 1:1 HCl in ethanol, followed by 500 µl acetone, and finally 1000 µl ethanol. The HCl etch removed any native Pd oxides that had formed while the acetone served to dissolve any $PdCl_2$ residues. The oxygen KLL Auger line at ∿ 970 eV was used to monitor the oxygen contamination since the O 1s core line overlaps the intense Pd $3p_{3/2}$ line. The Pd 3d doublet before and after the initial etches is shown in Figure 1. In the upper plot, the presence of PdO_2 is indicated by the small peak at ∿ 337.8 eV.[1] The slight shift in the Pd $3d_{5/2}$ peak maximum relative to the signal from the clean substrate in the lower curve also indicates the presence of the lower oxide PdO at ∿ 336.2 eV.[1] The initial presence of PdO is further substantiated by the decrease in the FWHM of the Pd $3d_{5/2}$ line from 1.8 eV to 1.6 eV after etching. The lower curve in Figure 1 indicates that after the clean, no observable PdO_2 or PdO remains. The oxygen Auger line is not detectable and the only remaining contamination is a small carbon overlayer (< 1 monolayer). The Pt/<100> Si sample was cleaned using the same spinning technique described above. A 3/8 x 3/8 inch sample was etched with 500 µl of 1:1 HCl in ethanol followed by 500 µl ethanol. The Pt $4d_{5/2}$ spectrum before the clean did not indicate the presence of PtO or PtO_2 and the observed line shape remained unchanged after the etch. The oxygen 1s intensity did, however, decrease substantially. The small amount of oxygen contamination that did remain was found to desorb upon heating of the sample for the *in situ* growth experiments.

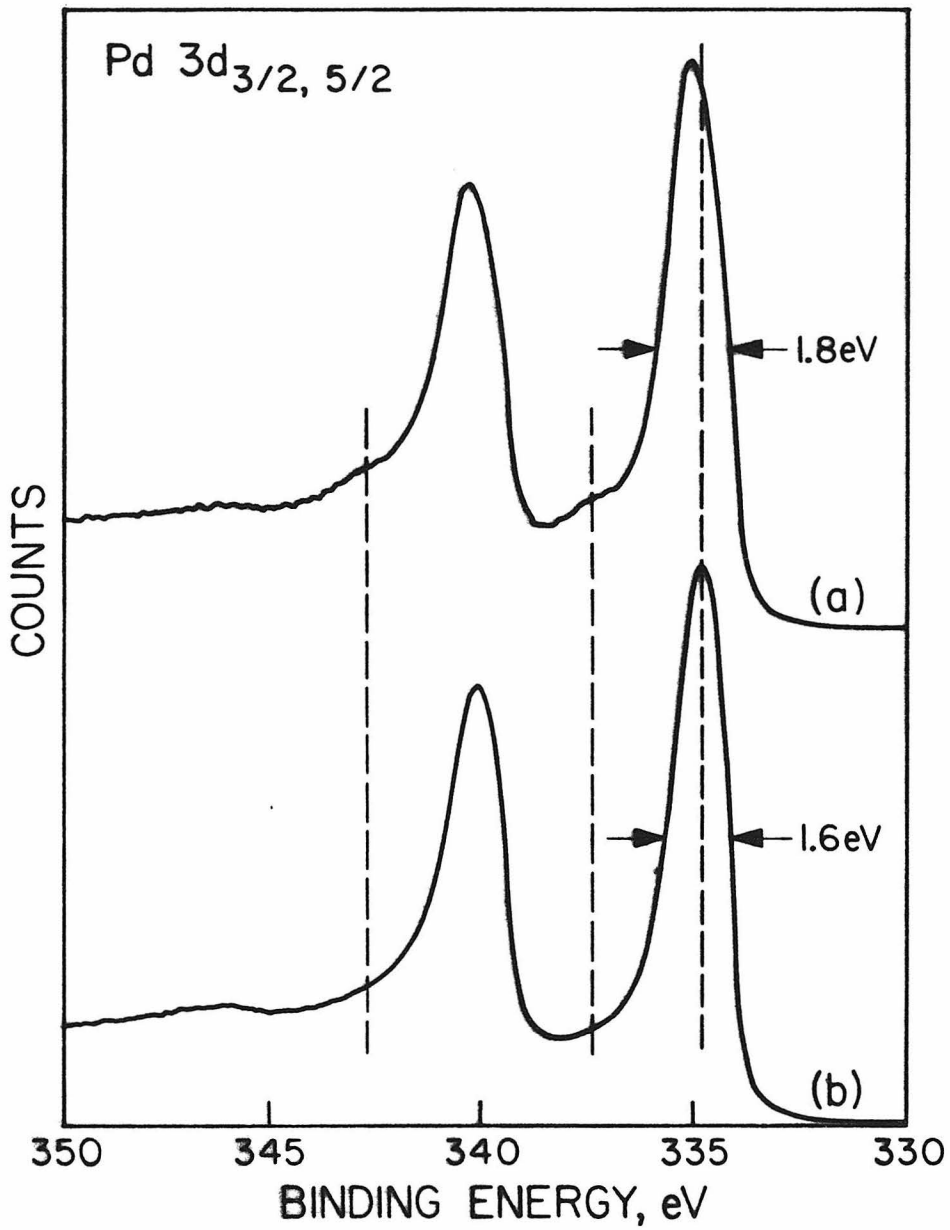

Figure 1: The Pd 3d doublet before and after removal of the surface oxide overlayer.

A small amount of carbon (< 1 monolayer) also remained after the etching procedure. The entire etching procedure for both the Pt and Pd samples was performed in a drybox under a flowing N_2 atmosphere. Since the sample inlet port of the spectrometer is connected directly to the N_2 drybox, no further oxidation of the samples occurred.

After establishing sample surfaces that were essentially free of oxide and carbon overlayers, the samples were heated *in situ* in the analyzer chamber of the XPS spectrometer. During heating, the chamber vacuum was $\sim 2 \times 10^{-9}$ Torr. The Pt/<100> Si and Pd/<100> Si samples were heated to 250°C and 170°C, respectively. At various intervals, the samples were cooled to 25°C to allow for extended data accumulation periods.

C. RESULTS AND DISCUSSION

1. The Pd/Pd_2 Si Interface

The Pd/Pd_2 Si interface may be studied by monitoring a sample of Pd deposited on Si <100> during the *in situ* formation of Pd_2Si. As demonstrated in Chapter III for Ni/Ni_2Si, the core level signals from the emerging Si atoms may be used to interrogate the Pd/Pd_2Si interface. The upper plot in Figure 2 shows a broad energy spectrum of 1280 eV obtained from a bulk Pd_2Si specimen. The major Pd and Si photoelectron and Auger lines are labeled according to their level of origin. The carbon peak at 285 eV is due to an overlayer of carbon containing contaminants. The intense Pd 3d doublet at $\sim$ 340 eV and the Si 2p line at $\sim$ 100 eV were monitored in detail as a function of time to determine

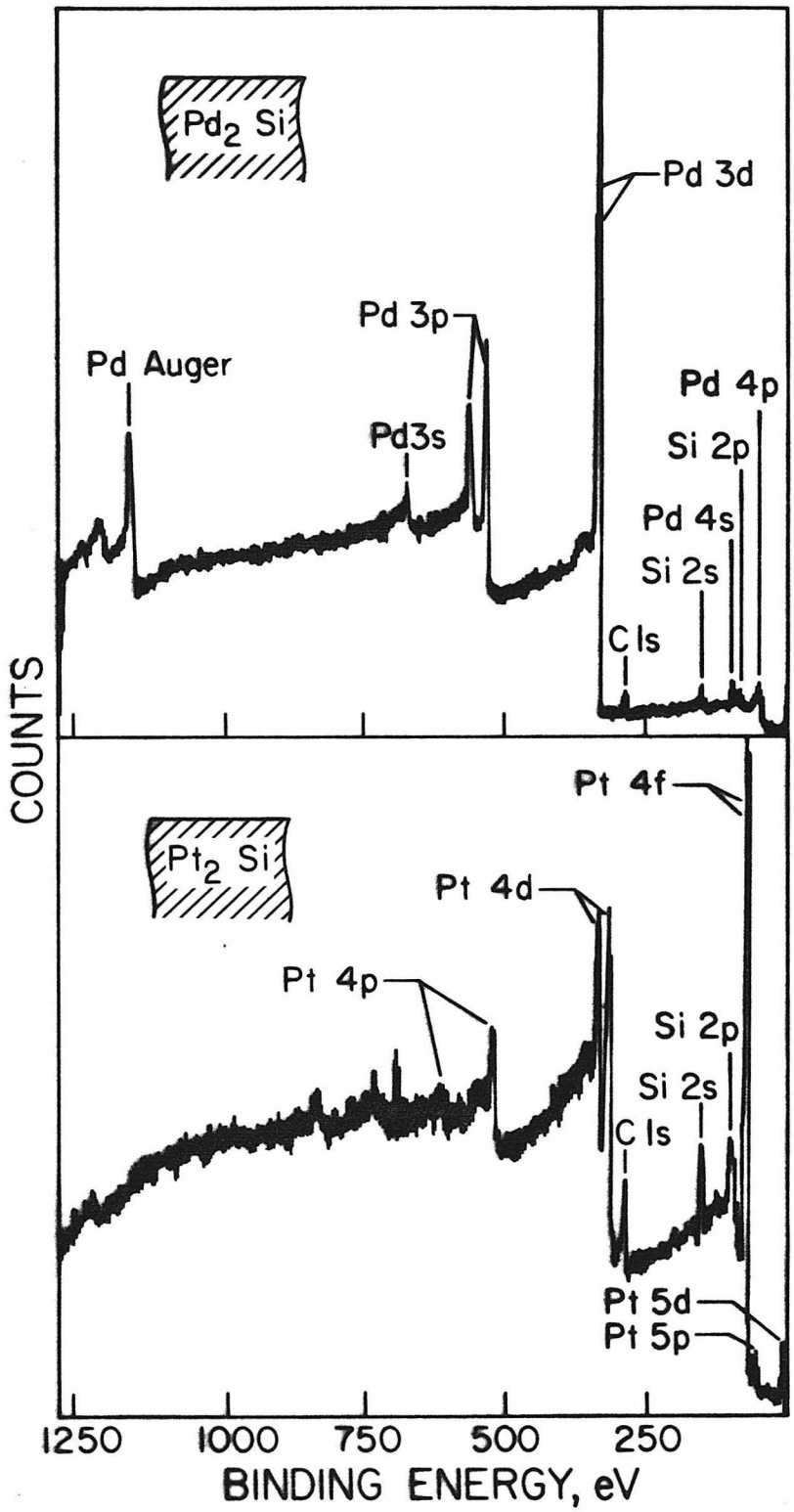

Figure 2: Wide scan XPS spectra of Pd_2Si and Pt_2Si samples.

the relative shifts between the Pd/Pd_2Si interfacial region and the bulk Pd_2Si.

Figure 3 plots the progression of the Pd 3d doublet as a function of time during the *in situ* silicide growth. Figure 3a corresponds to the pure Pd metal signal while Figures 3b-3g represent the progression toward the end phase Pd_2Si. The spectrum in Figure 3g is believed to be that of Pd_2Si since no further change in either the Pd or Si signal occurs at this time. In addition, the high formation temperature of 700°C[3] for the second phase PdSi suggests it is unlikely that this sample could have progressed to PdSi at a reaction temperature of only 170°C. As the Pd reacts to form Pd_2Si, the Pd $3d_{5/2}$ core signal shifts 0.9 eV upfield from 334.6 eV to 335.5 eV. The shift toward higher binding energy indicates that charge is being transferred from Pd to Si upon Pd-Si bond formation. This is similar to the observed direction of charge transfer that occurs upon Ni-Si bond formation as discussed in Chapter III. The weak interfacial Pd signal is not observable because of its overlap with the intense Pd metal and Pd_2Si signals. The progression of the emerging Si 2p signals must be examined for information concerning the interface.

The evolution of the Si 2p position and intensity as the Pd/Pd_2Si interface advances is plotted in Figure 4. The first detectable Si 2p signal is plotted in Figure 4a. As the Pd/Pd_2Si interface advances toward the surface, the spectra in Figure 4b through 4e are obtained. In the final spectrum, Figure 4f, the Pd film has been completely consumed to yield an end product of Pd_2Si.

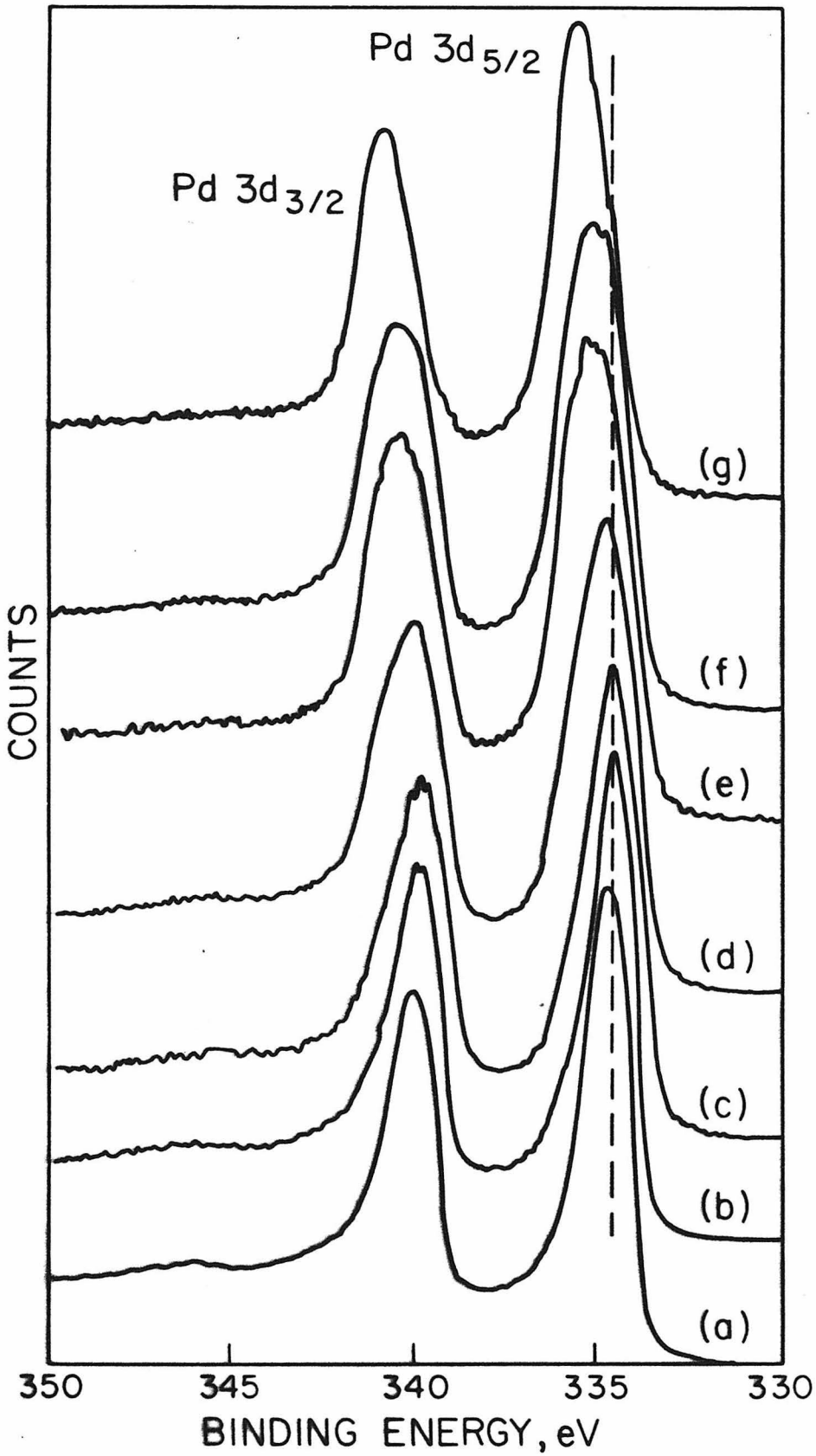

Figure 3: The Pd 3d XPS doublet obtained as a function of time as the Pd/Pd_2Si interface advances toward the sample surface.

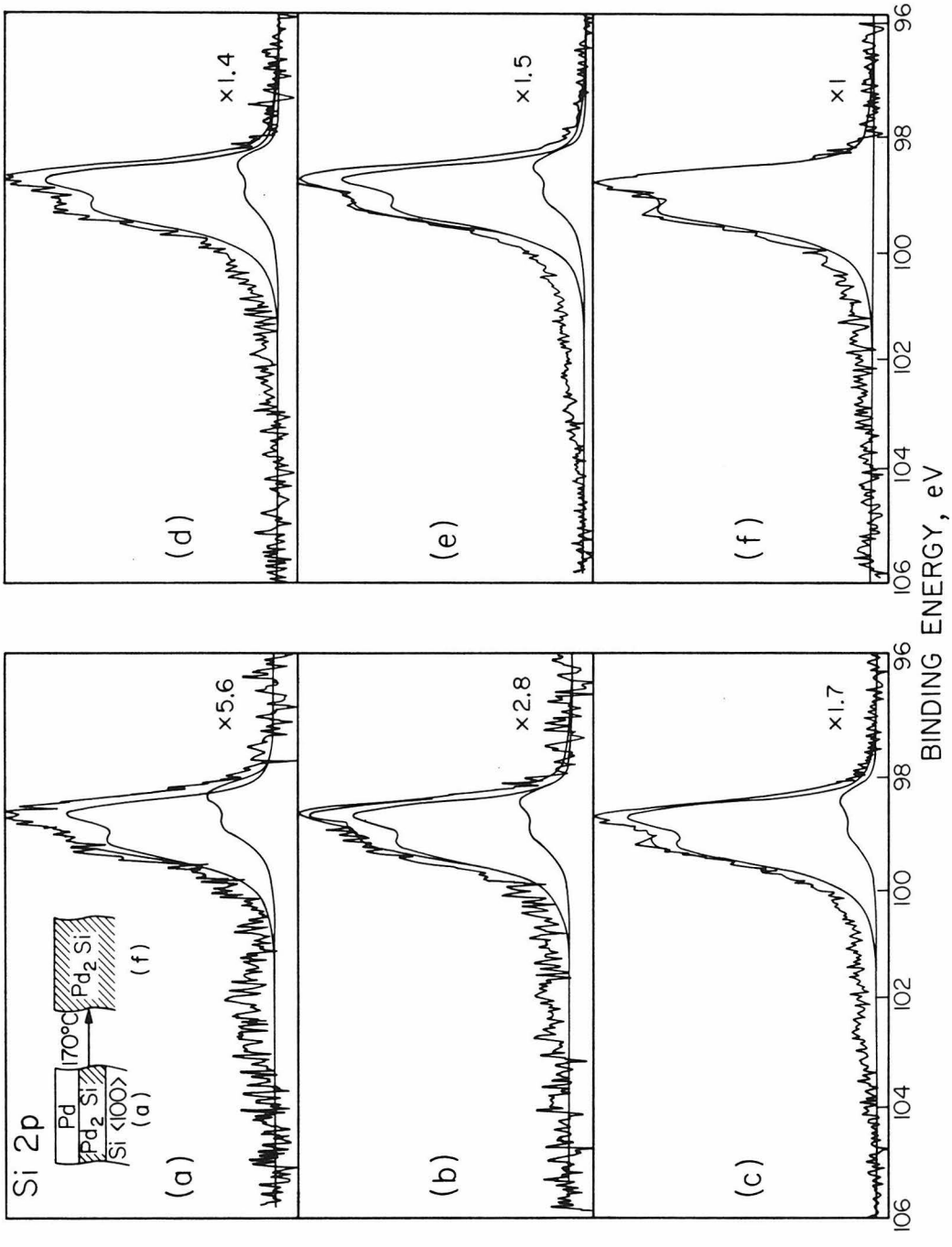

Figure 4: The Si 2p XPS spectra obtained as a function of time as the Pd/Pd_2Si interface advances toward the sample surface. The smooth curves represent components determined using a least square minimization criterion.

In Chapter III, Section 5, the influence of the interfacial width on the observed intensity ratio of the interface to the bulk silicide signal, I^{int}/I^{bulk}, was discussed in detail. It was shown that for a sufficiently wide interfacial region, only the interface Si 2p signal should be seen as the silicide reaction front advances. As the interface region dissipates at the sample surface, the bulk silicide signal should begin to dominate the spectra. On the other hand, if the interfacial region is narrow, then both the interfacial and bulk silicide signals should be detected simultaneously. Whereas a wide Ni/Ni_2Si interface characterizes the situation found with Ni_2Si grown on amorphous Si, a narrow interface was found for the case of Ni_2Si grown on <100> Si. The data suggest the latter is also true for Pd_2Si grown on <100> Si.

To test this hypothesis, two signals corresponding to a bulk Pd_2Si and an interfacial Si 2p signal were fitted to the spectra as in the Ni_2Si case using a least squares minimization criterion. A Si 2p signal from a clean Si <100> wafer was used as the lineshape model. The background signal, which was determined from a spectrum of the Si 2p region before any interfacial Si had emerged, was subtracted from the data. The position and height of the interface and bulk mode lineshapes were allowed to vary. The resulting least squares derived components and their sum are plotted with the raw data in Figure 4. Several features of the fitted spectra should be noted. First, the position of the interface and the bulk signals was found to remain constant in spectra 4a through 4e. Secondly, the ratio of the interface signal intensity to the bulk signal intensity was found to remain essentially

constant. As discussed in Chapter III, theory predicts that this ratio should remain constant for an ideal interface approaching the sample surface. Finally, in Figure 4b, the observed raw data can only be fit with a single lineshape. This is to be expected if the Pd overlayer has been consumed so that only Pd_2Si is now present. The apparent shift between the interfacial Si 2p and that from the bulk Pd_2Si is 0.3 eV. This compares to the 0.4 eV shift found for the Si 2p in the Ni/Ni_2Si.

Equation III-8 derived in Chapter III may be used to calculate the width of the interface. Using the average I^{int}/I^{bulk} ratio of 0.31 determined from Figure 4, one calculates $\Delta x > 0.12\ \lambda_{Si}^{int}$, where λ_{Si}^{int} is the escape depth of Si 2p electrons in the interfacial region. If a metallic-like escape depth of 15 Å is assumed, this places a lower limit on the Pd/Pd_2Si interface of ~ 2 Å. This lower limit is calculated assuming $D_{Si}^{int}\ \lambda_{Si}^{int}$ is equal to $D_{Si}^{bulk}\ \lambda_{Si}^{bulk}$. But the lower binding energy for the interfacial Si 2p as compared to the Pd_2Si indicates this region must consist of a Pd-rich silicide. This indicates $D_{Si}^{int} < D_{Si}^{bulk}$. Assuming the density of Si atoms at the interface is only one-half of that found in bulk Pd_2Si, one may calculate an upper bound for the interface width of $0.23\ \lambda_{Si}^{int}$ or ~ 4 Å, if λ_{Si}^{int} is 15 Å.

The presence of two nonequivalent Si sites might also be used to explain the two components found within the raw data envelope. However, the observation that only one model lineshape will fit the final Pd_2Si spectrum in Figure 4b suggests that this is not this case. The crystal structure for Pd_2Si lends further evidence for this conclusion. The

compound Pd_2Si is known to have the Fe_2P structure.[3] In this structure the Pd atoms at Z = 0 or Z = 1/2 form a pattern of triangular prisms. The Si atoms at Z = 0 or Z = 1/2 are in the centers of these prisms. Together, the Si and Pd atoms form a triangle-pentagon net.[4] Each Si atom is surrounded by a total of nine Pd atoms: six form the surrounding prism and three are positioned out through the centers of the rectangular prism faces. The reported bond lengths for Pd_2Si indicate there are in fact two crystallographically distinct Si sites.[2] For Si(1), there are six short Si-Pd bond lengths and three relatively longer Si-Pd distances. For Si(2), the situation is exactly reversed. That is, there exist three long and six short Si-Pd bond lengths. This suggests the nonequivalent Si sites are due to a slight puckering of the planar triangle-pentagon nets. This puckering is apparently insufficient to result in observable chemical shift differences between the two Si sites.

It has also been reported [5-6] that heat treatment of Pd_2Si in the range 250-600°C causes the accumulation of a thin ~ 3 Å overlayer of elemental Si over the silicide surface. Again, the final Pd_2Si Si 2p may be fit quite well with a single Si 2p lineshape suggesting that such an overlayer cannot be responsible for the signal we assign to the interfacial region. If elemental Si is present, it must fall at the same binding energy as the Si found in Pd_2Si. This would seem to be unlikely, although the possibility cannot be totally discarded because of relaxation and referencing ambiguities that arise when considering semiconductor binding energies.

2. The Pt/Pt_2Si Interface

The Pt/Pt_2Si interface may be examined by monitoring the Pt and Si photoemission signals as the Pt/Pt_2Si interface advances toward the surface. The lower plot in Figure 2 shows a broad energy spectrum obtained from a bulk Pt_2Si sample. Again, the major photoelectron lines are labeled according to their level of origin. For this interface, the Pt $4d_{5/2}$ line is monitored in detail as the silicide is grown *in situ*. This line was chosen over the more intense Pt 4f signal since the $4f_{5/2}$ and $4f_{7/2}$ spin-orbit components interfere slightly with one another.

Figure 5 plots the progression of the Pt $4d_{5/2}$ line as the Pt/Pt_2Si interface advances into the effective observation depth. Figure 5a corresponds to pure Pt metal, while Figure 5e corresponds to Pt_2Si. It is unlikely that the sample would have progressed to PtSi since formation of this second phase requires at least 300°C.[3] Furthermore, had PtSi formed after the Pt_2Si, a substantial decrease in the Pt 4d intensity would have occurred. Such a decrease was not observed. As the Pt metal reacted to form Pt_2Si, the Pt $4d_{5/2}$ signal shifted 1.6 eV upfield. This is the largest chemical shift observed in this work for the metal atom upon silicide formation. As found for Ni and Pd, charge is transferred from Pt to Si upon Pt-Si bond formation.

The progression of the emergent Si 2p signal is shown in Figure 6. The first detectable Si 2p is plotted in Figure 6a. In Figure 6d, the Pt film has been consumed to yield Pt_2Si.

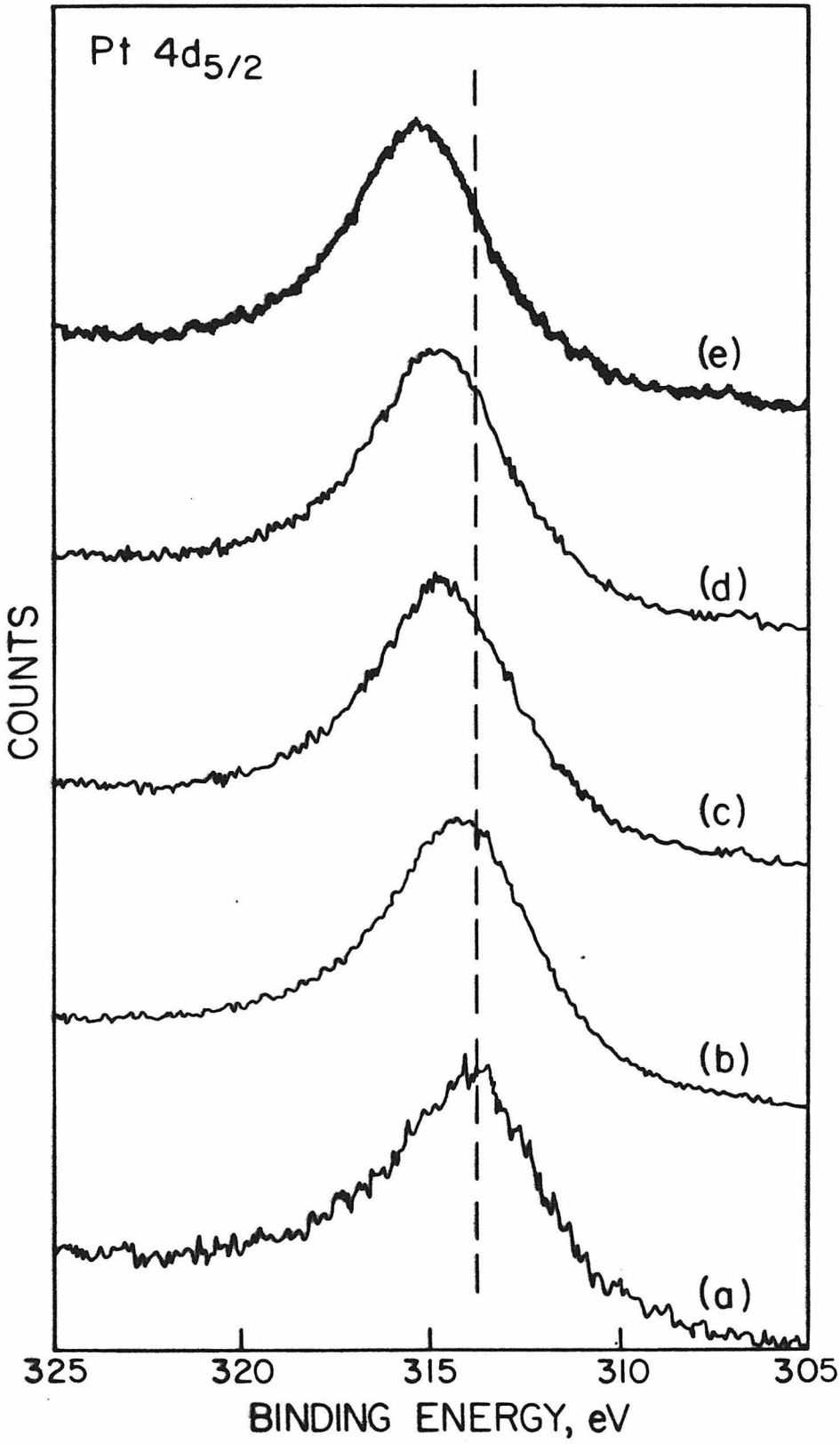

Figure 5: The Pt $4d_{5/2}$ XPS spectra obtained as a function of time as the Pt/Pt_2Si interface advances to the sample surface.

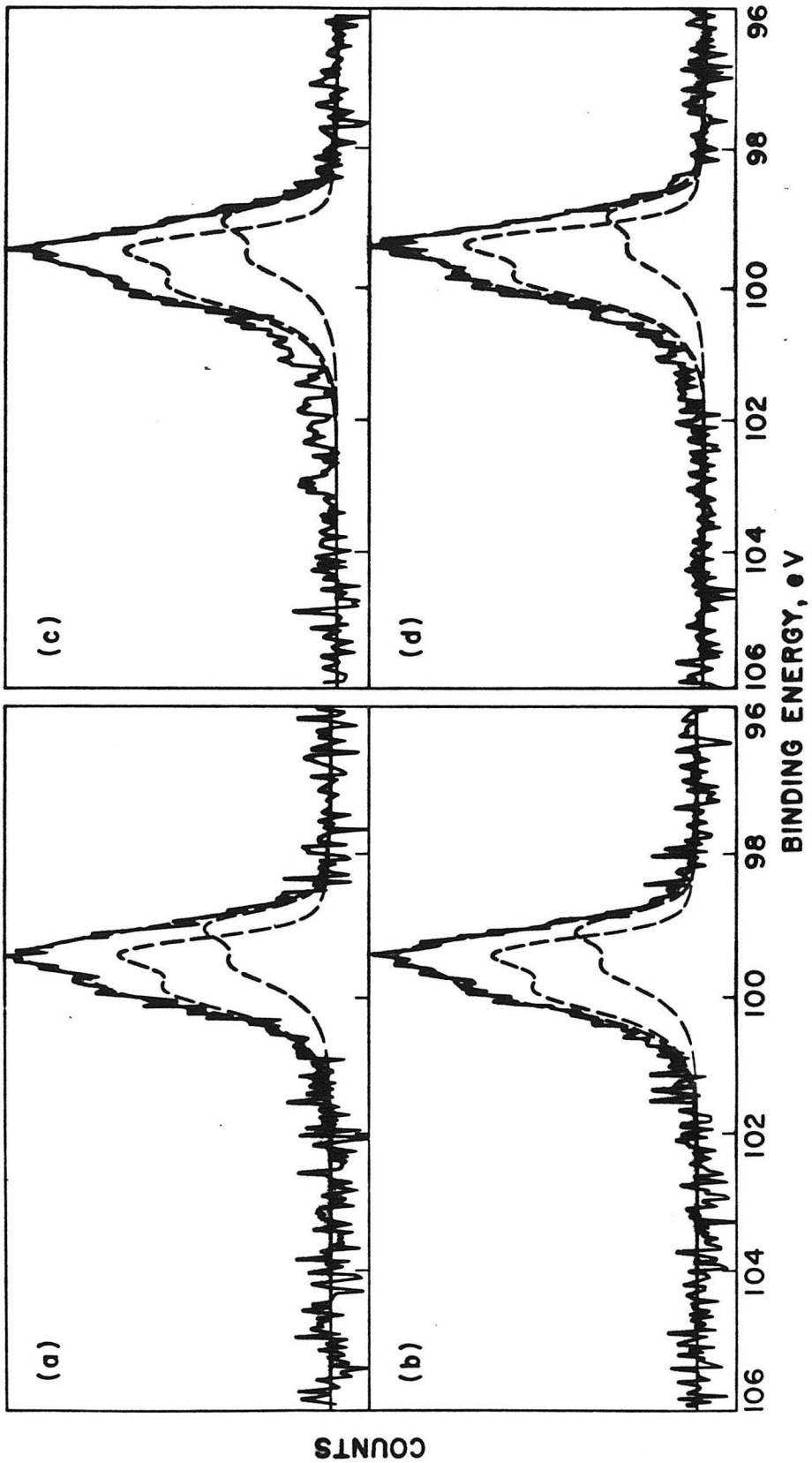

Figure 6: Plot of the Si 2p XPS spectra as the Pt/Pt_2Si interface advances toward the sample surface. The dashed spectra represent peak components determined using the least square criterion.

As discussed previously, the presence of a single peak envelope that remains constant in energy as the interface advances indicates a narrow interface width. Further, the distorted intensity distribution for the Si $2p_{1/2}$ - Si $2p_{3/2}$ spin orbit components also indicates that at least two components must be present in the peak envelope. As before, this envelope was fit with an interfacial and bulk Pt_2Si model signal. The model signal was obtained from a clean <100> Si sample. Again, the position and intensity of the component peaks were not constrained. The derived interface and bulk components along with their sum are plotted with the raw data in Figure 6. Again, several features of the fit components suggest they are reasonable estimates of the composite peaks within the raw data envelope. The positions of the interface and bulk signals remain constant in Figure 6a through 6d. The relative splitting between the two is found to vary from 0.33 eV to 0.40 eV with an average of 0.38 eV. In Figures 6a-6c, the I^{int}/I^{bulk} intensity ratio also remains constant (0.5-0.6), as theory predicts it should. In Figure 6d, the ratio drops to 0.4.

As noted previously, the spectrum in Figure 6d corresponds to the single species Pt_2Si. However, two components are indicated within the peak envelope by the least square procedure. There are two possible explanations for this observation: (1) The interface has not completely reached the sample surface. The lower I^{int}/I^{bulk} ratio for Figure 6d suggests the interface was just beginning to dissipate at this point. It is possible that either we stopped the reaction prematurely or that impurities in the Pt film impeded silicide formation by creating a

barrier to the metal diffusion.[7] (2) There are two crystallographically distinct Si sites in the Pt_2Si compound that are chemically distinct as well. It is known that Pt_2Si has the $CuAl_2$ structure[3] in which each Si is surrounded by eight Pt and two Si atoms.[4] Unfortunately, the details of the Pt_2Si structure are not known and it is not possible to ascertain if sufficient distortion exists to create nonequivalent Si sites. However, one may argue that if nonequivalent sites did exist, they should exist in a 1:1 ratio. This ratio is not indicated by the fitted spectra in Figure 6. Thus, we conclude that the two fit components in Figure 6 do indeed correspond to an interfacial and bulk region. Further experiments need yet to be done in order to substantiate this hypothesis.

Using equation III-8 and the average I^{int}/I^{bulk} of 0.5, the lower limit for the Pt/Pt_2Si interface is calculated to be 0.27 λ_{Si}^{int}. If λ_{Si}^{int} is assumed to be 15 Å, this corresponds to $\sim$ 4 Å. A reasonable upper limit is estimated by assuming the density of Si atoms at the Pt/Pt_2Si interface is only one-half of that found in Pt_2Si. This results in an estimation of the upper limit of 0.46 λ_{Si}^{int} or $\sim$ 7 Å, assuming a value of 15 Å for λ_{Si}^{int}.

D. SUMMARY

In this chapter, the Pd/Pd_2Si and Pt/Pt_2Si interfaces were examined by monitoring the silicide reaction *in situ* as a function of time. The estimated interfacial widths and relative binding energy shifts are summarized in Table 1. The data from Chapter III for the Ni/Ni_2Si interface using a Si <100> substrate is included for comparison.

The absolute binding energy of the Si atoms at the Ni/Ni_2Si, Pt/Pt_2Si, and Pd/Pd_2Si interfaces can also provide significant chemical information. It was found for both Ni and Pd, the interfacial Si 2p falls at 98.35 eV. This indicates the electron density in the Si atom must be similar in each of these environments. The Si 2p signal for the Pt interface falls 0.5 eV higher at 98.85 eV. Less charge transfer to the Si atom has occurred in this case. It was established previously with the Ni case that the degree of charge transfer to the Si is established by two factors: (1) the strength of the metal-Si bond and (2) the number of strong bonds formed, i.e., the coordination environment. Since the Ni and Pd have the same binding energy for the interfacial Si, the limiting environment for Si at the Pd/Pd_2Si interface is Si substituted in the fcc metal lattice, as was argued to be the case for Ni in Chapter III. In the case of Pt, the higher binding energy signal indicates that either the bond strength or the number of Pt-Si bonds have been reduced in the limiting interfacial environment. In view of the similarity of the chemistry of Pt and Pd, it seems unlikely that the difference in the binding energy can be entirely attributed to variations in bond strength. We therefore conclude that the interfacial Si in the Pt/Pt_2Si interface rests in a site of substantially lower coordination number in the fcc lattice. This is suggestive of an interstitial defect site.

Further evidence for the lower Si coordination environment at the Pt interface can be derived from an analysis of the binding energy of the bulk silicides. The Si in Ni_2Si and Pd_2Si falls at 98.75 eV and

98.65 eV, respectively. There are nine metal neighbors for each Si in both structures. Consequently, this 0.1 eV binding energy difference suggests an increase in the charge transfer in the Pd-Si bond relative to the Ni-Si bond. This is consistent with the binding energies found for the Ni 2p and Pd 3d lines for these bulk silicides. To first order, we expect similar bond strengths for Pt-Si and Pd-Si bonds. The observed binding energy for Si in bulk Pt_2Si falls at 99.25 eV. This 0.6 eV shift relative to Pd_2Si we interpret as indicative of a lower coordination number for the Si and a substantial difference in structure. In Pt_2Si, there are only eight Pt-Si bonds, an observation which is consistent with the binding energy interpretation.

The gradual shift of the Pd 3d and Pt 4d core lines as their respective metal/silicides advance suggests that both of these transition layers are graded in composition. Estimations of the interfacial widths indicate that the metal/silicon interface widths decrease in the order Ni > Pt > Pd. This is consistent with work reported by Cheung,[8] in which he studied the Ni_2Si/Si and Pd_2Si/Si interfaces using a thin crystal channeling technique. Cheung reported that the number of disordered Si atoms in the interfacial region decreases in the order Ni > Pd. This agrees with the work reported here if one can assume that the relative trend of the interfacial widths holds true for the opposite interface.

These preliminary experiments suggest substantial differences in the Si chemical environment in the Pt-Si system. Further detailed comparisons of charge transfer in the Pt and Pd silicides should enable a

comparison of the bonding roles of 4d/5s and 4f/5d/6s configurations. A particularly powerful extension of the dynamic growth experiments would be to examine the silicide/Si interfaces using thin (1600-3000 Å) Si crystals. In this situation, the silicide reaction can be monitored through the thin Si crystal. The emerging metal signals may be used to ascertain the chemical nature and width of these interfaces.

Table 1: Summary of Metal/Silicide Data

Transition Metal	Interfacial Width	ΔBE Si 2p (silicide-interface)	ΔBE Metal (silicide-metal)	Si 2p Silicide
Ni	0.6-0.9λ (9-14 Å)*	0.4 eV	0.5 eV	98.75 eV
Pt	0.27-0.46λ (4-7 Å)*	0.4 eV	1.6 eV	99.25 eV
Pd	0.12-0.23λ (2-4 Å)*	0.3 eV	0.9 eV	98.65 eV

*Assuming a value of 15 Å for λ

References

1) K. S. Kim, A. F. Gossman, N. Winograd, Anal. Chem., 46, 197 (1974)

2) Structure Reports, W. B. Pearson, ed., 31A, 56.

3) K. N. Tu and J. W. Mayer in Thin Films, Interdiffusion and Reactions, J. M. Poate, K. N. Tu, J. W. Mayer, eds. (John Wiley and Sons, New York, N.Y., 1978)

4) W. B. Pearson, The Crystal Chemistry and Physics of Metals and Alloys (John Wiley and Sons, New York, N.Y., 1972)

5) J. L. Freeouf, G. W. Rubloff, P. S. Ho, T. S. Kuan, Phys. Rev. Lett., 43, 1836 (1979)

6) K. Oura, S. Okada, T. Hanawa, Appl. Phys. Lett., 35, 705 (1979)

7) C. A. Crider, J. M. Poate, Appl. Phys. Lett., 36, 417 (1980)

8) N. Cheung, Thesis, California Institute of Technology, Applied Physics Department, 1980

VII. PROPOSITIONS

CONFORMATIONAL INVESTIGATION OF THE *LAC* REPRESSOR-OPERATOR DNA INTERACTION WITH FT-IR AND RAMAN SPECTROSCOPY

ABSTRACT

It is proposed that the conformational changes that occur in *lac* repressor protein and operator DNA upon complex formation be investigated with Fourier transform infrared and Raman spectroscopy. Five specific experiments are suggested.

INTRODUCTION

The *lac* repressor protein regulates the synthesis of the enzymes necessary for lactose metabolism in the bacteria *Escherichia coli*. The protein exerts this control by binding to a specific region of DNA known as the operator. This specific binding blocks the transcription of the lactose operon by RNA polymerase. Small inducer sugar molecules initiate enzyme production by binding to the repressor and destabilizing the protein-DNA complex. This causes the repressor to dissociate from the DNA, allowing the initiation of messenger RNA synthesis.

The interaction of repressor with operator DNA has been intensely studied as a model system for the regulation of gene expression. Much evidence has been presented indicating that conformational changes in the protein and DNA play an important role in the mechanism of enzyme regulation in the *lac* operon system. Changes in the protein fluorescence[1], ultraviolet absorbance,[2,3] sedimentation coefficient[3], and circular dichroism[1,3] have been reported on binding of inducer molecules to

repressor. These studies have concluded that inducer binding causes a conformational change in the repressor protein and that it is this change which is responsible for the reduced affinity of repressor for operator DNA. In addition, the possibility exists that the repressor undergoes a conformational change upon binding to operator DNA. Similarly, the conformation of the DNA itself may also change upon protein binding. A number of studies concerned with protein and DNA conformational changes have been reported using non-operator DNA. By chemically modifying the repressor with fluorescein mercuric acetate, Burgum and Matthews found evidence of a rearrangement of the tertiary structure of repressor upon non-specific DNA binding.[4] The spectral changes indicated that many of the models of DNA binding which invoke only the terminal regions of repressor protein need to be reexamined. Their data strongly suggest that specific operator DNA binding may also involve rearrangement of the protein conformation. The conformational changes in non-operator DNA itself have been examined by circular dichroism (CD) studies.[5] Here it was found that the CD spectrum of the repressor-non-operator DNA complex could be interpreted as a change in the conformation of the DNA. The authors suggested that some of the base pairs of the native structure are tilted relative to the free DNA.

JUSTIFICATION

To date, there have been no physical chemical studies of the repressor-operator DNA interaction. Physical studies for this case have not been feasible in the past because the available operator DNA also contained

a large excess of non-operator DNA. In the last few years, however, sufficient quantities of small fragment operator DNA (<30 base pairs) have become available, either through the cloning technology[6] or through direct chemical synthesis of the operator polynucleotide.[7,8] These small operator fragments make physical studies of specific DNA binding possible for the first time. It would be of great interest to examine the conformational changes of repressor and operator DNA that occur upon complex formation. Clearly, more repressor functional groups are involved in binding to operator DNA than to non-operator DNA since the latter binding is much weaker.

PROPOSAL

It is proposed here that the effect of complex formation on the structure of repressor and operator DNA be examined using Fourier transform infrared (FT-IR) and Raman spectroscopy. A comprehensive body of literature exists demonstrating the utility of these vibrational spectroscopies for obtaining structural information about protein and DNA conformations.[9-12]

APPROACH

In particular, the IR spectra of proteins and polypeptides exhibit nine characteristic absorption bands which have been assigned to the motion of the basic structural unit, the amide linkage C_α-CONH-C_α'. The frequencies of these amide bands and their assignments are summarized in Table 1. The frequency of the amide I-III motions as well as the low

energy backbone motions of amide IV-VI have been shown to depend on the secondary structure of the protein.[13-18] A summary of the energies characteristic of α-helix, β sheets, and random coils may be found in reference 19.

In addition to the amide bands mentioned above, unique frequencies attributable to α-helix and β sheet configurations have been assigned at 376-369 and 265-235 cm^{-1}, respectively.[15-17,20] These vibrations are admixtures of backbone angle deformations and amide bond torsion allowed by the specific coupling in an α-helix or β sheet.[19] The utility of these unique bands for probing the structure or proteins has been demonstrated in IR studies of collagen and whale myoglobin. Perturbation of the 376-369 cm^{-1} band has also been used to demonstrate the association of a helical structure with the metal binding site in plastocyanin.[19]

Raman spectroscopy, as a complement to IR, may also be used to investigate protein-nucleic acid interactions. Deductions concerning protein conformation can be made based on the following generalizations derived from Raman spectra of polypeptide model complexes.[12] α-Helical structures have a strong sharp amide I line at 1654 ± 5 cm^{-1} and a weak, broad amide III line at 1285 ± 15 cm^{-1}. An additional line at 900-950 cm^{-1} possibly due to a backbone vibration has also been attributed to α-helix structure. β sheet structures produce a strong sharp amide I line near 1670 ± 5 cm^{-1} and a strong amide III band at 1235 ± 10 cm^{-1}. Random coil structures produce a strong amide I and a medium intensity amide III line at 1665 cm^{-1} and 1246 cm^{-1}, respectively. In addition to the amide

regions, there are other Raman frequencies known to be sensitive to protein conformation. One such region occurs at 500-725 cm^{-1} and has been assigned to the bond-stretching vibrations of the C-S-S-C and C-S groups.[23-25] These sulfide group frequencies have been found to be quite sensitive to structural changes.

In addition to the information concerning protein structure, IR and Raman spectroscopy offer a means of studying changes in nucleic acid conformation. Several studies have demonstrated that IR provides an unequivocal method for measuring the degree of base-pairing in RNA because of the large frequency shifts that occur in vibrational bands when pairing occurs.[26,27] Raman spectra of nucleic acids have been shown to be sensitive to base-stacking interactions, hydrogen-bonding interactions (including base pairing), the orientation of the backbone residues, and the binding of metal ions to the phosphate or base substituents.[12]

Only a few applications of these vibrational spectroscopies to the study of protein-nucleic acid interactions have emerged. Most studies have been concerned with the separate components only. The recent studies of nucleic acid-protein systems have been quite successful, however. Using laser Raman, Prescott, et al., examined the extent of conformation changes in both DNA and polypeptide backbones upon complex formation.[28] They were able to demonstrate that both the geometry of the backbone and the mode of interaction between stacked bases of polyriboadenylic acid are altered by the binding of polylysine. On the other hand, when polylysine binds to calf thymus DNA, they found that the DNA backbone

structure was not perturbed. The interactions between the bases of the DNA double helix were significantly altered, however. These results were used to develop models for the peptide-DNA binding mechanisms. Using IR spectroscopy, Cotter and Gratzer[26,27] compared spectra of E. coli ribosomes with those of RNA and protein extracted from the ribosomes. They were able to conclude that the conformation of RNA in the ribosome is very similar to free RNA in solution in terms of the extent of base pairing.

The studies discussed above indicate the vibrational spectra of proteins and nucleic acids are understood well enough to provide valuable information regarding repressor-operator DNA interactions. Although many IR and Raman experiments are possible, several particular ones are suggested below.

A Fourier transform IR spectrometer is suggested for this study. It has two major advantages over the conventional dispersion-grating spectrophotometers: (1) It has a higher sensitivity and signal/background ratio that will allow the detection of very weak or very low frequency IR bands. (2) The digital processing of the spectra may be exploited to compensate for the strong absorbtion of water at 1640 cm^{-1} which interferes with the amide I frequency. Several studies using FT-IR have successfully removed the water contribution by digital subtraction.[22] This feature is also very significant since it will allow the detection of subtle changes in the vibrational spectra through difference spectra.

SUGGESTED EXPERIMENTS

(1) Although knowledge about the structure of the *lac* repressor is limited, circular dichroism and optical rotary studies have estimated a 33-40% helix content and a 18-40% β-sheet content.[21] Both the amino and carboxy termini have been predicted by Chou and Fasman to contain long helical regions.[29] Genetic evidence and experiments with trypsin digestion of repressor (which removes the 59 amino and 20 carboxy terminal residues) strongly suggest that one or both of the terminal peptide regions of repressor are involved in operator DNA binding. This possibility may be tested by examination of the low energy vibrational bands (376-369 cm^{-1}) that have been attributed to α-helix structure. Perturbation of the α-helix structure in the terminal residues upon DNA binding will be manifested as a shift in the vibrational frequency.[19]

(2) Circular dichroism studies of repressor binding to non-operator DNA have tentatively interpreted spectral changes as resulting from a partial base-tilting of the DNA, perhaps towards the A form.[5] This may be further investigated by a comparison of the Raman spectra for the free DNA and the repressor-bound operator DNA. This should yield information concerning the perturbation of the nucleic acid backbone conformation, base-stacking interactions, and base-pairing caused by protein binding.

(3) Extensive β-sheet structure has been predicted in the tryptic core of repressor. It has been proposed that this β-sheet structure is involved in the stabilization of the repressor tetramer. Since the repressor may be dissociated into monomer subunits and then reassociated

into active tetramers,[30] comparison of the IR vibrational spectra of the monomer and tetramer units in the 265-235 cm^{-1} energy region will yield information concerning β-sheet involvement in tetramer stabilization.

(4) Butler et al.[5] have reported that the reaction rate of the repressor sulfhydryl groups with 4,4'-dithiodipyridine is decreased almost two-fold by DNA binding. As one interpretation of their kinetic data, they suggest that the accessible -SH groups of 2 repressor subunits are blocked by DNA binding, while the -SH groups on the other 2 subunits remain unperturbed. This possibility may be tested straightforwardly using the Raman scattering of the sulfhydryl group of cysteine at 2575 cm^{-1}. Since its shift upon deuteration (to $\sim$ 1875 cm^{-1}) is very easy to detect, the accessibility of -SH groups to the solvent with and without DNA binding may be determined by observing the rate of deuterium exchange.

(5) The amino terminus of repressor contains four of the eight tyrosine residues found in *lac* repressor. It has been suggested that these residues are involved in the interaction with DNA by providing -OH groups (which can form hydrogen bonds with the DNA bases) or by intercalation between the DNA bases. These possibilities may be examined using Raman. It has been found that tryptophan, histidine, phenylalanine, and tyrosine all produce intense Raman lines. These lines show little response to protein conformational changes, except for tyrosine. The tyrosine band at 825-855 cm^{-1} appears to be highly sensitive to environmental changes. Examination of the Raman scattering of tyrosine may give insight into the roles of tyrosine residues on the amino terminus.

(6) Finally, the above IR and Raman experiments may also be performed in the presence of inducers and anti-inducers to determine their effect on the various conformational changes.

TABLE I *

Band	frequency range	approximate description
Amide A	∿3300	N-H
Amide B	∿3100	N-H str (in Fermi resonance with 2 x amide II)
Amide I	1597-1680	C=O str, N-H def, C-N str
Amide II	1480-1575	C-N str, N-H def
Amide III	1229-1301	C-N str, N-H def
Amide IV	625-767	O=C-N def
Amide V	640-800	N-H def
Amide VI	537-606	C=O def
Amide VII	200	C-N tor

Abbreviations: str, stretching; def, deformation; tor, torsion

*from reference 12

References

1) S. L. Laiken, C. A. Gross, P. H. von Hippel, J. Mol. Biol., 66 (1972) 143

2) K. S. Matthews, H. R. Matthews, H. W. Thielmann, O. Jardetzky, Biochem. Biophys. Acta, 295 (1973) 159

3) Y. Ohshima, M. Matsuura, T. Horiuchi, Biochem. Biophys. Res. Commun., 47 (1972) 1444

4) A. A. Burgum, K. S. Matthews, J. Biol. Chem., 253 (1978) 4279

5) A. P. Butler, A. Revzin, P. H. von Hippel, Biochemistry 16 (1977) 4757

6) H. L. Heyneker, J. Shine, H. M. Goodman, H. W. Boyer, J. Rosenberg, R. E. Dickerson, S. A. Narang, K. Itakura, S. Lin, A. D. Riggs, Nature, 263 (1976) 748

7. P. B. Bahl, R. Wu, K. Itakura, N. Katagiri, S. A. Narang, Proc. Nat. Acad. Sci., 73 (1976) 91

8) P. B. Bahl, R. Wu, J. Stawinsky, S. A. Narang, Proc. Nat. Acad. Sci. 74 (1977) 966

9) F. S. Parker, Applications of Infrared Spectroscopy in Biochemistry, Biology, and Medicine (Plenum Press, New York, N.Y.) 1971

10) H. Susi, in Structure and Stability of Biological Macromolecules, Vol. III (S. N. Timasheff and Fasman, eds.) Marcel Dekker, New York, N.Y., 1969

11) B. G. Frushour, J. L. Koenig, in Advances in Infrared and Raman Spectroscopy (R. J. H. Clark, R. E. Hester, eds.) Heyden and Son, Ltd, London, 1975

12) G. J. Thomas, Y. Kyogoker, in Infrared and Raman Spectroscopy, Part C (E. G. Brame, J. G. Grasselli, eds.) Marcel Dekker, Inc., New York, N.Y., 1977

13) A. Elliott, E. J. Ambrose, Nature, 165 (1950) 921

14) T. Miyazaw, in Polyamino Acids, Polypeptides, and Proteins, M. A. Stahmann, ed., (Univ. of Wisc. Press, Madison, Wisc.) 1962

15) K. Itoh, T. Shimanouchi, O. Oya, Biopolymers, 7 (1969) 649

16) K. Itoh, T. Nakahara, T. Shimanouchi, K. Uno, Y. Iwakura, Biopolymers, 6 (1968) 1759

17) K. Itoh, H. Katabuchi, Biopolymers, 11 (1972) 1593

18) F. Heitz, B. Lotz, G. Spach, J. Mol. Biol., 92 (1975) 1

19) J. Hare, Thesis, California Institute of Technology

20) K. Itoh, H. Katabuchi, Biopolymers, 12 (1973) 921

21) B. Muller-Hill, Prog. Biophys. Molec. Biol., 30 (1975) 227

22) L. D'Esposito, J. L. Koenig, in Fourier Transform Infrared Spectroscopy, Vol. I (F. R. Ferraso, L. J. Basile, eds.) Academic Press, New York, N.Y., 1978

23) R. C. Lord, N. T. Yu, J. Mol. Biol., 51 (1970) 203

24) A. M. Bellocq, R. C. Lord, R. Mendelsohn, Biochim. Biophys. Acta, 257 (1972) 280

25) M. C. Chen, R. C. Lord, R. Mendelsohn, J. Amer. Chem. Soc., 96 (1974) 3038

26) R. I. Cotter, W. B. Gratzer, Nature 221 (1969) 154

27) R. I. Cotter, W. B. Gratzer, Eur. J. Biochem. 8 (1969) 352

28) B. Prescott, C. H. Chou, G. J. Thomas, J. Phys. Chem., 80 (1976) 1164

29) P. Y. Chou, G. D. Fasman, Biochemistry, 233 (1971) 67

30) J. R. Sadler, M. Tecklenburg, Biochemistry, 15 (1976) 4353

INVESTIGATION OF THE METALLIC NICKEL 2p PHOTOEMISSION SATELLITE USING X-RAY FLUORESCENCE

ABSTRACT

It is proposed that the Kα x-ray fluorescence spectra of metallic nickel and nickel alloys be examined. This should allow one to distinguish between the various final state explanations for the satellite structure observed on the Ni^{o} 2p photoemission line.

INTRODUCTION

The photoelectron spectra of insulators quite often display satellite structure in addition to the expected photoemission lines. Most metals, on the other hand, exhibit relatively simple core electron photoemission lines consisting only of a spin-orbit doublet. The major exception to this is nickel. Both the core levels and valence level photoelectron spectra of Ni^{o} are complicated by the presence of strong satellite lines approximately 6 eV upfield of the main electronic line.[1] Several possible explanations for this satellite structure in terms of various many electron effects have been presented in the literature.

Normally, a single photoelectron peak per orbital is expected according to the photoelectric effect:

$$E_e = h\nu - E_B$$

where E_e = kinetic energy of the photoejected electron

$h\nu$ = energy of the impinging photons

The binding energy of the electron, E_B, may be defined as

$$E_B = E_F - E_I$$

where E_I = the total energy of the initial neutral atom

E_F = the total energy of the resultant ion

If more than one possible final state exists after an electron has been removed from a core orbital, more than one photoelectron peak will occur. For the case of the Ni^o 2p satellite, two possible final state effects have been suggested: (1) multiplet or exchange splitting[1,2] and (2) electron shake-up.[3]

Multiplet splitting results from the coupling of the 2p shell in which a vacancy has been created by the photoionization process with the unfilled 3d shell of the metal ion. The remaining 2p electron may couple spin-parallel or spin-antiparallel with the unpaired valence electrons. The spin-parallel electrons will experience an electron exchange potential which will tend to reduce the average Coulombic repulsion.[4] The spin-parallel electrons will thus be favored energetically, and a split photoelectron emission will result.

Electron shake-up structure is the result of a monopole excitation. When a 2p core electron is removed by photoionization, the sudden creation of a 2p vacancy ($<10^{-15}$ sec) abruptly changes the effective charge seen by the remaining electrons. In the sudden approximation,[5] the remaining electrons relax toward the positive hole. The subsequent relaxation energy may be used to excite a second electron into an unoccupied bound

state. As a result, one will observe a satellite line at a kinetic energy lower than the main photoelectron line, and with an energy separation that corresponds to the shake-up transition. It has been suggested that the Ni^{o} 2p satellite is due to the excitation of a metal 3d electron into an unoccupied predominantly 4s metal orbital.[3]

One possible experiment for distinguishing between multiplet splitting and electron shake-up for the Ni^{o} 2p satellite is to examine the satellite structure associated with the deeper 1s core level. One would expect that the coupling between the unfilled 3d shell and a given core orbital would decrease as the principal quantum number decreased Thus, then energy separation between the main electronic line and the satellite should decrease. Hartree-Fock calculations have shown, in fact, that the multiplet splitting energies are negligible for the 1s shell.[6] If the origin of the Ni^{o} 2p satellite is multiplet splitting, the Ni^{o} 1s line should display no satellite structure at all. Electron shake-up, on the other hand, should vary only with the chemical environment of the Ni atom. Each Ni subshell will display the same satellite structure, as long as the subshell is at least one principal quantum number lower than the shell undergoing shake-up.

PROPOSAL

The difficulty with the above experiment is that the Ni 1s electrons have a binding energy of $\sim$ 8300 eV. Most x-ray photoelectron spectrometers use Al Kα or Mg Kα x-rays which have energies of 1487 eV and 1254 eV, respectively. The harder x-rays from the Cu Kα transition are generally

necessary to create K shell vacancies, but again the energy of this line (8048 eV) is not sufficient to promote photoemission from the Ni 1s shell.

As an alternative method for distinguishing between multiplet splitting and electron shake-up mechanisms for the metallic Ni 2p satellite, it is proposed here that the Kα x-ray emission spectra of metallic nickel and nickel alloys be examined. The alloys $Ni_{50}Zn_{50}$, $Ni_{20}Zn_{80}$, and $Ni_{50}Al_{50}$ are suggested because their electron photoemission spectra are already available in the literature.[3] Since Kα x-ray emission is the result of a 2p→1s electron transition, the final state after x-ray emission is the same as the final state resulting from the photoionization of the 2p shell. Thus, if the Ni^{o} 2p photoemission satellite is a result of multiplet splitting, multiplet structure should also be observed in the Kα x-ray fluorescence spectrum. On the other hand, shake-up transitions occur before deexcitation by x-ray fluorescence is possible. Thus, if an electron shake-up mechanism is reponsible for the Ni^{o} 2p satellite, one should not observe any structure on the Kα x-ray emission spectrum. The experiment is straightforward to perform and should yield unambiguous results concerning the nature of the metallic Ni 2p satellite. The understanding of such satellite structure is important since a large potential exists for the use of satellites for elucidating the nature of chemical bonding in solids.

References

1) S. Hufner, C. K. Wertheim, Phys. Lett., 51A (1975) 299

2) C. S. Fadley, D. A. Shirley, Phys. Rev. A, 2 (1970) 1109

3) P. T. Andrews, T. Collins, C. E. Johnson, P. Weightman, J. Electron Spectrosc. and Related Phenom., 15 (1979) 39

4) J. C. Slater, Quantum Theory of Atomic Structure (McGraw-Hill, New York, N.Y., 1960), Vol. II

5) T. A. Carlson, Photoelectron and Auger Spectroscopy (Plenum Press, New York, N.Y.) 1975

6) T. A. Carlson, J. C. Carver, L. J. Saethre, F. G. Santibanez, G. A. Vernon, J. Electron Spectrosc. and Related Phenom., 5 (1974) 247

VALENCE BAND STUDIES OF THE CHEMICAL BONDING IN THE TRANSITION METAL SILICIDES

ABSTRACT

It is proposed that the detailed electronic structure of the chemical bonds formed in the transition metal silicides and their interfaces to silicon be examined using XPS derived valence band structure. Data are presented that demonstrate that the evolution of the valence region can be examined using the dynamical growth experiments developed in this thesis.

INTRODUCTION

The relevance of transition metal silicides to modern device technology has motivated many recent studies concerned with the chemical properties of silicides and their interfaces to silicon.[1-3] These studies typically employ multiple monolayer depositions of the transition metal onto single crystal silicon substrates. The development of the metal/silicide interface is then monitored using Auger electron spectroscopy (AES) or ultraviolet photoelectron spectroscopy (UPS). These spectroscopic data have been interpreted on two levels: 1) to ascertain the stoichiometry of the solid phase reaction products, and 2) to derive information concerning the electronic band structure of the material. Interpretation of AES and UPS spectra in terms of the electronic density of states is not particularly straightforward. In the UPS regime ($h\omega < 50$ eV), transitions occur between occupied and empty bands and the structure of the experimental energy distribution curve (EDC) is inter-

preted in terms of structure in the energy distribution of the joint density of states.[4] Because of the low energy of the photoejected electrons, the initial and final states are closely coupled. In the AES studies, the LVV line of silicon is monitored. The resulting spectrum is a measure of the electron charge only in the vicinity of the particular atom upon which the core hole is localized.[5] Thus, AES yields information about the local portion of the total valence charge density or the partial density of states.

PROPOSAL

The proposition discussed here is two-fold. First, it is proposed that XPS be used to examine the electronic band structure of the transition metal silicides and their interfaces to silicon. Second, it is further proposed that the dynamical interfacial studies developed in Chapter III of this thesis be used to examine the evolution of the valence region as the silicide is formed. This will complement the conventional thin film deposition technique used in the above studies.

In XPS, the energy of the emitted photoelectron is large. The essentially free-electron states at high photoelectron energies mean the probability of coupling between the initial and final states is low and thus XPS valence emission will reflect the density of states with little or no modulation. Experimentally observed intensity ratios are modulated by photoionization cross sections which basically depend on the atomic composition of the valence wave functions.

To demonstrate the application of the experimental approach developed in Chapter III to valence studies, the progression of the

valence band spectra was examined as the Si/Ni_2Si interface advanced toward the sample surface. The results are shown in Figure 1. In Figure 1a, the interfacial region has not yet advanced into the effective observation depth of the spectroscopy. Thus only the valence band structure of the amorphous silicon is obtained. Figure 1b corresponds to the valence structure obtained when the first nickel core level is detected. The remaining spectra in Figure 1 show the valence region as the Si/Ni_2Si interface continues to advance until the Si overlayer is completely consumed to yield Ni_2Si (Figure 1e).

These data indicate that the valence spectra of the interfacial region can be obtained without the structural or chemical perturbations introduced by conventional depth profiling techniques. The metal d band at ∿2 eV corresponding to the interfacial region (Figure 1b) can be observed to be shifted relative to the d band from the bulk silicide. In addition, the density of states at the Fermi level is also changing as the film progresses from pure Si to Ni_2Si.

The dynamic experiment illustrated above is complemented by the conventional approach of multiple monolayer depositions of Ni onto <100> Si. The valence region as a function of Ni coverage is shown in Figure 2. The Ni coverage was determined using $^4He^+$ backscattering with an independently calibrated standard.[7] The lowest Ni coverage is 8×10^{13} Ni/cm^2 which corresponds to ∿0.1 monolayer. Again, it can be observed that the Ni d band is shifted considerably with respect to that obtained at higher Ni coverages. The use of single crystal silicon also allows one to examine the evolution of the Si s-p bands at ∿7 and

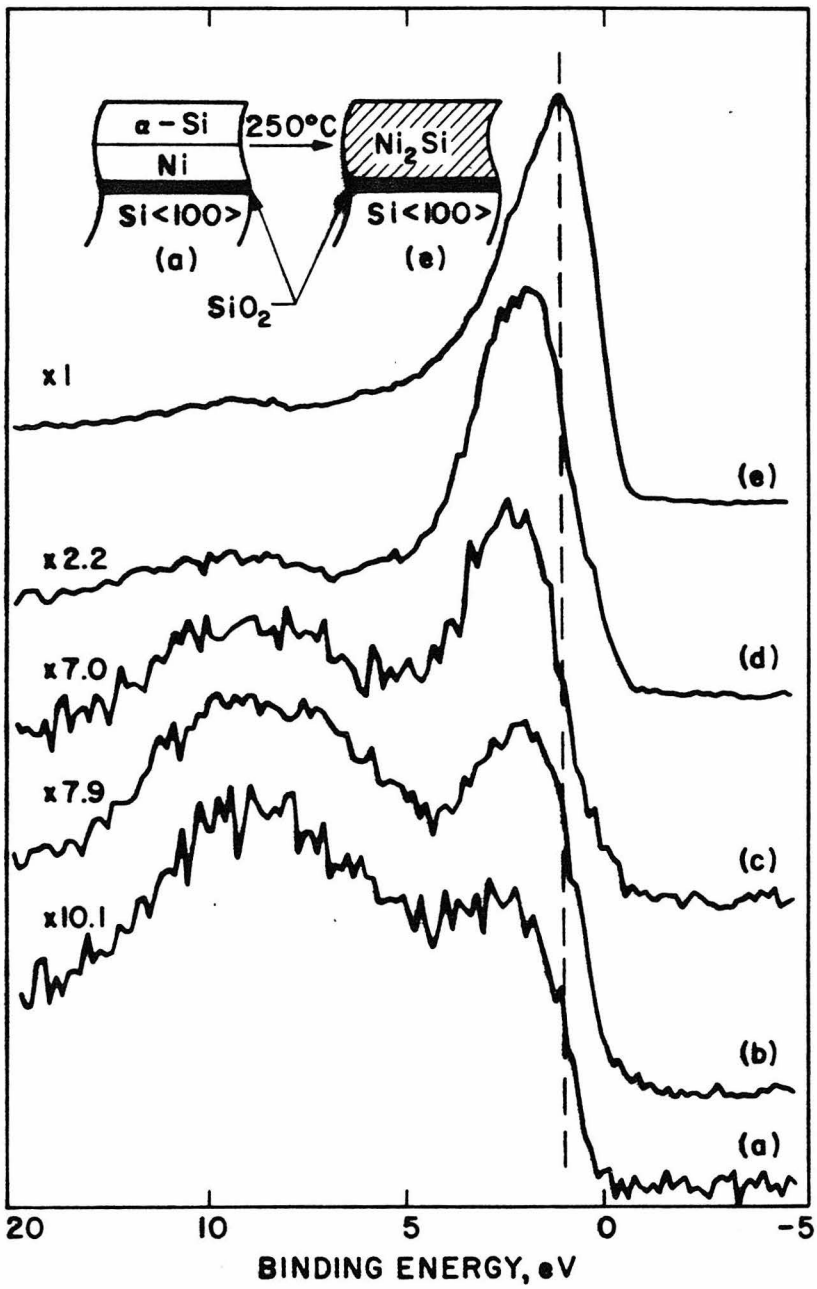

Figure 1: Plot of the XPS derived valence bands as a function of time as the Si/Ni_2Si interface advances toward the sample surface.

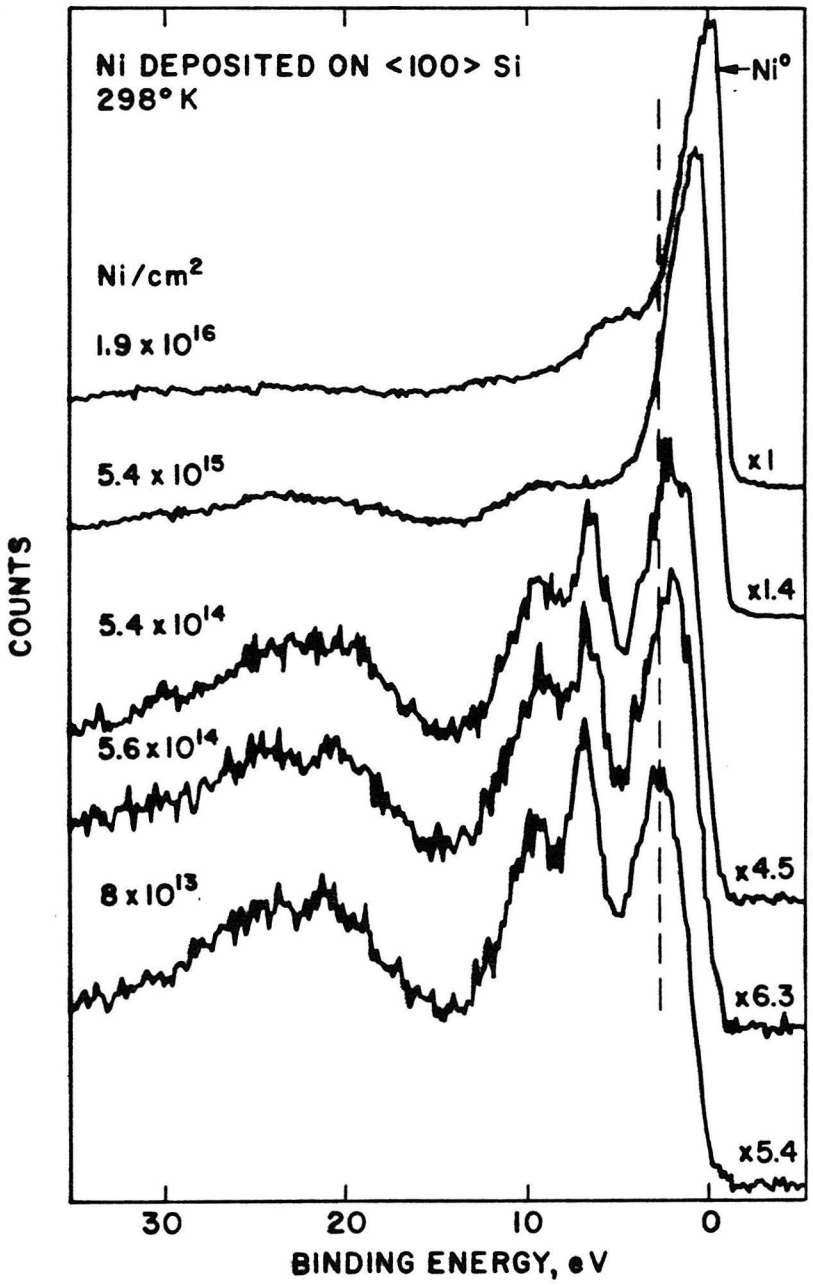

Figure 2: Plot of the XPS derived valence bands as a function of the Ni coverage on <100> Si.

$\sim$10 eV.

Detailed interpretation of these spectra will require the interplay of theory and experiment. Theoretical calculation on the bulk silicides, for which the structures are known, should be attempted to interpret the XPS derived valence band spectra. From such a study, one may well be able to derive the electronic nature of the chemical bonding in the interfacial regions. In particular, one could examine the relative contribution of the outer silicon d orbitals to bonding in the bulk and interfacial silicides proposed in Chapter III of this thesis.

References

1) P. S. Ho, T. Y. Tan, J. E. Lewis, G. W. Rubloff, J. Vac. Sci. Technol., 16, 1120, (1979)

2) J. L. Freeouf, G. W. Rubloff, P. S. Ho, T. S. Kuan, Phy. Rev. Lett., 43, 1836 (1979)

3) J. A. Roth, Thesis, University of Southern California, Materials Science Department

4) S. Hüfner in Topics in Applied Physics, L. Ley, M. Cardona, Eds., (Springer-Verlag, 1977)

5) D. R. Jennison, Phys. Rev. Lett., 40, 807 (1978)

6. B. Feuerbacher, B. Fitton in Topics in Current Physics, H. Ibach, Ed., (Springer-Verlag, 1977)

7. J. L'Ecuyer, J. A. Davies and N. Matsunami, Nucl. Instr. Meth., 160, 337 (1979)

SYNTHESIS OF UNUSUAL COPPER COORDINATION ENVIRONMENTS USING ION IMPLANTATION

ABSTRACT

The use of ion implantation is proposed as a method to synthesize unusual coordination environments for copper. The reaction products may be characterized using Mössbauer spectroscopy. $^{4}He^{+}$ backscattering and channeling studies may also be performed to yield additional information concerning the Cu atom site.

INTRODUCTION

The use of ion implantation to modify the surface properties of solids is a well established technique in solid state physics. Much of the early research concentrated on the use of ion beams to modify semiconductors for device applications, but in recent years there has been an increasing interest in the application of ion beams to problems in material science and chemistry. Ion implantation has now been sucessfully employed in such diverse fields as catalysis[1], superconductivity[2], corrosion[3], luminescence[4], optical wave-guides[6], and color center formation.[7]

One aspect of ion implantation that has only begun to emerge is its potential for solid state chemical synthesis. The study of the reaction products formed between implanted ions and the target constituents or other implanted ions is a potentially rewarding field. Since the interaction of a solid with energetic ions involves single

atoms reacting far from equilibrium conditions, unconventional chemical reactions may occur resulting in unusual chemical compounds and coordination environments. Moreover, ion implantation allows a flexibility that does not exists in conventional chemical synthesis. Ions may be introduced into the solid with a variety of kinetic energies and at any substrate temperature without regard to the normal limitations of chemical solubility, stoichiometry, and grain boundary diffusion.

Only a few examples of the use of ion implantation in solid state chemistry exist in the literature. The most interesting is the work by Wolf, et al, where the synthesis of heteronuclear carbonyl compounds was demonstrated.[7] By implanting radioactive $^{56}Mn^{+}$ ions at 100 Kev kinetic energy into the organometallic compound $Re_2(CO)_{10}$, they were able to synthesize the mixed carbonyl $MnRe(CO)_{10}$. In addition to this compound, which may be synthesized in small amounts by other methods, they produced a range of entirely new heteronuclear metal carbonyls with Cr, Re, Ru, Ir, and Fe. By implanting with $^{64}Cu^{+}$, they synthesized a variety of Cu carbonyls. These compounds are extremely interesting since stable Cu carbonyls have not been prepared by any other method.

PROPOSAL

It is proposed here that the novel non-equilibrium conditions possible with ion implantation by used to produce unusual copper coordination sites. This may be accomplished by implanting Cu^{+} into a variety of inorganic complexes. An investigation of unusual copper coordination may potentially yield information regarding the coordination

of copper in the metallo-proteins involved in electron transport in plants.

It is suggested that the initial study involve implantation of 10-100 Kev $^{61}Cu^{+}$ ions into the two basic ligand systems ethene-1,2-dithiolate ($S_2C_2H_2^{2-}$) and dithiocarbamate ($S_2CNH_2^{-}$). The ammonium-, tetramethyl ammonium-, and tetrabutyl ammonium-dithiocarbamates, in particular, crystallize nicely and will provide a systematic variation of the crystal lattice parameters. Implantation into the ligand crystals with alkali metal counterions or inert gases such as xenon or argon should also be performed as a check for possible substrate decomposition.

The major experimental problem that will be encountered with ion implantation is the radiation damage that accompanies heavy ion implants. This damage will show itself primarily as an increase in the substrate lattice disorder, but ion induced mixing of the substrate composition is also possible. Wolf, et. al, found that when 60 Kev $^{51}Cr^{+}$ was implanted into $Mo(CO)_6$, 50% of the Cr^{+} could be converted to $Cr(CO)_6$ at ion dosages of 10^{12} ions/cm^2 or less. For dosages greater than 10^{12} ions/cm^2, the $Mo(CO)_6$ substrate began to suffer radiation damage. At 10^{14} ions/cm^2, the $Mo(CO)_6$ became highly disorder and the yield of $Cr(CO)_6$ dropped essentially to zero.

Considering the radiation damage problem discussed above, a total ion dosage of 10^{12}-10^{13} ions/cm^2 is probably the maximum feasible dosage. The exact possible dosage will depend on many factors- the target substrate structure, sputtering coefficients, temperature, etc. Lattice

damage may be reduced by implanting in a substrate at LN_2 temperatures. This should also help to "freeze in" unusual coordination sites. Implanting ions along an oriented crystallographic plane should also help to decrease lattice disruption since the number of nuclear collisions is reduced.

Since a maximum of 10^{13} molecules will be synthesized by implanting $^{61}Cu^+$ into various single crystal complexes, an additional problem is the characterization of the resulting reaction products. The depth of $^{61}Cu^+$ implantation at kinetic energies of 10-100 KeV will be less than 1000 Å. Conventional transmission spectroscopies probably will not be able to detect the reaction products. Similarly, techniques such as Auger and x-ray photoelectron spectroscopy will be of limited used since they sample only the first 10-150 Å of a sample surface. It is suggested here that the ion implantation reaction products be examined using Mössbauer spectroscopy. The ^{61}Cu isotope has a half-life of 33 hours and undergoes β-decay to form the ^{61}Ni Mössbauer nucleii. The ^{61}Ni nucleii undergo γ-emission with a photon energy of 67.4 Kev, and have a half-life of 5.3 nanoseconds. Although this lifetime is rather short, the resulting Mössbauer linewidths should still be adequate for the resolution of hyperfine structure. The technique of $^4He^+$ Rutherford backscattering (RBS) is also suggested since it will allow one to determine the depth profile of the implanted Cu atoms. Moreover, the phenomenon of ion channeling by the substrate crystal lattice may be examined with RBS to determine the extent of lattice disorder created by the implantation procedure. Channeling

may also be used to deduce whether the Cu atoms are in substitutional or interstitial sites in the host crystal.

References

1) M. Voinov, D. Buhler, H. Tannenberger, Proc. Electrochem. Soc., San Francisco, 1974

2) B. Stritzker, 1975 Intl. Conf. on Applications of Ion Beams to Materials, p 160

3) V. Ashworth, D. Baxter, W. A. Grant, R. P. M. Proctor, 1975a Proc. Intl. Conf. on Ion Implantation in Semiconductors and Other Materials, Osaka, 1974, S. Namba, Ed., (Plenum Press, New York)

4) M. C. Wintersgill, P. D. Townsend, F. Cussoperez, J. de Phys., C7, 123 (1977)

5) M. Saidoh, P. D. Townsend, J. Phys. C., 10 1541 (1977)

6) T. Ukai, N. Matsunami, K. Morita, N. Itoh, Phys. Lett., 56A, 127 (1976)

7) G. K. Wolf, W. Froschen, U. Sahm, 1975 Proc. Intl. Conf. on Ion Implantation in Semiconductors and Other Materials, Osaka, 1974 S. Namba, Ed., (Plenum Press, New York)

SILICON/METAL SILICIDE INTERFACIAL STUDIES USING THIN MONOCRYSTALLINE SILICON

ABSTRACT

It is proposed that thin 1000 - 2000 Å single crystal silicon be used to investigate the chemical nature and width of the technologically relevant silicon/silicide interface. X-ray photoelectron spectroscopy is used to dynamically monitor the interfacial growth front during *in situ* silicide formation.

INTRODUCTION

As part of the work reported in this thesis, the chemistry of transition metal silicide/silicon interfaces was examined by dynamically monitoring the advancing planar silicide growth front during *in situ* formation of the silicide. The photoemission signals of the emerging metal atoms were monitored as a function of time to interrogate the interfacial chemistry. These experiments required that the reaction front be monitored through a thin silicon overlayer. Thin 1500 Å layers of amorphous Si on Ni, Pt, or Pd were used. However, the more technologically relevant interface is that found between crystalline silicon and the metal silicides. Device grade single crystal silicon wafers are 10-20 mils thick and their use in these photoemission experiments is not feasible.

PROPOSAL

A procedure has recently appeared for preparing large area self-supporting silicon thin crystals 1000 Å to 2 μm in thickness.[1] Crystals up to 2 cm in diameter with <100>, <110>, or <111> orientations can be produced. Thickness variations across the crystal are as low as ±60 Å. It is proposed here that these thin crystals be used to investigate the crystalline silicon/silicide interface. The experimental procedure for preparing these thin crystals and the subsequent interfacial experiments are discussed below.

1) Preparation of the thin crystalline Si windows

The preparation of thin Si crystals is based on a selective ethylenediamine-pyrocatechol etch (EDP), which does not attack Si when it is sufficiently doped with boron. The procedure is outlined in Figure 1. A thin p^+ surface layer is formed in a device grade single crystal Si wafer by boron doping. This doping is most conveniently achieved by thermal diffusion at 1050° C using boron nitride as the diffusion source. The penetration depth of the boron, which determines the final thin-crystal thickness, is controlled by the diffusion time. Approximately 15 minutes diffusion time will result in a 2000-2500 Å thickness, depending on the flow rate of the carrier gas and the furnace geometry. The boron glass that is deposited on the surface of the wafer may be removed by immersing the wafer in boiling nitric acid and then rinsing with hydrofluoric acid.

Because EDP etches Si at a rate of only 3-50 μm/hour, depending on the crystal orientation, it is necessary to remove a major

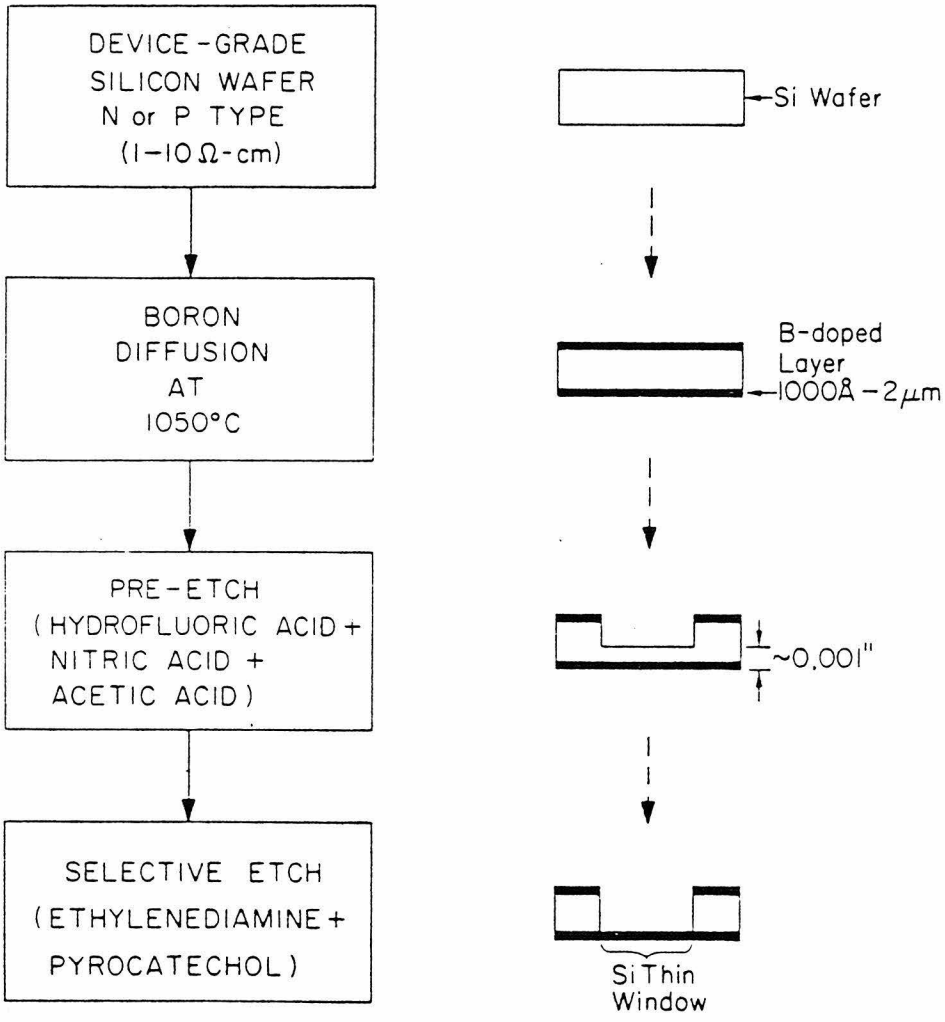

Figure 1: Processing schematic for the preparation of thin crystalline silicon windows. (From Reference 1).

portion of the Si with a faster non-selective pre-etch. An etch rate of approximately 25 μm/minute can be obtained using a 2:5:2 solution of HF, HNO_3, and glacial acetic acid. A small piece of the boron doped Si wafer should be mounted polished side face-down on a quartz disc using paraffin to protect the edges of the wafer. Adhesive teflon tape with a circular hole in the middle is then placed on top of the mounted Si wafer. All areas of the wafer except for the circular hole are thus protected from the etch. The mounted sample can now be immersed in the pre-etch solution. Agitation of the etching solution should be provided by rotating the solution beaker and by bubbling N_2 or O_2 gas through the solution. This insures a uniform etch rate by preventing the nucleation of gas bubbles on the Si surface. The Si wafer should be etched to approximately 1 mil thickness. At this thickness, the thinned region is transparent to light. The sample can be removed from the mounting disc at this time and the teflon tape removed.

The final thinning process illustrated in Figure 1 uses a selective etch at 110° C: pyrocatechol ($C_6H_4(OH)_2$), ethylenediamine ($NH_2(CH_2)NH_2$), and water in the ratio 3 gm : 17 ml : 8 ml. This solution will not etch silicon if the boron level exceeds 7×10^{19} /cm^3. The time required for this etching step ranges from 1-4 hours. After completion, the sample should be rinsed in hot ethanol.

The distribution of defects in these thin crystals has been investigated using the channeling properties of ion beams.[1] Figure 2 shows the channeled and random spectra of a 4300 Å Si <110> crystal. The χ_{min} value, which is the ratio of the scattering yields between the

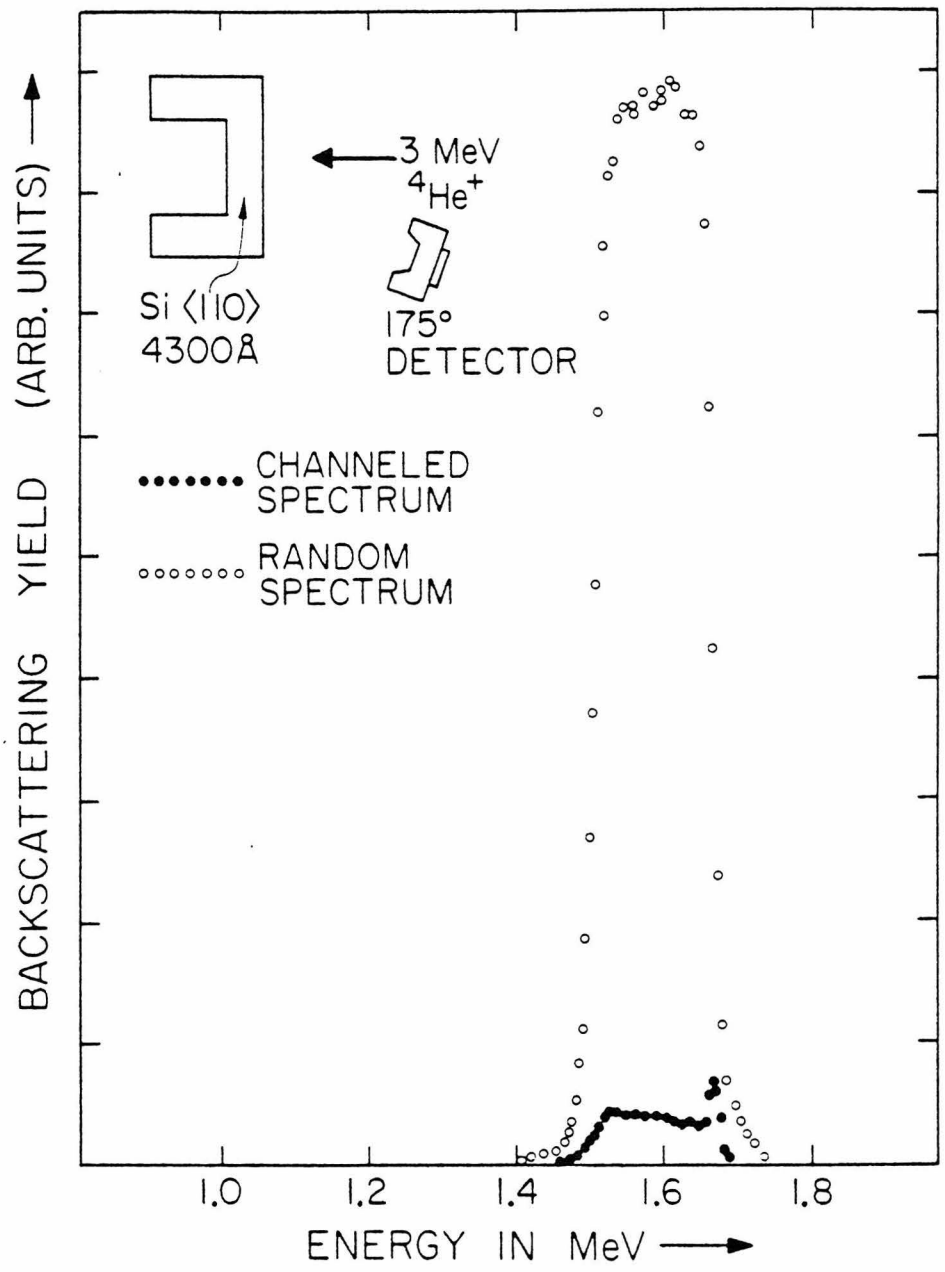

Figure 2: Channeled and random spectra of a 4300 Å thick Si (110) crystal. The channeling axis is (110). (From Reference 1).

channeling and random incident directions, ranges from 3-5%. This is comparable to the χ_{min} found for the starting Si wafer.

2) The silicon/silicide interface experiment

It has been reported that SiO_2 and metal silicide layers can be grown on these thin crystals by thermal annealing up to 850° C.[2,3] The interface experiments discussed in detail in Chapter III of this thesis may be extended to the crystalline Si/silicide interface using the sample arrangement illustrated in Figure 3. At least a micron of the transition metal of interest should be deposited on the polished side of the thin Si crystal. This should help to add strength to the thinned region.

By heating this sample *in situ* to 250° C in the analyzer chamber of the XPS spectrometer, the advancing planar crystalline Si/silicide growth front may be studied. Because photoemission intensities are exponentionally attenuated by solids, the first metal core level signal should be detected when a Si overlayer of 50 - 75 Å still exists. By monitoring the metal core lines as a function of time the metal environment in the Si/silicide interfacial region can be compared to that found for the metal in the bulk silicide. In addition to the chemical enivironment at the interface, the width of the transitional layer may be determined as well using the equations derived in Chapter III of this thesis.

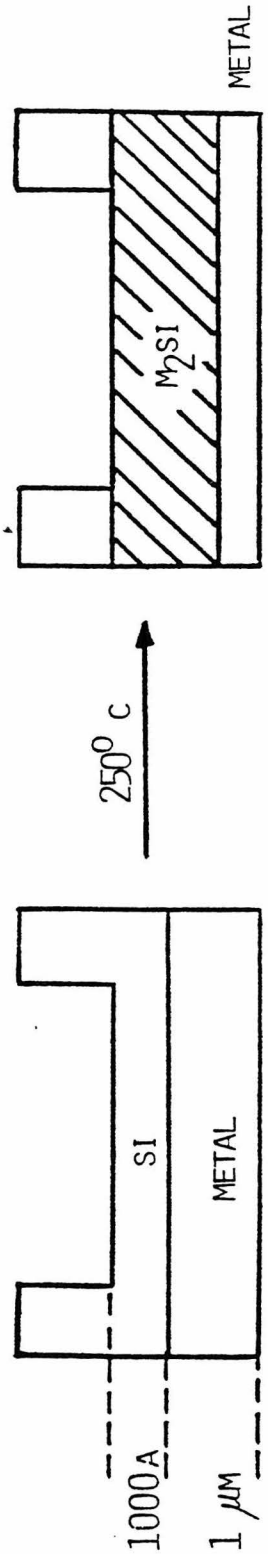

Figure 3: Schematic of the sample arrangement for the XPS interface experiments.

References

1) N. W. Cheung, to be published

2) N. W. Cheung, L. C. Feldman, P. J. Silverman, I. Stensgaard, Appl. Phys. Lett., 35, 859 (1979)

3) N. W. Cheung, M-A. Nicolet, J. W. Mayer, to be published in the Proceedings of the Symposium on Thin Film Phenomena- Interfaces and Interactions, The Electrochemical Society Meeting, Los Angeles, California, (October 14-19, 1979)